

Kinetic Investigations of Thiolate Protected Gold Nanoparticles: Protein Interactions,
Electron Transfer, and Precursor Formation

By

Brian N. Turner

Dissertation

Submitted to the Faculty of the
Graduate School of Vanderbilt University
in partial fulfillment of the requirements
for the degree of

Doctor of Philosophy

in

Chemistry

December, 2011

Nashville, Tennessee

Approved:

Professor David E. Cliffel

Professor John A. McLean

Professor James E. Crowe, Jr.

Professor David W. Wright

In Memory of Sharon Rose Turner and Ruth Shelton Turner

A special thanks to Mom, Dad, April, Eric, Gramps, Keith, and Patti

Lovingly dedicated to Mary Pat

ACKNOWLEDGEMENTS

Acknowledgements of people who helped along the way are included at the end of each chapter, but I would like to reserve this section to thank people who helped in unique ways.

As for my committee, I will open with Dr. David Cliffler. I have always appreciated your knowledge and creativity in generating new ideas. I have also appreciated the freedom I have had to go in my own direction with research that seems very unique to this lab. Also, I really appreciate your humanistic approach to leaves of absence, and never once interfering in personal business. This was especially appreciated as many personal crises and family crises seemed to continually arise over the last six years, and I am not sure I would have been able to deal with them appropriately in a lot of other situations. On a lighter note, it was a pleasant surprise to work for someone who would have the group over to play strategy games, volleyball, and generously provided wonderful food to a somewhat larger research group. Finally, thanks for having the patience to allow me to work here over a six year period, all the while providing financial support.

Dr. Wright, I have always secretly appreciated your no-holds-barred attitude, and tell-it-like-it-is approach to committee meetings. I think this is a very important trait when it comes to making sure that the science we practice is legitimate. My favorite part about your approach is your intensity about the science because I believe that it should be exciting and meaningful to the researchers instead of just a means to a job. Until I saw

you lecture at a SERMACS, I had never appreciated how exciting bio-inspired materials design really is in terms of practical potential and elegance.

Dr. McLean, I would like to thank you for some of the most interesting science conversations I have had during my stay here. My personal favorite was the discussion about how to weigh an electron accurately. I always looked forward to your classes, because you have a unique gift of making complicated topics seem approachable and exciting. I also enjoyed hanging out with you socially in Atlanta during Pittcon. We will have to meet at another conference and play that shuffleboard game again.

Finally, Dr. Jim Crowe, until I met you, I had not met somebody who works on such a high level in their field that is as approachable as you are. Additionally, I appreciate that you are always very thoughtful with your questions.

It would take me way too long to thank everybody individually in my research group for sitting through my practice exams and the like. Thank you to everyone, as it was much appreciated.

Graduate school can be a difficult time, so I would like to thank Bill Evans, Vanessa Phelan, Dr. Victor Ghidu, Easton Selby, Danielle “Watkins” Kimmel, the volleyball crew, the soccer crew, the old Magic the Gathering crew (ignore that), and the current strategy gaming crew for keeping things light when times were not. I would also like to thank all of my old friends back home and elsewhere for staying in touch, offering encouragement, and giving me an excuse to leave town every here and again, especially Mike Pateras, Lora Robinson, Greg Raffio, Alicia DiMarco, Mykola Bilokonsky, and Ryan Stolte-Sawa.

Finally, it would be hard to put into words the contributions of family, so I will just suffice it to say that when things got tough here, I would not have continued along if not for your encouragement and belief. I love you all.

And Mary Pat, I just want you to know that I would not have finished this if you hadn't pushed me. And Dad, I never would have gotten into this in the first place without your constant support and help.

I would like to acknowledge the following sources of funding: the National Institutes of Health Sections on General Medicine [NIH/NIGMS (R01 GM 076479)] and Allergies and Infections Disease- Southeastern Regional Center for Excellence in Biodefense [NIH/NIAID/SERCEB (U54 AI057157)], the Defense Threat Reduction Agency, the Research Corporation, the Vanderbilt University Graduate School and their Travel Grant Program (which provided for trips to Pittcon 2007 and ACS National Meeting Fall 2010), Oak Ridge National Laboratory Center for Nanophase Materials Science and the Vanderbilt University Department of Chemistry Teaching Assistant Program.

TABLE OF CONTENTS

	Page
DEDICATION	ii
ACKNOWLEDGEMENTS	iii
LIST OF TABLES	x
LIST OF FIGURES	xi
I. INTRODUCTION: SYNTHESIS AND CHARACTERIZATION OF VARIOUS THIOLATE PROTECTED GOLD NANOPARTICLES AS PREPARED BY MODIFIED BRUST METHODS.....	1
Introduction.....	1
Background.....	1
Synthetic Routes	3
Functionalization of Thiolate Protected Gold Nanoparticles	5
Characterization Methods for MPCs	11
Methods	14
Instrumentation for Routine Nanoparticle Characterization	14
II. LINEAR EPITOPE MAPPING APPROACH TO LOCATE BINDING “HOT SPOTS” IN THE CONFORMATIONAL ANTIGENIC SITE A OF HUMAN RESPIRATORY SYNCYTIAL VIRUS (HRSV) FUSION PROTEIN (F)	15
Introduction.....	15
Background.....	16
Human Respiratory Syncytial Virus	16
Epitope Mapping	22
Quartz Crystal Microbalance (QCM)	24
Methods	31
Instrumentation.....	31
Materials.....	31
Peptide Synthesis.....	32
Formation of peptide SAMs	33
ELISA Stepwise linear epitope mapping of the full length RSV F Antigenic Site A	36

	Results and Discussion	38
	Peptide QCM step-wise linear epitope mapping	38
	Peptide ELISA step-wise linear epitope mapping	43
	Acknowledgements	51
III.	GOLD NANOPARTICLES PRESENTING PEPTIDES AS BIOMIMICS OF HRSV F PROTEIN ANTIGENIC FUNCTION.....	53
	Introduction.....	53
	Background.....	54
	Nanoparticles Presenting Peptides as Antigenic Mimics.....	54
	Quartz Crystal Microbalance Immunosensing	61
	Methods	62
	Materials.....	62
	Peptide Synthesis	63
	Synthesis of Au ₂₁₆ Tiopronin ₁₂₉ Nanoparticles	64
	Synthesis of Au ₁₁₈ Tiopronin ₇₁ Nanoparticles	65
	Synthesis of Au ₆₉₆ Tiopronin ₂₆₅ Nanoparticles	66
	Place Exchange to Form Series 3 Peptide-Nanoparticle Conjugates	67
	QCM Immunosensor Construction and Detection of HRSV	67
	Adaptation of the QCM Immunosensor to Detect Peptide Presenting Gold Nanoparticles	68
	Results and Discussion.....	69
	QCM Immunosensor for HRSV	69
	Development of Peptide Presenting Gold Nanoparticles.....	73
	Detection of Peptide Presenting Gold Nanoparticles with the QCM Immunosensor for HRSV	74
	Acknowledgements	86
IV.	SECM OF “WIRED” GOLD NANOPARTICLES TO DETERMINE ELECTRON TRANSFER KINETICS: PROOF OF CONCEPT FOR POTENTIAL COMPONENTS IN NANOMOLECULAR CIRCUITS.....	87
	Introduction.....	87
	Background.....	88
	Molecular Electronics	88
	Electrochemical Properties of Gold Nanoparticles	92
	Molecular Wire Molecules.....	95
	Scanning Electrochemical Microscope.....	99
	Methods	107
	Materials.....	107
	Synthesis of Au ₁₁₂₀ Dodecanthiolate ₆₉₀	108
	Synthesis of Au ₂₂₈ Octanethiol ₉₂	109

Deprotection of S-[4-(2-Phenylethynyl)phenyl]ethynylphenyl]thioacetate (PEPEPSAc)	110
Place exchange reactions with PEPEPSAc and PEPEPS ₂	111
Scanning Electrochemical Microscopy Experiments	111
Nanoparticle Surface Quantitation	113
Results and Discussion	114
A Note About Surface Ligand Quantitation.....	114
SECM Qualitative Observation of AuDodecanethiol Electron Transfer Rates.....	116
Improved Synthesis of Alkanethiol Nanoparticles Reduces Current Drift	119
SECM Quantitative Observation of AuOctanethiol Electron Transfer Rates.....	121
Acknowledgements	125
V. KINETIC INVESTIGATION OF TIOPRONIN PROTECTED GOLD NANOPARTICLE PRECURSOR FORMATION.....	126
Introduction.....	126
Background.....	126
Methods	131
Materials.....	131
UV-Visible Spectroscopy Kinetics Experiments	131
Results and Discussion	132
Preliminary Observations.....	132
UV-Visible Spectroscopy	133
Acknowledgements	154
VI. SUMMARY OF CONCLUSIONS AND SUGGESTIONS FOR FUTURE WORK.....	155
Summary of Conclusions.....	155
Suggestions for Future Work.....	157
Biomimetic Nanoparticles.....	157
Wired Nanoparticles	160
Nanoparticle Precursor Formation.....	161
Appendix	
A. THERMAL GRAVIMETRY-MASS SPECTROMETRY AND ELEMENTAL ANALYSIS OF TIOPRONIN PROTECTED GOLD NANOPARTICLES	148
B. SYNTHESIS AND CHARACTERIZATION OF WATER SOLUBLE DENDRIMER PROTECTED GOLD NANOPARTICLES	158

C.	SYNTHETIC ROUTES TO P-MERCAPTOPHENYETHYNYLBENZENE	162
D.	PURIFICATION AND CHARACTERIZATION DATA FOR PEPTIDES USED IN THIS STUDY OR OTHERWISE DESIGNED AND PURIFIED	158
E.	ADDENDUM TO “COLOR MY NANOWORLD” EXERCISE USED AT THE VANDERBILT SUMMER ACADEMY	178
	REFERENCES	181
	CURRICULUM VITAE	1

LIST OF TABLES

Table	Page
1. Summary of reported HRSV escape mutations in HRSV F antigenic site A.	21
2. Tabulated characterization data for peptides purified by this author.	33
3. Peptides designed to be evaluated by the QCM step-wise linear epitope mapping method.....	35
4. Peptides evaluated against palivizumab in an ELISA assay.	36
5. Student's t-tests for peptide ELISA.....	45
6. Peptides that were conjugated to nanoparticles in this study.	64
7. Nanoparticle mimics studied with the QCM HRSV immunosensor.	74
8. Summary of mimic A detection at various concentrations, along with sensor characterization data	78
9. electron transfer kinetic constants determined for Au ₂₂₈ Octanethiol _{92-n} PEPEPS _n	123
10. Rate data for the reaction of Au(III)Cl ₄ ⁻ with tiopronin in MeOH at unfixed ionic strength.....	142
11. Rate data at fixed [RSH] and [Au(III)] with variable [H ⁺] (adjusted with perchloric acid/MeOH solution) and [Cl ⁻] (adjusted with sodium chloride/MeOH solution). ..	145
12. Rate data for conditions designed to test saturation kinetics of the tiopronin/tetrachloroaurate system.	148
13. Elemental analysis-calculation compared to two different TGA-TEM calculations of molecular formula.....	167
14. Characterization data for peptides synthesized by this author.	187

LIST OF FIGURES

Figure		Page
15.	Modified Brust reaction scheme for polar ligands.	3
16.	Examples of thiolate ligands used in the synthesis of water soluble Au MPCs.....	4
17.	Scheme of the solution phase place-exchange reaction.	5
18.	The stoichiometry of incoming to exiting ligand is 1:1.	5
19.	Chart of the different relative rates at which place-exchange and (possibly) migration occur.....	6
20.	The non-covalent interaction based place-exchange reaction. ⁴⁹	9
21.	Cartoon schematic of an HRSV virion.	18
22.	HRSV F protein, showing the head, neck, and stalk structure.....	20
23.	ELISA study of synthetic peptides from Rutledge and coworkers	24
24.	QCM graph illustrating the binding of BSA to bare gold and PZ to a mixed SAM of peptide 2 and tiopronin.	40
25.	QCM graph illustrating the binding of BSA to bare gold and PZ to a mixed SAM of peptide 8 and tiopronin.	40
26.	QCM graph illustrating the binding of BSA to bare gold and PZ to a mixed SAM of peptide 10 and tiopronin.	41
27.	Results of the optimized peptide ELISA.....	44
28.	A conceptual interpretation of PZ approaching the synthetic peptide epitope	47
29.	Motavizumab peptide epitope of HRSV F (gray) interacting with the light chain (blue) and heavy chain (green).	50
30.	Comparison of the glutathione (top) and tiopronin (bottom) ligands	56
31.	10-amino acid HA peptide on a 3-D gold tiopronin nanoparticle	57
32.	Loop presenting MPCs (left) shown compared to the native protein	58

33.	Cartoon schematic of the QCM based immunosensor for HRSV detection.	69
34.	Detection of HRSV with the QCM-PZ immunosensor.	70
35.	Detection and control experiments for the QCM-PZ immunosensor.	71
36.	¹ H NMR, with double water-gate solvent suppression, of a peptide-nanoparticle conjugate	73
37.	Detection of Au ₆₉₆ Tiopronin ₂₅₅ Peptide(3-F) ₁₀ by the QCM immunosensor with and without PZ.	76
38.	Representative QCM mass versus time curves at various concentrations of mimic A during the detection step.	79
39.	Plot to determine the time constant for mimic A binding to the Palivizumab sensor .	80
40.	Plot of individual time constants determined for each concentration.....	81
41.	Plot to determine binding coefficients using the four lowest concentration samples..	83
42.	Nanoparticle-bipyridine redox switch.....	89
43.	Cowpea mosaic virus-gold nanoparticle-molecular wire conjugate molecular electronic nanosensor.....	91
44.	Square wave voltammogram of AuHexanethiolate nanoparticles.	93
45.	The molecular wire ligand	95
46.	Current-voltage profiles of molecular wires sandwiched between gold wires.	97
47.	Read-write computing system with gold electrodes sandwiching molecular wires. ...	98
48.	SECM as a useful imaging technique in biological and materials applications.....	101
49.	SECM experimental design.....	102
50.	SECM approach curves of AuAlkanethiolate nanoparticles.....	103
51.	Proof of concept experiments to confirm whether “wired” AuDodecanethiol nanoparticles (left) exhibit faster electron transfer than their “unwired” precursors (right)	107
52.	MALDI-IM mass spectrum of AuDodecanethiolate nanoparticles functionalized with the molecular wire.	115

53.	SECM approach curve with 1V Pt UME through larger AuDodecanethiolate nanoparticles.....	117
54.	SECM approach curve with 1V Pt UME through larger “wired” AuDodecanethiolate nanoparticles.....	118
55.	Comparison of ¹ H NMR spectra of dodecanethiol gold nanoparticles synthesized by the Brust method (blue), and by the method of Rowe and coworkers (red)	120
56.	SECM approach curve through Au ₂₂₈ Octanethiol ₉₀ PEPEPS ₂ , Au ₂₂₈ Octanethiol ₉₀ PEPEPS _{2.6} , and Au ₂₂₈ Octanethiol ₉₂	122
57.	Nanoparticle and ring complex structures.....	128
58.	Time resolved UV-Vis spectra of AuCl ₄ ⁻ undergoing reduction by tiopronin.....	134
59.	UV-Vis region containing the saddle at 289 nm for the gold(III)/tiopronin system.	135
60.	Time resolved UV-Vis spectra of tetrabromoauric acid undergoing reduction by tiopronin.	137
61.	Dynamic reaction profiles of Au(III)Cl ₄ ⁻ with tiopronin	138
62.	Plots to determine the order of reaction with respect to Au(III)Cl ₄ ⁻	140
63.	Plot to determine the reaction order and pseudo first order rate constant with respect to [Au(III)].....	141
64.	Plot to determine the order of reaction with respect to [RSH], <i>n</i> , and the overall rate constant, <i>k_{net}</i>	142
65.	Saturation behavior was suspected when <i>k_{Au(III),1}</i> lost a linear relationship with [RSH] at higher [RSH].....	148
66.	Determination of parameters <i>a</i> and <i>b</i> for the saturation kinetics rate law.	149
67.	Thermogravimetric profiles of gold hexanethiol cluster (red) and gold tiopronin cluster (black).	166
68.	Thermal gravimetric spectrum generated on the TG-MS instrument at Oakridge....	169
69.	Selective ion scan of elemental and small molecule fragments thermally lost from AuHexanethiol nanoparticles.	170
70.	Larger mass peaks thermally lost from AuHexanethiol nanoparticles.	171
71.	Small mass fragments thermally lost from AuTiopronin nanoparticles.	172

72.	^1H NMR of G1 dendrimer protecting a gold nanoparticle	175
73.	TEM micrograph and size distribution of AuG1S NCDs.	176
74.	^1H NMR data G1 place exchanged onto AuTiopronin.	177

CHAPTER I

INTRODUCTION: SYNTHESIS AND CHARACTERIZATION OF VARIOUS THIOLATE PROTECTED GOLD NANOPARTICLES AS PREPARED BY MODIFIED BRUST METHODS

Introduction

The practical focus of this dissertation is the adaptation of stable, chemically versatile, easy to synthesize thiolate protected gold nanoparticles to medicine (Chapters II and III) and molecular electronics (Chapter IV). In the course of the studies aimed at these goals, a number of questions arose about fundamental aspects of nanoparticle synthesis, their mechanism of formation, and characterization techniques used to describe them. These secondary interests came to define much of the content of this dissertation (especially Chapters I and V, and Appendices A and B).

Background

(Note: much of this background material appears in a previously written review article by this author, Brian Huffman, and David Cliffel. It has been rewritten and truncated for clarity).¹

The scientific study of colloidal metal particles dates back to Faraday in the mid-19th century.² The synthesis and characterization, notably by electron microscope, of water “soluble” gold colloids as small as 18 nm was completed by Turkevich and co-workers in

1951.³ Monolayer protected clusters (MPCs), a term used by Royce Murray to describe small gold nanoparticles that are identical or similar to those first synthesized by Brust and coworkers,⁴ differ from metal colloids in that they can be repeatedly dried, isolated from, and redissolved in common solvents without decomposing or aggregating.⁵ For the duration of the dissertation, the term nanoparticle will be used instead of cluster, so as not to confuse these nanomaterials with smaller cluster structures of discrete morphology. These small gold nanoparticles are obtained using a bottom-up approach (as opposed to a top-down approach such as lithography), implying that the creation of a great variety of nanomaterials is possible from a small number of building block materials.⁶

Nanoparticles are created with a variety of core types and, furthermore, capping ligands, to create water or organic soluble products with desired functions. Both metallic and non-metallic starting materials are used in the creation of nanoparticle structures, such as: thiolate protected gold,^{4, 5, 7-11} organic polymers,¹²⁻¹⁵ virus-like particles,¹⁶⁻²¹ protein particles,²² colloidal particles,^{3, 23, 24} and semiconductor quantum dots.²⁵ Thiolate protected gold nanoparticles have been the focus of studies in our research group because of their ease of creation, water and air stability, electrochemical and optical properties, biocompatibility, and their ability to be surface functionalized by straightforward techniques with a variety of sulfur containing ligands. Thiolate protected gold nanoparticles of the type focused on in this dissertation can range in size from 1-10 nm, containing approximately 55-1000 gold atoms which correlates with molecular weights between 20 – 200 kDa.²⁶

Synthetic Routes

The Brust reaction is a standard method to produce small gold nanoparticles that can be tuned to a number of organic solvents. Nanoparticles prepared by this method are most commonly synthesized with alkanethiolate protecting molecules, which lead to relatively stable nanoparticles. More recently, water solubility of gold nanoparticles was easily accomplished by using water-solubilizing protecting thiolate ligands in a modified Brust reaction as depicted in Scheme 1.^{4,8} In the single phase Brust reaction, tetrachloroauric acid is reduced from Au(III) to Au(I) in the presence of the thiol capping ligand in a polar solvent, yielding an orange, brown, or ruby red solution that fades to clear over time. The color change has been attributed to a Au(III)-thiol complex which is reduced to a Au(I) complex over time which ultimately forms either a gold-thiol polymer,⁵ oligomer, or cyclic tetramer.²⁷ Precursor formation in the context of water soluble tiopronin protected gold nanoparticles is the subject of Chapter V. Following the initial reduction, the Au(I) is further reduced to Au⁰ in the presence of sodium borohydride (NaBH₄), yielding a black to dark brown or purple solution. Other reducing agents have been used for other metal cores, such as lithium aluminum hydride (LiAlH₄) or lithium triethylborohydride.^{10, 11}

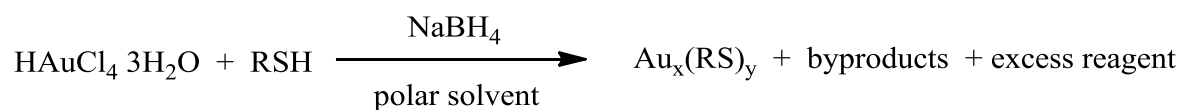


Figure 1: Modified Brust reaction scheme for polar ligands.

Key examples of thiolate ligands that have been used to produce water soluble, long-term air and solvent stable clusters are tiopronin,⁸ glutathione,²⁸ 4-mercaptobenzoic acid,²⁹ 1-thio- β -D-glucose,³⁰ and N,N,N-trimethyl(mercaptoundecyl)ammonium (TMA),³¹ as shown in Figure 2.

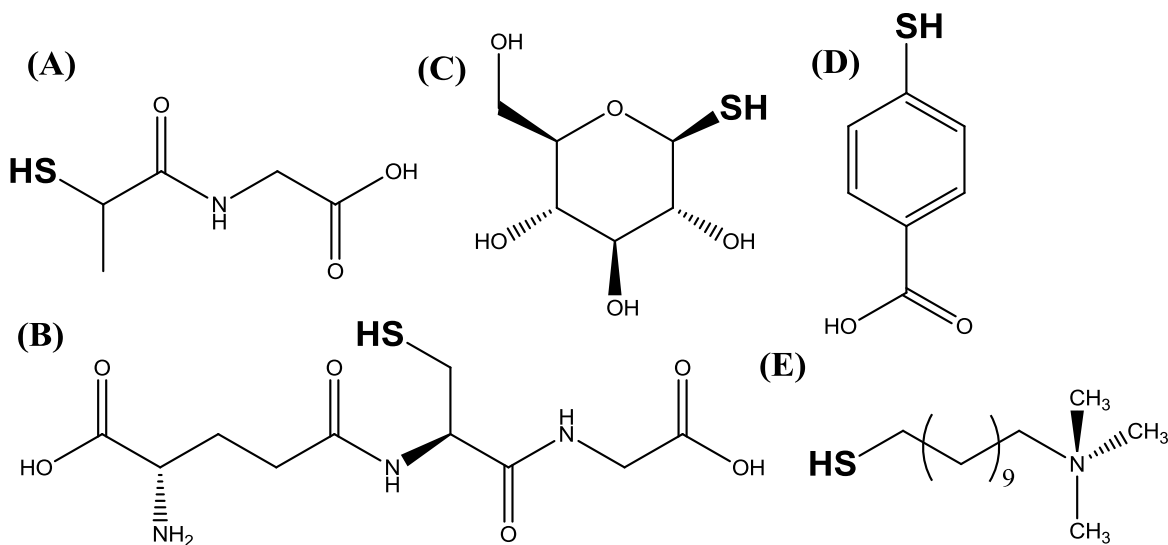


Figure 2: Examples of thiolate ligands used in the synthesis of water soluble Au MPCs. (A) tiopronin, (B) glutathione, (C) 4-mercaptobenzoic acid, (D) 1-thio- β -D-glucose, (E) N,N,N-trimethyl(mercaptoundecyl)ammonium.

In Chapter III, tiopronin (3-mercaptopropionyl glycine, Figure 2(A)) protected gold nanoparticles will be used as a scaffold to present synthetic peptide epitopes to a commercial antibody immobilized on a novel immunosensor platform. Tiopronin has been popular in our lab as it produces high yield, long-lasting nanoparticles in a straightforward synthesis with robust results.

Functionalization of Thiolate Protected Gold Nanoparticles

Transformation of these gold nanoparticles into materials with relevance to biology and engineering has been accomplished by a variety of synthetic functionalization strategies, out of which, the most widely used and thoroughly studied method is the thiol place-exchange reaction depicted in Figure 3.

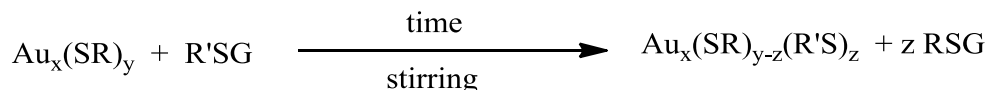


Figure 3: Scheme of the solution phase place-exchange reaction. The stoichiometry of incoming to exiting ligand is 1:1.

Place-exchange involves an incoming ligand, such as a thiol containing biomolecule, taking the place of one of the original capping ligands in a 1:1 ratio. Place-exchange was first described by Murray and co-workers,³² using alkanethiolate-clusters with ω -functionalized thiols in toluene. This reaction has since been expanded to aqueous solutions⁹ and can be carried out in aqueous buffer solutions. Multiple research groups have studied the dynamics by which place-exchange occurs in ligand solutions. According to Murray's work, the rate of ligand exchange depends both upon the concentration of incoming and exiting ligands, implying an associative (S_n2 -like) mechanism.³³ Lennox and co-workers,³⁴ on the other hand, report the reaction is zero-order with respect to the incoming ligand. Zerbetto's lab found that the associative mechanism is accurate, but that the interactions of the newly introduced chains interact

with multiple chains on the cluster, causing the kinetics to change as the reaction proceeds.³⁵

The reaction rate increases with smaller sized entering ligands and shorter chain length of the protecting ligand.³³ Consequently, it is favorable to place-exchange a large biomolecule (such as a peptide) with a small protecting ligand (such as tiopronin), although the process will proceed at a slower rate. It is still practical to place exchange similar sized ligands in shorter time courses, as will be shown later with small molecule wire-like molecules and small alkanethiols, but the extent of exchange is expected to be lower in these cases. Furthermore, it is important to consider that subtle differences in the structure of the incoming ligand, such as branching, can have a significant effect on both the rate of place-exchange, and the stability of the monolayer.³⁶ Additionally, it should be noted that the reaction proceeds more favorably at different sites on the core; vertex sites > edge sites > near-edge sites > terrace sites³³ as shown in Figure 4.

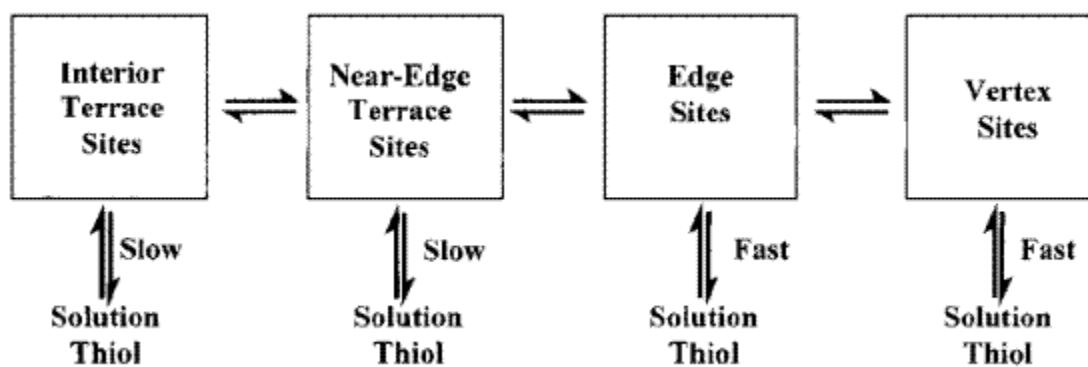


Figure 4: Chart of the different relative rates at which place-exchange and (possibly) migration occur. Copyright 1999 of the American Chemical Society.

The differences in reactivity due to thermodynamics and kinetics originate from the electron density differences³⁷ and steric accessibility differences³⁸ of these sites. These unique properties of nanoparticles lead to some degree of predictability, and therefore control, of where place-exchanged functional groups will anchor on the gold core. The rate of exchange is also increased by oxidative electronic charging of the core by electrochemical means³⁹ or in the presence of dioxygen.⁴⁰ The extent of reaction can be enhanced by increasing the incoming ligand concentration, but it should be noted that the extent of exchange rarely approaches 100%, due to the difficulty of exchange at terrace sites.³³

It is also important to note that the rate of ligand place-exchange on MPCs becomes slower as the particles age, probably due to a prolonged rearrangement of the ligands on the surface.⁴¹ To date, no kinetic or mechanistic study of place-exchange has considered new findings about the presence of gold thiolate tetramer rings on the surface of MPCs as reported by our group using mass spectrometry²⁷ and Häkkinen and co-workers in a theoretical paper.⁴² These nuances in surface structure could help to better explain the complexities of the place-exchange mechanism.

More recently, a number of crystal structures of thiolate protected nanoparticles^{43, 44} have been published, revealing that terrace, vertex, and edge sites, as described earlier, may not be as important as ring and staple⁴⁵ structures that project out of a tightly packed, central core (termed the “grand core”). It should be noted, however, that the available crystal structures describe smaller cores than those commonly used, and the vertex, edge, terrace description may hold more relevance for these materials.

It is difficult to use first principles to predict the extent and location of place exchange. In practice, a place exchange study in sufficient excess of incoming ligand to the protecting monolayer (*e.g.* 10-50 fold in excess of protecting groups in solution) over a long reaction time (*e.g.* 3 to 7 days) is used. This allows for determination of the “feed ratio” that is required for a given exchange percentage, and conditions can be tuned either by varying the reaction time or ligand concentration. Once exchanged, there is not a straightforward technique to determine the location of the exchanged ligands. Recent efforts by Harkness and coworkers have, however, led to the development of a method for the determination of ligand microstructure on the surface of a polyfunctionalized nanoparticle.⁴⁶

As an alternative to the solution phase place-exchange discussed above, Huo and coworkers have studied solid phase place-exchange reactions. In their original report of a solid phase place-exchange reaction, they employ a polystyrene Wang resin with acetyl protected 6-mercaptohexanoic acid attached via an ester bond.⁴⁷ The thiol groups are deprotected and allowed to undergo place-exchange with butanethiolate-protected gold nanoparticles, followed by washing away of unexchanged product, and cleaving of the exchanged particles. The same group has compared this solid phase approach to the solution phase approach and found the solid phase approach to be advantageous in terms of controlling the number of ligands attached per cluster and preserving the order of ligands on the surface.⁴⁸ Recently, the same group has reported a solid phase approach using a non-covalent interaction of the incoming ligand with silica gel⁴⁹ (see Figure 5).

the case of proteins, the inclusion of terminal cysteine residues during the synthesis of peptides, and the conversion of phosphates to phosphorothioates using 3H-1,2-benzodithiole-3-one 1,1-dioxide.⁵² It is also possible to introduce ligands into the MPC monolayer which undergo electrostatic interactions with biomolecules, for example, the use of biotin-streptavidin interaction or biotin-anti-biotin interaction.⁵³ All of these routes provide straightforward methods to ready a group for place-exchange and create functional nanoparticles.

Following the place exchange reaction, the material consists of unbound thiols from both the incoming and outgoing ligands, consequently requiring an additional purification step. Removal of these impurities is a unique challenge as the different molecules not only have different preferences for solvents (in the case of classical wet chemical purification techniques) or pore sizes (in the case of a size-exclusion technique), but properties that are similar to the nanoparticle. Options that are explored in subsequent chapters are washing with a battery of solvents, solvent immersion and sonication on glass, suspension and centrifugation given the availability of a sufficient solvent for this purpose, suspension and precipitation from cold solvent, dialysis, and molecular weight cut-off centrifuge filters. Some other suggestions for purification are continuous free-flow electrophoresis,⁵⁴ and diafiltration.⁵⁵

Besides the place-exchange strategy, there are other strategies to functionalize MPCs. An important class of these strategies, which is beginning to gain popularity, is the use of simple organic reactions on ligands already bound to the MPC. Examples include triazole cycloaddition to a bromine functionality⁵⁶ and direct functionalization of a

hydroxyl group,⁵⁷ amide coupling and ester coupling.⁵⁸ All of these methods allow for post-exchange reaction chemistry to occur, yielding surfaces that can be modified in a controlled fashion.

Another popular option, not explored in this dissertation, is polyfunctionalization *in situ*. When the properties of the given ligands will allow it, a mixed ligand nanoparticle synthesis is also an option. Mixed ligand synthesis refers to a reaction where a certain percentage mixture of two or more thiolated ligands are added to the gold salt prior to reduction, resulting in polyfunctionalized nanoparticle similar to those produced via place-exchange. Mixed ligand synthesis has the advantage of not requiring additional mixing and purification steps, but it is more difficult to control the pre-reduction chemistry and therefore more difficult to control the extent of exchange.

Characterization Methods for MPCs

A thorough characterization of mono- and polyfunctionalized nanoparticles is critical before applying them in biological or materials uses. Determination of core size (greater than about 1 nm, depending upon the substrate used) and dispersity is easily accomplished via transmission electron microscopy (TEM).⁴ Core sizes have also been determined by mass spectrometric methods, but this is limited to smaller cores with charge carrying ligands.^{59, 60} Scattering techniques and zeta-potential instruments are not as helpful for this class of nanomaterial due to the complexities that come with combined absorbance and scattering. Thermogravimetric analysis (TGA)⁶¹ provides an easy

method to determine the ratio of organic ligand to inorganic core material. Combining the core size and organic/inorganic ratio data yields an approximate average molecular formula for homofunctionalized nanoparticles.⁶⁰ Nuclear magnetic resonance spectroscopy (NMR) is useful for determining the structure and composition of the protecting monolayer, as well as the purity of the final material. Protecting ligands have broadened peaks in both ^1H and ^{13}C spectra due to spin-spin relaxational (T_2) broadening, dispersity in binding sites, and dipolar broadening due to packing density gradients.^{62, 63}

Once functionalized into a useful conjugate material, it is critical to characterize MPCs in terms of the quantity of biological relevant functional groups attached per cluster (on average) and the secondary structure of the biomimics post-conjugation. ^1H NMR is a simple way to semi-quantitatively determine the number of antigen peptides per cluster via integration of known protecting ligand peaks versus new broadened biomolecule peaks. The accuracy of this method can be enhanced through the use of I_2 -induced MPC decomposition (termed the “death reaction”) which leads to sharper peaks with less overlap.⁶⁴ A newer technique that has been developed in our group for relative surface quantitation of polyfunctionalized nanoparticles is matrix assisted laser desorption ionization-ion mobility-mass spectrometry (MALDI-IM-MS).⁶⁵ This specific mass spectrometric technique has the advantage of sorting out impurities with small collisional cross sections from the gold complexes actually used to quantify the surface (see the methods section of Chapter IV for more information). Secondary structure determination has proven to be more difficult. Drobny and co-workers describe the use of novel solid-state NMR techniques to investigate the secondary structure of peptides immobilized on

gold MPCs via amide coupling.⁶⁶ In an elegant study, they were able to use cross-polarization magic angle spinning (CPMAS) with double-quantum dipolar recoupling with a windowless sequence (DQDRAWS) to show that a peptide maintained a helical structure upon conjugation, but with a slight change in backbone torsion angle. Mandal and Kraatz recently described similar characterizations of peptides place-exchanged onto MPCs using Fourier transform infrared spectroscopy (FT-IR) and Fourier transform reflection absorption spectroscopy (FT-RAIRS).⁶⁷ Using amide I bands, they were able to observe that the secondary structure of a leucine rich peptide bound to gold transitions from α -helical to β -sheet with greater surface curvature. Helix forming free peptides, 2D SAMs on gold, and peptides on 20 nm gold MPCs (less curvature) showed α -helical structure while 10 nm, and especially 5 nm gold MPCs (more curvature) showed increasing amounts of β -sheet conformation. An excellent review of characterization techniques for peptide-nanoparticle conjugates was written by Slocik and Naik.⁶⁸ In this review, they describe a number of methods based on NMR, CD, FT-IR, and binding assays to reveal or confirm secondary structure of the conjugated peptides. Consideration of these techniques should prove vital in improving the characterization quality of biomolecule conjugated nanomaterials in our research group.

Methods

Instrumentation for Routine Nanoparticle Characterization

Nanoparticle characterization was accomplished with a variety of instrumentation. ^1H NMR spectra for synthetic characterization and purity confirmation were collected using a Bruker AV 400 MHz NMR. Surface ligand quantitation was accomplished with Bruker DRX 500 MHz, and AV 600 MHz instruments. Ultraviolet/Visible spectroscopy was performed using a Cary 100 Bio UV/Visible spectrophotometer. Thermogravimetric analysis (TGA) was performed in the Vanderbilt Institute of Nanoscale Science and Engineering (VINSE) Biomolecular Nano-Structure lab using an Instrument Specialist's TGA 1000 with N_2 or air as the chamber gas. Transmission electron microscopy was performed using a Philips CM20 TEM with a LaB_6 tip operating at 200 kV. Samples are prepared by a variety of methods on formvar or ultrathin holey carbon supported on copper mesh grids, purchased from Ted Pella.

CHAPTER II

LINEAR EPITOPE MAPPING APPROACH TO LOCATE BINDING “HOT SPOTS” IN THE CONFORMATIONAL ANTIGENIC SITE A OF HUMAN RESPIRATORY SYNCYTIAL VIRUS (HRSV) FUSION PROTEIN (F)

Introduction

Having discussed the synthesis and characterization of thiolate protected nanoparticle synthesis, the application of these materials in a biological context will be discussed. The question, “How can you make a small gold nanoparticle resemble a protein in a way that it “tricks” a system into thinking that it really is one?” will be asked. Some answers to this question will be covered in the next two chapters. Chapter II deals with a biological system that is mimicked, and the results of that study are important to the construction of a bio-nano-conjugate material, discussed in Chapter III. Specifically, the research aimed to determine which piece of a full protein is necessary to achieve a specific function. In the current case, it was desirable to know which peptide segment from HRSV F protein is necessary for recognition of a specific antibody and whether it still behaves in the same way when not part of the native protein. Furthermore, the impact of removing or adding amino acids in a stepwise fashion on the strength of the recognition was studied. The effect of removing and adding terminal amino acids was initially probed using the quartz crystal microbalance, and later with enzyme-linked immunosorbant assay (ELISA).

It is important to note that, ultimately, this research came together in a non-linear fashion. Summarily, preliminary experiments with the QCM to examine the antibody binding properties of relevant peptides were attempted with little success, prompting the research to pursue peptide conjugated nanoparticles not informed by epitope mapping experiments. Having not found a strong, specific nanoparticle biomimic in the first round of experiments, epitope mapping was revisited with ELISA. The second round of epitope mapping resulted in more informative data, presented in this chapter, which allowed for construction of an improved nanoparticle mimic. The improvements and results to the nanoparticle mimic are presented in Chapter III. The results were then put back together in a more readable account of the research than if they were presented chronologically. Therefore, while experiments from Chapter II and III alternate in time and inform each other, they are more cohesive in the current structure.

Background

Human Respiratory Syncytial Virus

Acute respiratory tract infection is the leading cause of death by infectious disease worldwide and HRSV is the leading cause of acute respiratory tract infection in infants.⁶⁹ A 13-year surveillance of Washington DC infants and young children showed that HRSV was present in 43% of patients with bronchiolitis and 25% of patients with pneumonia.⁷⁰ Diagnosis of HRSV can be difficult during the cold season due to an increased patient load, especially given the high volume of young patients with associated symptoms from

other infections. The insufficient pace of clinical diagnosis often results in longer than necessary hospital stays for afflicted children and their families, and an increased financial burden for hospitals. Our research group is focused on strategies to develop quick and accurate diagnostic platforms, to analyze immunological interactions of HRSV with the commercial pharmaceutical IgG Palivizumab (PZ), and to design biological mimics of this immunological interaction.

The HRSV virion is in the family *Paramyxoviridae* and of the order *Mononegavirales*, making it a non-segmented negative sense RNA virus.⁶⁹ HRSV is in the subfamily *Pneumovirinae* along with bovine respiratory syncytial virus (BRSV), pneumonia virus of mice (PVM), and avian and human metapneumovirus (AMPV and HMPV).⁶⁹ The diversity in this family of viruses allows researchers to tune strategies developed for one virus to a number of different diseases because of structural similarities.

A general understanding of the protein structure and function is vital to understanding the goals and approaches of this project. A structural schematic of HRSV is shown in Figure 7.

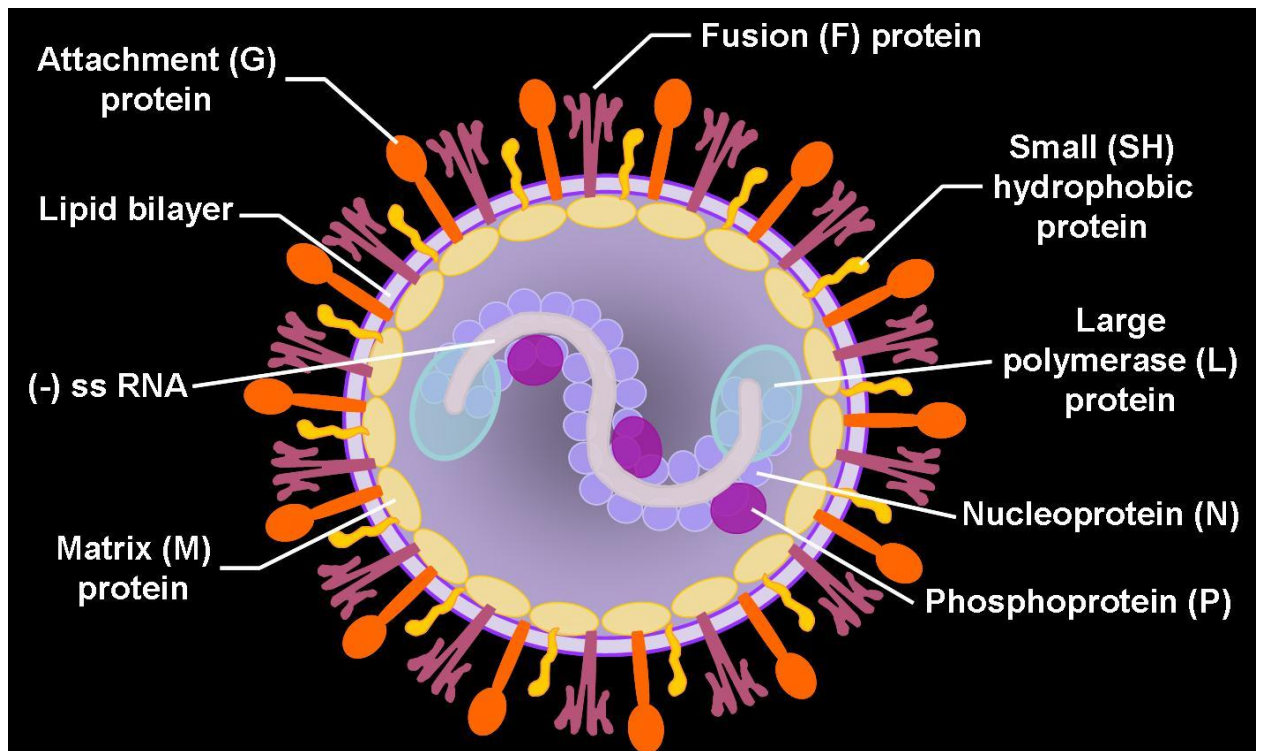


Figure 7: Cartoon schematic of an HRSV virion. The RNA and associated proteins are housed by a matrix protein which is covered with a protective lipid bilayer. The lipid bilayer projects three different surface glycoproteins that are important targets for the immune system: fusion (F), attachment (G), and small hydrophobic (SH). Figure from the Katholieke Universiteit Leuven, used with permission.⁷¹

The viral genome encodes three surface glycoproteins (fusion [F], attachment [G], and a small hydrophobic protein [SH]). Also encoded are a non-glycosylated matrix protein (M), a nucleoprotein (N), a phosphoprotein (P), transcription processivity factors, two non-structural proteins, and a large viral RNA polymerase unit (L). The structure of the virion houses a nucleoprotein/RNA complex payload at its core (L, N, P and possibly transcription processivity factors).⁶⁹ The RNA is thought to be surrounded by a protective coat of M. HRSV is an enveloped virus; therefore it collects a lipid bi-layer upon

budding from infected cells, making it more difficult for the immune system to recognize and destroy. The three surface glycoproteins project from the surface of this envelope as 11-20 nm spikes spaced at about 6-10 nm apart.⁶⁹ The total size of the virus varies from 100-350 nm diameter spherical particles to 10 µm long filamentous particles having a radius of 60-200 nm.⁶⁹ Analysis of the proteins encoded for by HRSV RNA has allowed researchers to identify appropriate targets for detection and treatment strategies.

Of all the encoded HRSV proteins, F and G are the only two that induce neutralizing antibodies, as steric hindrance at certain areas of these sites will block cell entry.⁷² The importance of the third surface glycoprotein (SH) is not clear, and it has been shown to be non-essential both *in vitro* and *in vivo*.^{73,74} G is important for viral attachment and F accomplishes viral fusion; therefore, if an antibody binds either one of these antigens at an epitope that is simultaneously involved in a critical function, viral replication will be neutralized by sterics and the prevention of necessary conformational changes.

Consequently, a wide variety of neutralizing monoclonal antibodies are known for each. G, which is heavily glycosylated, has a highly variable amino acid sequence from strain to strain, whereas neutralizing antibodies targeted against F are cross reactive between various strains and across antigenic subgroups.⁷⁵ These properties render F a superior target for antibody-based detection strategies.

In the absence of an available crystal structure of HRSV F protein, the best resource to gain structural insights to aid this project is a Newcastle Disease Virus (NDV) fusion protein homology model of HRSV F.^{76,77} A structural schematic of the protein illustrates the trimeric structure, and presence of stalk, neck, and head regions (see Figure 8).

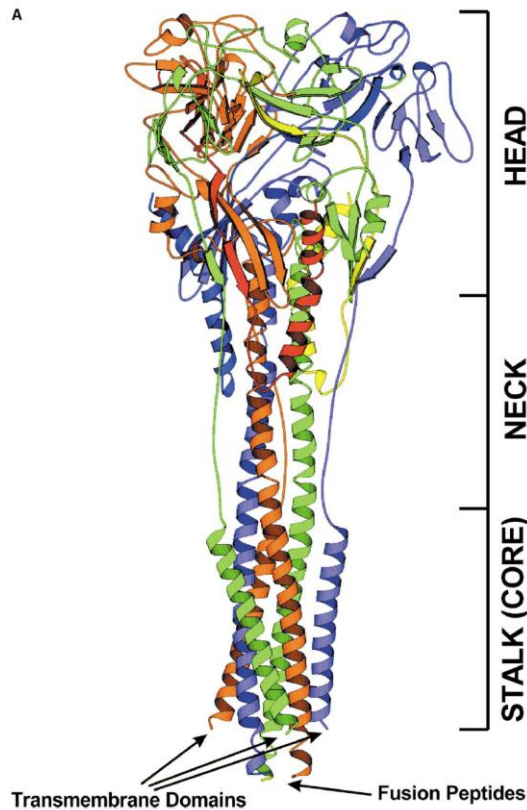


Figure 8: HRSV F protein, showing the head, neck, and stalk structure. The head docks with the cell wall during infection, and is the site of epitopes for neutralizing mAbs. Figure from Morton, *et. al.*⁷⁶ Copyright 2003, Elsevier, used with permission.

Competitive binding studies of HRSV F using libraries of monoclonal IgG's have revealed three unique antigenic sites (A, B, C) with various epitopes (including one in a bridge site AB).⁷⁸ The A and C sites are conserved while the B site is variable.⁷⁸

Monoclonal antibody resistant mutants (MARMs) in the A site are understood in terms of specific amino acid changes. Coincidentally, a number of MARMs of RSV type A exhibit amino acid changes between residues 258 and 276.^{75, 78-85} Specific amino acid

changes in the F protein of RSV type A MARMs are shown in Table 1 with reference as to which monoclonal antibody was used to select the MARM.

Table 1: Summary of reported HRSV escape mutations in HRSV F antigenic site A. The colored boxes refer to the study in which the escape mutation was reported: Crowe,⁸⁵ M or Q from Zhao and Chen 2004,⁸¹ I from Zhao; Chen; Megaw 2004,⁸⁰ R from Zhao 2005,⁸³ Suzich,⁸⁴ Beeler,⁷⁸ Arbiza.⁷⁵

Position	262	263	264	265	266	267	268	269	270	271	272	273	274	275	276	277
Residue	N	D	M	P	I	T	N	D	Q	K	K	L	M	S	N	N
other mAb	S										N					Y
Fab 19					M											
mAb 1129															F	
PZ	S						I				Q				F	Y
	Y										M					
	K										R					
											E					
											N					
											T					
											D					
	Crowe															
	Sullender	M or Q from Zhao and Chen 2004														
		I from Zhao; Chen; Megaw 2004														
		R from Zhao 2005														
	Suzich															
	Beeler															
	Arbiza															

Epitopes in antigenic site A are conformational epitopes, and are, therefore, difficult to mimic in such a way that elicits antibody binding similar to the native structure.^{75, 78}

Failure to reproduce to secondary structure is further compounded when the epitope is highly discontinuous.

Synagis, often called by its pharmaceutical name Palivizumab (PZ), is prescribed to prevent HRSV infection in children during the cold season, and is commercially available from MedImmune. This designer monoclonal pharmaceutical IgG is a humanized form of murine monoclonal antibody (mAb) 1129,⁷⁸ where certain regions are identical to the murine structure to conserve the structural integrity of the binding sites, and the rest of

the mAb is that of a well characterized human mAb MCPC603.^{86, 87} Palivizumab was determined to have at least as strong of an affinity for RSV F as chimeric 1129 via ELISA.⁸⁶ The commercial availability of this mAb and its high affinity for RSV F protein makes it a desirable tool for constructing immunosensors, mapping HRSV F epitope sequences, and screening antigenic mimics (see Chapter III) presenting HRSV F epitope peptides.

Since this study was completed, crystal structures of HRSV F in complex with mAb F101,⁸⁸ post-fusion HRSV F,⁸⁹ and the HRSV F motavizumab peptide epitope bound to the antigen-binding fragment (Fab) of motavizumab⁹⁰ have been published.

Motavizumab is the next generation of PZ, with 10 fold higher activity but the same epitope region.⁹¹ These crystal structures should prove instrumental in understanding the structural basis of the antigen-antibody interaction, and will aid future efforts to construct biomimetic agents.

Epitope Mapping

In the construction an antigenic mimic, it is useful to understand the specific intermolecular forces that are responsible for binding HRSV F to PZ. Specifically, the goal is to determine which amino acid side chains are involved and how they are spatially organized. Given this information, a nanomaterials scientist can imagine and create a synthetic system which copies the important parameters without the need to use complicated techniques, expensive and fragile biological systems, and exotic reagents.

Epitope mapping describes any technique where antigens or fragments thereof are analyzed for their affinity to an antibody in order to gain information about which parts of the whole are important for the antigen-antibody interaction. Linear epitope mapping refers to techniques which solely interrogate primary structure while conformational epitope mapping considers the effects of secondary and tertiary structure as well. In the current study, a linear epitope mapping approach to investigate synthetic antigenic site A peptides against PZ was used, but information about the secondary structure was inferred from other studies.

The discovery by Rutledge and coworkers of binding “hot spots” in a proposed long C-terminal epitope sequence of Ebola glycoprotein⁹² lead this research to apply similar methodology to antigenic site A of HRSV F. Briefly, the researchers discovered that there were two discrete regions in a longer peptide sequence which had local maxima in an ELISA assay against the monoclonal antibody 15H10 that appeared to be centered about two spatially distinct three amino acid sequences, as is shown in Figure 9.

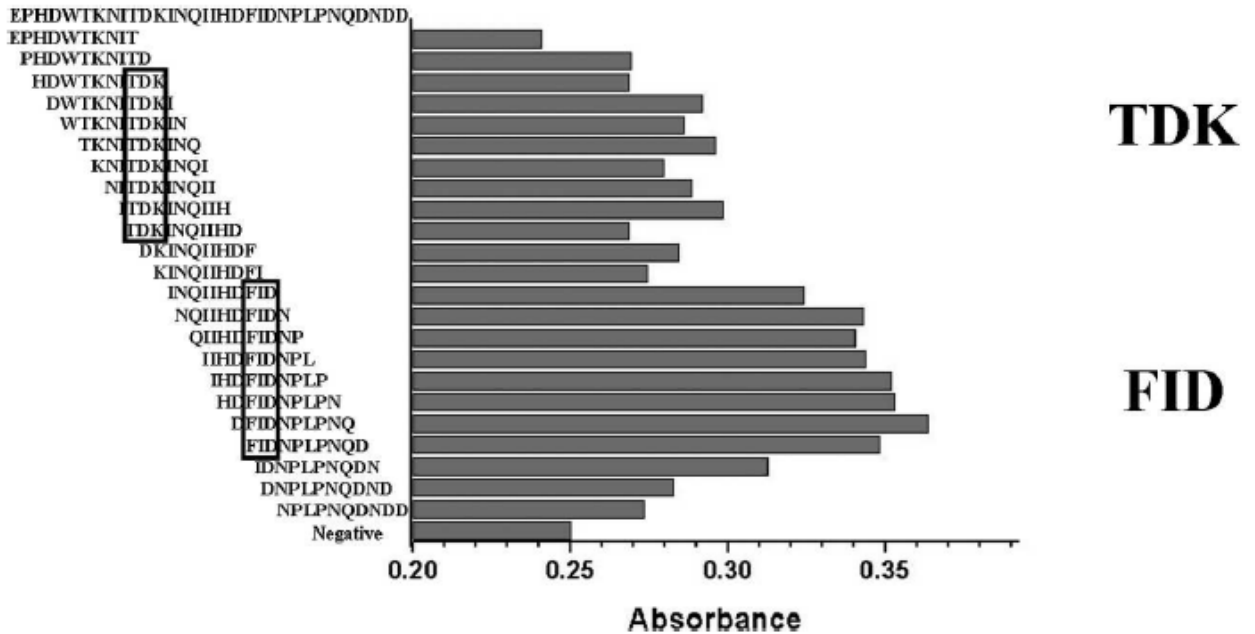


Figure 9: ELISA study of synthetic peptides from Rutledge and coworkers demonstrating that two spatially separate three amino acid sequences are likely to provide the strongest interactions between the glycoprotein of Ebola and the antibody 15H10.⁹² Copyright 2008, the Materials Research Society, used with permission.

These “hot spots,” TDK and FID, were validated by place exchanging cysteine-PEG terminated versions of the three amino acid sequences onto tiopronin protected gold nanoparticles and detecting them with a home-made Ebola QCM immunosensor presenting 15H10.

Quartz Crystal Microbalance (QCM)

The QCM consists of a piezoelectric quartz resonator with metal electrodes on either side. The combination of electrodes and resonator is attached to an oscillator circuit. QCM has become a useful analytical technique due to the linear relationship between

mass deposited on the crystal and the frequency of the crystal resonance.⁹³ Oscillator circuits that permit liquid measurements have made the technique useful in the area of bioanalytical chemistry.^{94,95} The ideal oscillator for this technology is quartz because it has desirable mechanical, electrical, chemical, and thermal properties.⁹⁴ Specifically, AT-cut quartz crystals have a temperature coefficient that is nearly zero between 0 and 50 °C, making them ideal for QCM measurements at ambient temperatures without sophisticated temperature control.⁹⁶

Electrode wrapped quartz crystals manufactured by Maxtek Inc. resonate at different frequencies depending upon their thickness. Conventionally, quartz crystals used in QCM measurements are identified on the basis of this resonant frequency. For example, a 5 MHz QCM crystal is 333 μm thick and a 9 MHz QCM crystal is 185 μm thick. The crystals are 1" in diameter, the oversized front electrode is $\frac{1}{2}$ " in diameter and the concentric electrode located on the reverse side (contact electrode) is $\frac{1}{4}$ " in diameter.⁹⁷ The overlapping area of the contact electrode and front electrode is 0.3419 cm^2 . The overlapping region has been shown to be the sensitive area by scanning electrochemical mass sensitivity experiments.⁹⁸ The consequences of this are that deposited mass (mass added to the crystal by covalent, electrostatic, physical etc. interactions) has a maximum effect on resonant frequency in the overlapping region and a small effect outside of the overlapping region (known as field fringing). Such an electrode geometry sacrifices some sensitivity in order to negate fringing field effects from non-specific binding on the quartz itself.⁹⁹ Fringing field effects refer to mass loading that is outside of the fully overlapping area between the two electrodes that still affects the electric field and thus

elicits a small, but significant effect on crystal frequency. The manual for the Maxtek RQCM cites that the particular electrode geometry (small contact electrode with an oversized sensing electrode) was chosen to ensure a “more consistent deposition across the active area of the crystal.”⁹⁷

In order to calculate mass loading using the QCM, one takes advantage of the following relationship between mass and frequency shift, proposed by Sauerbrey and henceforth named the Sauerbrey equation:

$$\Delta f = C_f \Delta m \quad (2-1)$$

where Δf [Hz] is the frequency shift of the quartz crystal, Δm [kg] is the mass loaded onto the crystal, and C_f is known as Sauerbrey’s sensitivity factor and has units of Hz kg⁻¹.⁹³

Sauerbrey’s sensitivity factor is defined by the following equation:

$$C_f = \frac{-2f_0^2}{A\sqrt{\rho_q\mu_q}} \quad (2-2)$$

where f_0 is the first harmonic resonant frequency of the unloaded crystal, A is the active (sensitive) area [m²] of the QCM crystal, ρ_q is the density of quartz (2.648 kg/m³) and μ_q is the shear modulus of AT-cut quartz (2.95 x 10¹¹ N/cm²).^{93,97} The sensitive area, again, is the overlap area of the large front electrode with the small rear electrode. C_f for our crystals are 0.0566 Hz cm²/μg for a 5 MHz crystal and 0.1834 Hz cm²/μg for a 9 MHz crystal. When calculating mass, it is important to recognize that frequency is not

dependent upon mass loading alone in a liquid system. Viscosity has a major effect on the frequency, as shown by the following equation:

$$\Delta f = -f_q^{3/2} \sqrt{\frac{\eta_L \rho_L}{\pi \mu_q \rho_q}} \quad (2-3)$$

where η_L [N s m⁻²] is the viscosity of the liquid in contact with the crystal, and ρ_L is the density of the liquid in contact with the crystal.¹⁰⁰ This specific component of the total frequency change is directly related to a change in resistance, given by the following equation:

$$\Delta R = \Delta f \frac{2\pi(\rho_q \mu_q)^{3/2}}{32f^3 A_r (\rho_q e_{26})^2} \quad (2-4)$$

where ΔR [Ω] is the change in resistance, and e_{26} [kg V s⁻²] is the piezoelectric constant of quartz.^{100, 101} Therefore, frequency shift due to viscosity can be calibrated to separate frequency due to mass loading by use of solutions of a non-loading analyte, such as sucrose, leading to a concentration dependent decrease in frequency, which results from viscosity. The slope of a plot of Δf versus ΔR is used as a correction factor to subtract out viscosity induced frequency shift.

The practical equation to be used for data analysis in the current studies involves first rearranging equation 2-1:

$$\Delta m = \frac{\Delta f}{C_f} \quad (2-5)$$

Subtracting out frequency due to resistance yields:

$$\Delta m = \frac{\Delta f - (\Delta R c)}{C_f} \quad (2-6)$$

where c is the calibration factor in units of Hz/ Ω attained from the plot of frequency versus resistance for solutions of varying viscosity. The value for c should be independently determined for each crystal used. Typical c values for the Maxtek crystals used in this research are 2.095 Hz/ Ω for a 5 MHz crystal and 15.3 Hz/ Ω for a 9 MHz crystal.

QCM data can also be used to extract thermodynamic parameters for the systems being studied. For the generic system $Ag + Ab \rightleftharpoons AgAb$ where Ag is an antigen and Ab is an antibody, the equilibrium constant, K , is defined by:

$$K = \frac{[AgAb]_{eq}}{[Ag]_{eq}[Ab]_{eq}} \quad (2-7)$$

K can be determined from mass loading data using either of the following equations:

$$\Delta m = -K^{-1} \left(\frac{\Delta m}{C} \right) + \Delta m_{max} \quad (2-8)$$

$$\left(\frac{C}{\Delta m} \right) = \left(\frac{C}{\Delta m_{max}} \right) + \left(\frac{1}{K \Delta m_{max}} \right) \quad (2-9)$$

where C is the adsorbate concentration, and Δm_{max} is the maximum mass that can be adsorbed by the monolayer, and $\Delta m / \Delta m_{max} = \Theta$, the degree of surface coverage.¹⁰²

Determination of K from either of the above equations (8 or 9), allows calculation of the Gibb's free energy of adsorption, ΔG°_{ads} using the following equation:

$$\Delta G^{\circ}_{ads} = -RT \ln K \quad (2-10)$$

where R is the gas constant and T is the temperature of the system. Studying the variation of the system with temperature, the enthalpy of adsorption, ΔH°_{ads} , can be determined using the following equation:

$$\left[\frac{d \ln K}{d(1/T)} \right] = \frac{-\Delta H^{\circ}_{ads}}{R} \quad (2-11)$$

Finally, determination of the entropy of adsorption, ΔS°_{ads} , can be determined using the following equation:

$$\Delta S^{\circ}_{ads} = \frac{(\Delta H^{\circ}_{ads} - \Delta G^{\circ}_{ads})}{T} \quad (2-12)$$

The full process from data collection to thermodynamic quantities is rigorous, but allows for determination of whether various biological processes are entropy or enthalpy driven. Thermodynamic understanding, in turn, allows for better understanding of the structure-function relationship in biological molecules. From an evolutionary perspective, this allows researchers to understand how a protein used to be structured, what modifications it made to get where it is, and exactly how those changes made the protein function better than its predecessor.

The ability to determine real time kinetic and thermodynamic parameters is only one aspect that makes the construction of QCM based immunosensors desirable. QCM also had the advantages of low cost, portability, and a number of analytical advantages. A good case for comparison is surface plasmon resonance (SPR). Whereas QCM uses acoustic waves and measures frequency, SPR uses optical waves and measures reflection minimum. Either instrument provides data that can be used to study protein interactions in real time. SPR performs at least as well as QCM in terms of detection limit, sensitivity, and detection time;^{103, 104} however, QCM instrumentation is less expensive (about \$5,000 compared to about \$100,000 for the lowest specifications of either instrument) and, reportedly, easier to use, and can make measurements on thicker layers without loss of sensitivity (200 nm for SPR versus 400 nm for QCM).¹⁰⁵⁻¹⁰⁷ Either technique measures up well in terms of analytical figures of merit when compared to many techniques employed in the field. In terms of time consumption, culture of a nasal swab takes about four days for detection and polymerase chain reaction (PCR) takes one to two days for detection. Rapid ELISA techniques can be employed with total analysis time of 30 minutes to 1 hour, but the cost to the patient is about \$300.00 per test, and the pieces, such as antibody solutions and control samples, are not reusable.¹⁰⁸ The cost could be lowered by a platform like QCM or SPR because of their amenability to reusability, as solid-phase stabilized biomolecules have longer shelf lives. Additionally, all of the above techniques are largely qualitative or semi-quantitative at best, and therefore give less information about total viral load. The dominant RSV immunoassay in the clinical environment, direct fluorescent antibody (DFA), takes about 2 hours.¹⁰⁹ A QCM

immunosensor that is reusable should be much quicker and cheaper than this technique, while providing more information about the disease.

Methods

Instrumentation

Solution phase resistance and frequency measurements to characterize biological interactions were made using a Maxtek, Inc. 3-channel Research QCM operating at a driving voltage of 125 mV RMS and using Maxtek 5 or 9 MHz AT-cut quartz crystals with gold electrodes. Flow cells were also purchased from Maxtek. Solutions were delivered through the flow cells using a Cole Parmer Masterflex console drive peristaltic pump.

Materials

Reagent and optima grade solvents, N-2-mercaptopropionylglycine (tiopronin), bovine serum albumin (fraction V, 96%), tween-20 (molecular biology grade), α -cyano-4-hydroxycinnamic acid, 3,3',5,5'-Tetramethylbenzidine (TMB, liquid substrate, super-sensitive, for ELISA), thioanisole, and anisole were purchased from Sigma-Aldrich. Common laboratory salts and concentrated ammonium hydroxide were reagent grade and purchased from Fisher scientific. Concentrated sulfuric acid was purchased from EMD. Absolute ethanol was purchased from Pharmco-AAPER. Immulon 2HB well plates,

maleimide coated well plates, and cysteine-HCl were purchased from Thermo scientific. Hydrogen peroxide (30% v/v) was purchased from Acros. Peptide synthesis materials (f-moc protected and side-chain protected amino acids, coupling reagents, and resins) were provided generously by the research group of David Wright. 18 M Ω Water was obtained from a U.S. Filter Modulab water system with a 0.2 μ m external filter, or from a Barnstead NANOpure Diamond water purification system. Dry nitrogen is provided in house. Monoclonal antibody 1214, 1129, Palivizumab, and human respiratory syncytial virus were provided generously by the Dr. James Crowe, Jr. research group. Work areas that contained HRSV were cleaned thoroughly with bleach and 70% isopropyl alcohol solution.

Peptide Synthesis

Most peptides were synthesized by standard solid phase f-moc procedures using an Apex automated peptide synthesizer. The series of peptides used in the QCM experiments were synthesized, purified, and characterized by Malgorzata Broncel. Subsequent peptides that were utilized in the ELISA experiments were synthesized by Joshua Swartz. The peptides were cleaved from the resin and side-chain-deprotected using Reagent R (90% trifluoroacetic acid, 5% thioanisole, 3% ethanedithiol, 2% anisole). Following extraction in cold diethyl ether with cold centrifugation (0° C), cleaved peptides were further purified using a Waters semi-prep HPLC with a reverse phase column in a continuous gradient of water:acetonitrile following injection in water/acetonitrile/dilute

ammonium hydroxide. Samples were collected with a Waters fraction collector, operated manually. (Note: ammonium hydroxide must be used sparingly, < 100 mM, to avoid damaging the column or corroding the pumping lines). Following lyophilization, peptides were diluted in 20% acetonitrile and water, occasionally with the addition of ammonium hydroxide to increase solubility, and characterized by MALDI MS on a Voyager MALDI mass spectrometer with α -cyano-4-hydroxycinnamic acid.

Characterization data for peptides used in this study that were not fully characterized by other coworkers are displayed in Table 2.

Table 2: Tabulated characterization data for peptides purified by this author. The data has been relocated to Appendix D.

[Located in Appendix D]

Formation of peptide SAMs

Clean gold electrode surface was achieved by mixing 3 drops concentrated sulfuric acid to 1 drop 30% hydrogen peroxide (piranha) on the gold electrode three times, each time completely covering the surface and rinsing away with deionized water. The crystal was then rinsed with copious amounts of absolute ethanol and blown dry with cool nitrogen. Self-assembled monolayers (SAMs) of RSV F A site peptides terminated with cysteine were created on the surface of QCM crystal electrodes by soaking the crystal face in a mixture of 3 parts tiopronin to 1 part peptide (1 mM combined) solution in absolute ethanol with a minimum of deionized water (to aid solubility). The peptide/tiopronin

solution was immediately transferred to the QCM crystal in a glass cell clamped on top of the oversized gold electrode. The total time of soaking varied from 3 to 24 hours. The solution was then discarded and the crystal rinsed with copious amounts of absolute ethanol and blown dry with cool nitrogen.

QCM experiment

The QCM crystal presenting the SAM on the gold electrode, or just the clean gold presenting crystal was placed in a flow cell interfaced with the Maxtek, Inc. RQCM. Phosphate buffer solution (25 to 50 mM sodium phosphate with 0 to 150 mM sodium chloride pH adjusted to 7.1) was pumped across the crystal face in a laminar flow until a minimum in frequency and resistance drift is measured. A ten-minute baseline was then collected. Following collection of a baseline, a solution of bovine serum albumin (BSA) (1 mg/mL) was switched with the buffer solution and pumped 5 to 10 minutes beyond when a decrease in frequency was observed. The buffer flow time assures that there are no available gold sites which could participate in non-specific binding. Buffer was then pumped in order to purge the system of BSA. Then, solutions of antibody in buffer (10-20 $\mu\text{g/mL}$) were flowed for 10 minutes and the frequency response was observed. All solutions were pumped at a flow rate of approximately 40 $\mu\text{L/min}$. The following peptide sequences in Table 3 were evaluated.

Table 3: Peptides designed to be evaluated by the QCM step-wise linear epitope mapping method. Odd numbered sequences were made to correlate QCM experiments with ELISA experiments in an Immulon well plate. Even numbered peptides are designed for the QCM experiment itself, having a cysteine residue for thiol linkage to the gold surface. Spaces allow for easy visualization of the stepwise differences between peptides. The amino acid numbering sequence for HRSV F protein is displayed in the top row. Known MARMs against PZ or related mAbs are indicated in bold orange. Residues that bind to motavizumab are indicated in bold blue.

ID Peptide Sequence

RSV F 255 260 265 270 275

| | | | |

- A) NSELLSL**IND**MP**ITND**Q**KKLMS****SNN** (not evaluated)
- 1) LSL**IND**MP**ITND**Q**KKLMS**
- 2) CLSL**IND**MP**ITND**Q**KKLMS**
- 3) SL**IND**MP**ITND**Q**KKLMS****N**
- 4) CSL**IND**MP**ITND**Q**KKLMS****N**
- 5) L**IND**MP**ITND**Q**KKLMS****SNN**
- 6) CL**IND**MP**ITND**Q**KKLMS****SNN**
- 7) I**ND**MP**ITND**Q**KKLMS****SNNV**
- 8) CI**ND**MP**ITND**Q**KKLMS****SNNV**
- 9) N**D**MP**ITND**Q**KKLMS****SNNVQ**
- 10) CN**D**MP**ITND**Q**KKLMS****SNNVQ**

ELISA Stepwise linear epitope mapping of the full length RSV F Antigenic Site A

Linear fragments and full length linear peptides of antigenic site A were evaluated for their ability to bind Palivizumab in a peptide ELISA assay using maleimide coated well plates. The design of the peptides has been improved by amination of the C terminus, and acylation of the N terminus to better represent the fact that the antigenic site A is an internal sequence. Serine-glycine-serine-glycine spacers were used in favor of PEG-6 for improved synthetic yield, solubility, and ease of purification. The following synthetic peptides were evaluated by the assay (Table 4 lists peptides used for the ELISA assay and Table 3 lists peptides used in the QCM assay):

Table 4: Peptides evaluated against palivizumab in an ELISA assay. Spaces allow for easy visualization of the stepwise differences between peptides. The amino acid numbering sequence for HRSV F protein is displayed in the top row. “Linker” indicates the inert CSGSG sequence added for peptide immobilization and projection. Known MARMs against PZ or related mAbs are indicated in bold orange. Residues that bind to motavizumab are indicated in bold blue.

ID Peptide Sequence

RSV F linker	255	260	265	270	275	linker
A	CSGSG	NSELLSLINDMP	ITNDQK	KLMS	NN	
B		NSELLSLINDMP	ITNDQK	KLMS	NN	GSGSC
1	CSGSG	NSELLSLIND				
2	CSGSG	SELLSLINDM				
3	CSGSG	ELLSLINDMP				

4	CSGSG	LLSLINDMPI	
5	CSGSG	LSLINDMPIT	
6	CSGSG	SLINDMPITN	
7	CSGSG	LINDMPITND	
8	CSGSG	INDMPITNDQ	
9	CSGSG	NDMPITNDQK	
10	CSGSG	DMPITNDQKK	
11	CSGSG	MPITNDQKKL	
12	CSGSG	PITNDQKKLM	
13	CSGSG	ITNDQKKLMS	
14	CSGSG	TNDQKKLMSN	
15	CSGSG	NDQKKLMSNN	
1b		NSELLSLIND	GSGSC
2b		SELLSLINDM	GSGSC
3b		ELLSLINDMP	GSGSC
4b		LLSLINDMPI	GSGSC
5b		LSLINDMPIT	GSGSC
6b		SLINDMPITN	GSGSC
7b		LINDMPITND	GSGSC
7	CSGSG	LINDMPITND	
8	CSGSG	INDMPITNDQ	
9	CSGSG	NDMPITNDQK	
10	CSGSG	DMPITNDQKK	
11	CSGSG	MPITNDQKKL	

12	CSGSG	PITNDQKKLM
13	CSGSG	ITNDQKKLMS
14	CSGSG	TNDQKKLMSN
15	CSGSG	NDQKKLMSNN
1b	NSELLSLIND	GSGSC
2b	SELLSLINDM	GSGSC
3b	ELLSLINDMP	GSGSC
4b	LLSLINDMPI	GSGSC
5b	LSLINDMPIT	GSGSC
6b	SLINDMPITN	GSGSC
7b	LINDMPITND	GSGSC

Results and Discussion

Peptide QCM step-wise linear epitope mapping

Self-assembled monolayers of synthetic peptide epitopes 2, 4, 6, 8, and 10 showed small (barely greater than three times the noise) amounts of mass loading when mAb 1214 (20 $\mu\text{g}/\text{mL}$) in PBS was flowed across the SAM. The small amount of mass loading was not observed when the electrode was blocked with BSA prior to antibody addition, suggesting that mAb 1214 binds to the gold electrode surface. Experiments demonstrating mAb 1214 binding to the clean gold surface of the QCM crystal confirmed this observation. There were significant amounts of mass loading observed when peptide epitopes were mixed with tiopronin prior to addition; however, this was later discovered

to be non-specific binding to tiopronin. 11-mercapto-1-undecanol and 6-mercapto-1-hexanol, as alternatives to tiopronin as a diluting agent, also exhibited significant amounts of binding to mAb 1214.

It was concluded that neither Synagis nor mAb 1214 binds self-assembled monolayers of synthetic peptide epitopes 2, 4, 6, 8, nor 10 on gold in a high ionic strength (200 mM salt) environment. Additionally, mAb 1214 and PZ fail to bind to synthetic peptide epitopes 1, 3, 5, 7, or 9 on Immulon. Possibly, mAb 1214 will not bind to the conformation adopted by the peptide on Immulon well plate, whereas it might bind to the same peptide in a different context.

Synagis was found to bind synthetic peptide epitope monolayers of 2, 8, and 10 on gold in a low ionic strength (50 mM salt) environment (4 and 6 were not evaluated due to a lack of remaining material) (Figures 10-12).

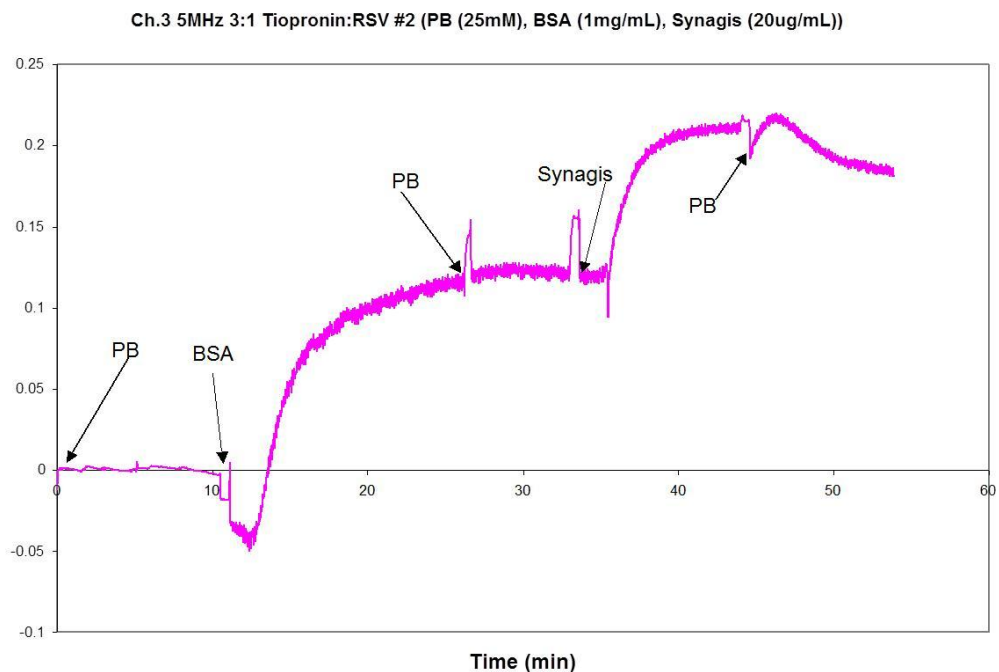


Figure 10: QCM graph illustrating the binding of BSA to bare gold and PZ to a mixed SAM of peptide 2 and tiopronin.

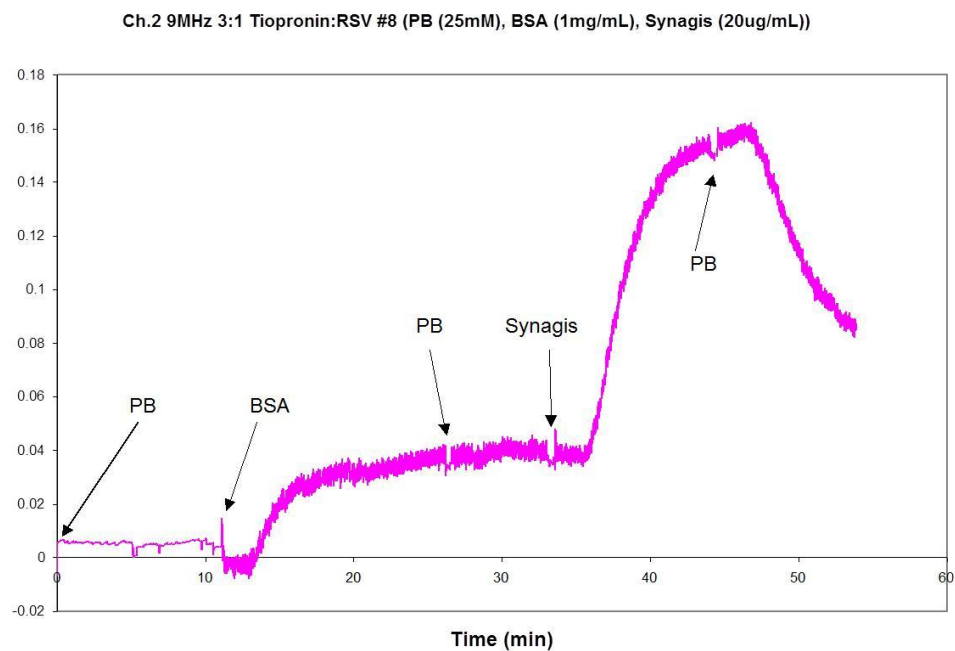


Figure 11: QCM graph illustrating the binding of BSA to bare gold and PZ to a mixed SAM of peptide 8 and tiopronin.

Ch.2 9MHz 3:1 Tiopronin:RSV #10 (PB (25mM), BSA (1mg/mL), Synagis

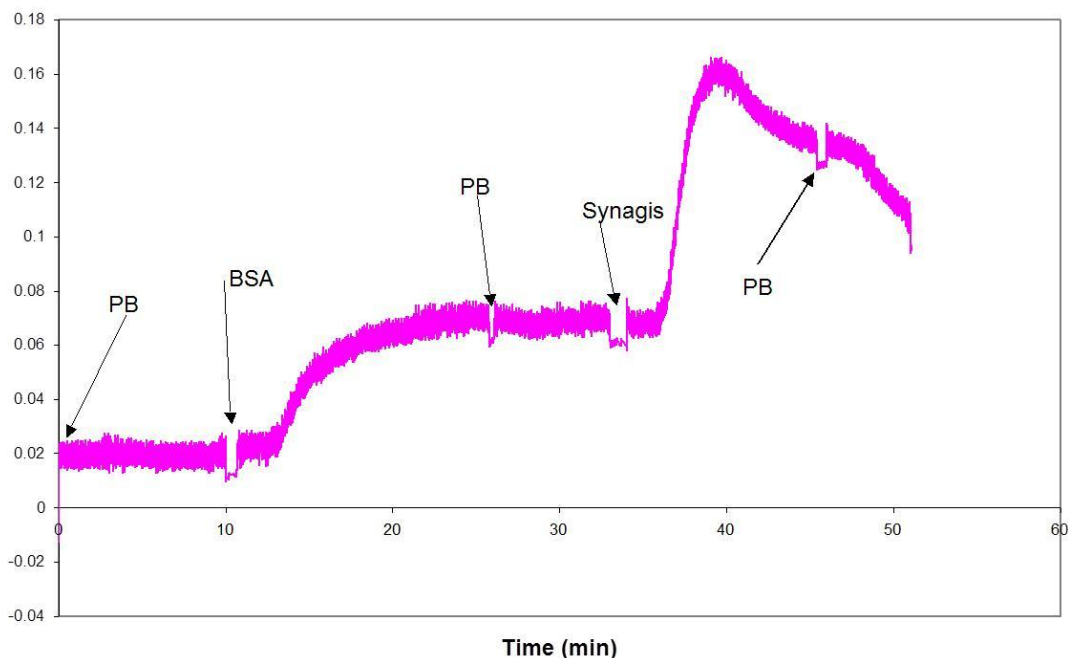


Figure 12: QCM graph illustrating the binding of BSA to bare gold and PZ to a mixed SAM of peptide 10 and tiopronin.

All three of these epitopes demonstrated a reversible binding event with Synagis, which differs from the irreversible binding of synagis with the diluting agent, tiopronin. Of particular interest, Synagis bound in a highly reversible fashion to peptide 8 (Figure 11). Reversible binding can be associated with biological activity. At the very least, it distinguishes itself from the other peptides. To be sure that the binding is specific, a new diluting agent that does not bind Synagis must be evaluated and mixed with the peptide epitopes.

As these experiments were performed a number of years ago and abandoned in order to pursue other research directions, it would be appropriate to reflect on the results and conclusions with a fresh perspective in order to aid a future student reading this

dissertation for guidance. In retrospect, these studies could have been improved with a number of modifications. Additionally, peptides discussed in the following section could be evaluated with the QCM technique in order to corroborate the results below. Most importantly, the full length sequence of peptide A, in the following section, should be evaluated first with varying amounts of the diluting agent, whether it is tiopronin or a more inert molecule towards PZ. The amount of diluting agent used in these experiments (3:1 molar ratio) was likely too low, not allowing enough space between peptides to avoid steric hindrance to the approach of PZ. Another approach would be to biotinylate the linked terminus of the peptide and conjugate the biotinylated peptide to a layer of streptavidin. The alternative immobilization strategy may allow for more space around each peptide (governed by the surface area and packing density of streptavidin), avoiding the steric problems without the need to vary the quantity of diluting agent. The experiments should be performed at the high ionic strength only, and possibly with the addition of a surfactant such as Tween 20 to cut down on non-specific binding. Low ionic strength binding is near irrelevant in the scope of mimicking a real biological event. The reversible nature of some of the different peptides (2,8, and 10), while interesting, is difficult to fully explain. One possible explanation is that the peptides are in such a conformation as to cast an alpha helical “umbrella” over the tiopronin layer below, which is known to bind to the antibodies discussed, allowing the antibody to reversibly bind the peptide instead of irreversibly and non-specifically sticking to the tiopronin layer. Another important problem with these studies was that the peptides were not amidated and acetylated at the C and N termini, not accurately reflecting the fact that antigenic site A is an internal section of the protein.

Peptide ELISA step-wise linear epitope mapping

Peptides were evaluated in an ELISA assay at various concentrations of peptide, primary antibody (PZ), and labeled secondary antibody and with different wash solutions and development conditions until optimum conditions were obtained for the sequence A.

These optimum conditions were determined to be 50 µg/mL peptide in PBS with 10mM EDTA, 5 µg/mL PZ in wash buffer, goat-anti-human diluted 1:5,000 in wash buffer, and 10 minutes of developing time with TMB substrate followed by quenching with 1N H₂SO₄. The results of this assay are presented in Figure 13.

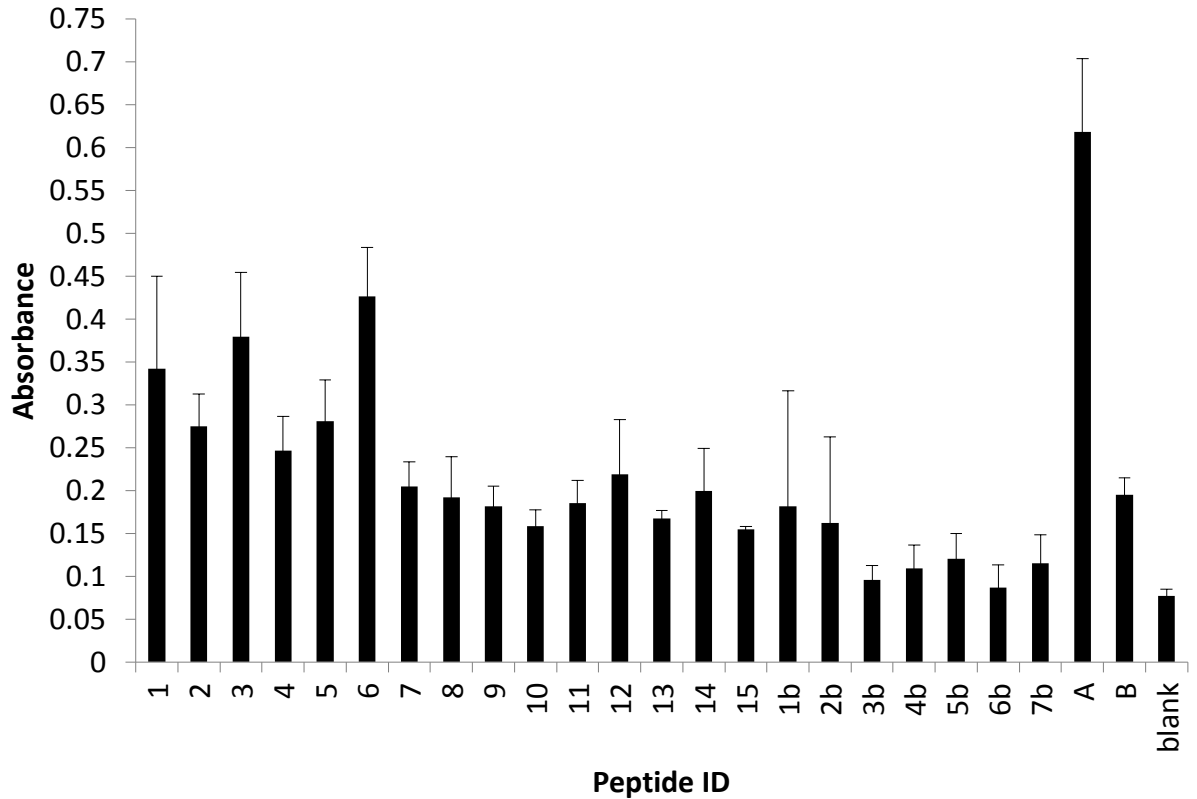


Figure 13: Results of the optimized peptide ELISA. The peptide IDs are listed in Table 4. Multiple null/alternate hypothesis pairs were evaluated from the ELISA data using Student's t-tests at a 95% confidence interval, assuming unequal variances, and a two-tailed distribution. The results are displayed in Table 5. Analysis of the true hypotheses allowed conclusions about which parts of the full peptide sequence A are important to the binding of PZ to HRSV F to be drawn.

Student's t-tests were performed on the data in order help make arguments about which peptides or groups of peptides binds more or less strongly to PZ than others, displayed in Table 5.

Table 5: Student's t-tests for peptide ELISA of whether a given null hypothesis or alternate hypothesis is supported. H_0 is supported if $t_{stat} \leq t_{critical}$ given a two tail distribution at a 95% confidence interval assuming unequal variances. Here x refers to the mean absorbance for the set of peptides indicated by its/their ID #(s) from Table 4. 0 means that H_0 is supported or A means that H_A is suggested to be true with reasonable confidence. H_A is assumed to be the opposite case of H_0 . For instance, for $x_5 \leq x(7-15)$, H_0 means that peptide 5 binds PZ less or equally as efficient as peptides 7 through 15, and A indicates that H_A is supported, which would be taken to be that peptide 5 binds PZ more efficiently than the pooled results of peptides 7 through 15.

H_0	t_{stat}	$t_{critical}$ (two-tail)	supported hypothesis
$x_1 \leq x(7-15)$	2.51	3.18	0
$x_2 \leq x(7-15)$	3.92	2.78	A
$x_3 \leq x(7-15)$	4.46	3.18	A
$x_4 \leq x(7-15)$	2.57	2.78	0
$x_5 \leq x(7-15)$	3.36	3.18	A
$x_6 \leq x(7-15)$	7.19	3.18	A
$x(1-6) \leq x(7-15)$	6.92	2.05	A
$x(7-15) \leq x(b)$	3.78	2.02	A
$x_A \leq x_6$	3.22	2.57	A
$x_A \leq x_B$	8.34	3.18	A

The first significant finding of these tests is that four out of six peptides (2, 3, 5, and 6) are more active towards PZ than peptides oriented in the same direction but missing amino acids earlier in the chain (peptides 7 through 15). Furthermore, the pooled results of peptides 1-6 are significantly more active towards PZ than 7-15. The implication of this hypothesis is that HRSV F amino acids 254-268 represent a “hot spot” for binding of

HRSV F to PZ. The conclusion is reasonable to expect given that there are six hydrogen bond donors (two serine, three asparagine, and one threonine residues) and two negatively charged residues at physiological pH (one each glutamic acid and aspartic acid). There are, however, a higher proportion of these residues in the region represented by peptides 7-15: two positively charged lysine residues, two asparagine residues, and one additional serine residue. Furthermore, escape mutations are present in either region. In the regions represented by peptides 1-6, the following escape mutations have been reported: N262S/Y/K, I266M, and N268I (previously mentioned in Table 1). In the area represented by peptides 7-15, K272N/Q/M/R/E/N/T/D, N276F, and N277Y (previously mentioned in Table 1) have been reported. Peptide A, a representation of the full region, binds PZ stronger than any of the peptide fragments. Joining the regions together gives an estimated, albeit semi-quantitative, increase in affinity of nearly 50% (peptide A versus peptide 6, based on a single concentration of PZ to an identical mass of peptide). The same sequence presented in the reverse direction, peptide B, binds as effectively as sequences from peptides 7-15. Comparing segments from peptides 1-6 and 7-15 to the reversed sequence peptides 1b-7b, and the full length peptide A to B, it is clear that the orientation in which the peptides are displayed to PZ has a dramatic effect on binding affinity.

In conclusion, the most important observations to be made are that the full length epitope with the linker at the C terminus (B) shows little binding activity in ELISA ($A = 0.195 \pm 0.019$), while the full length epitope with the linker at the N terminus (A) shows significant binding (0.618 ± 0.086). The difference in binding was attributed to a

directionally dependent misalignment in the case of peptide B, as demonstrated in Figure 14.

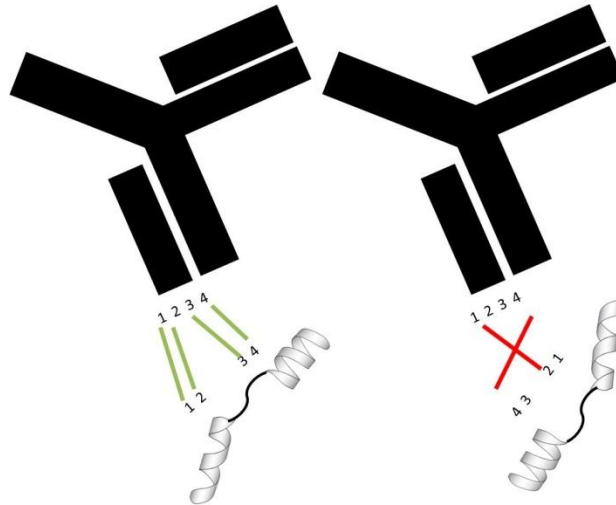


Figure 14: A conceptual interpretation of PZ approaching the synthetic peptide epitope in forward (left) and reverse (right) presentations. The illustrated concept might explain why PZ has such a strong preference for peptide A over peptide B.

Fragments 2,3,5, and 6 are more active than any of the peptides in fragments 7-15, suggesting that the sequence NSELLSLINDMPITN (amino acids 254-268) represents a significant binding motif for mAb interaction with HRSV F, particularly with PZ. The approach of PZ to the protein (or peptide fragment thereof) during recognition is, therefore, hypothesized to occur in a manner where the Fab region of PZ is pointing against the sequence NSELLSLINDMPITN, which constitutes an alpha helical and then kinked part of the native protein. While it was tempting to speculate that the hypothesized approach was due to projection of binding residues further from the surface in fragments 2, 3, 5, and 6, this was not consistent with identical experiments that used

the same primary epitope sequences presented in the reverse direction. As the segments representing amino acids 269-278, which bend opposite from the direction of the earlier part of the sequence in the native protein structure, it was reasonable that presenting them in the same direction eliminated binding.

Given these conclusions, it would be interesting to study peptides 8-15 in reverse.

Alternative presentation might face these sequences in the same direction as they are presented to PZ in the native protein. Studying the two alpha helical portions with the following sequences would be informative: CSGSG-NSELLSLINDM and NDQKKLMSNN-GSGSC. These peptides would allow for interrogation of either alpha helix on its own without the non-interacting loop region (PIT). Chapter III discusses the possibility of placing these sequences together on a single nanoparticle of a specific size to mimic the distance between the two helices in the native protein.

If both halves appear to be distinct “hot spots” that bind the strongest when oriented in opposite direction of each other, this would confirm the importance of the loop conformation of this region in the native protein. In the full length linear sequence, an amorphous loop conformation might be represented by the natural kink introduced by the proline residue at position 265. If this theory is true, the data stands in sharp contrast to the work of Gerdon, et. al.¹¹⁰ In their study of a loop peptide epitope of anthrax protective antigen, they had to use a bidentate attachment strategy in order for their antibody to bind to its nanoparticle immobilized synthetic peptide epitope, purportedly in order to force the peptide into the loop conformation of the native structure. Considering that the peptide used in their study also featured a proline residue in the middle of the

sequence does not necessarily mean that it is kinked into a favorable conformation in the free peptide or in the monodentate immobilized peptide, therefore still requiring the bidentate attachment for antigenic binding. The PZ epitope peptide epitope has two alpha helices, which might help control the conformation without bidentate attachment. The conformation of peptide A is therefore thought to be more identical to the PZ epitope in the native protein than synthetic anthrax PA epitope is to the native epitope. The conformational differences could be confirmed by observing the secondary structure of both peptides in solution, bound to maleimide coated plastic with a single terminal cysteine, and also to a gold surface and analyzing with circular dichroism or solid state NMR.

Alternatively, peptide A has a terminal asparagine residue which is capable of forming either an electrostatic or salt bridging interaction with cysteine carboxylate groups, available from the blocking agent used. Van der Waals bonding of this nature might also act to hold the peptide into a loop conformation more similar to the native structure. Contrary to this theory is the observation that the C-terminal linked peptide B, which also presents a terminal asparagine residue, does not exhibit as much activity towards palivizumab. Notwithstanding, in this form the terminal asparagine may be held at an angle where the steric hindrance to moving the asparagine within close proximity of the blocking cysteine molecules is greater than the steric hindrance encountered in peptide A. Another possibility is that other residues on that terminal would produce repulsive forces against the well-plate surface. Notably, the glutamic acid residue near the N terminal

would electrostatically repel the like-charged carboxylate group. If this model holds true, peptide A might adopt a loop conformation on the well plate whereas peptide B does not.

Since these conclusions were drawn, crystal structures of HRSV F, post-fusion HRSV F, and the motavizumab peptide epitope (identical to the full peptide sequence used in this study) bound to HRSV F have been published. The authors determined that N262, N268, D269, K272, and S275 all have hydrogen bonding or salt bridge interactions with residues in CDRs of both the heavy and light chain of the motavizumab Fab.

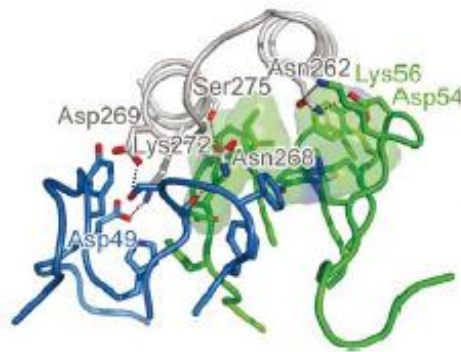


Figure 15: Motavizumab peptide epitope of HRSV F (gray) interacting with the light chain (blue) and heavy chain (green). Labeled amino acids are those participating in hydrogen bonds or salt bridges. From McClellan, et al.⁹⁰ Copyright 2010, Nature Publishing Group, reprinted with permission.

Considering the importance of these residues, it is worth noting that peptide 6 represents the step where N268 is just included along with N262. Unexpectedly, binding is lost upon adding the next important binding residue, D269, in peptide 7, without losing any other important binding residues or escape mutants. At this point along the stepwise path

it is possible that alpha helicity in the early part of the chain is lost with the disappearance of S259, forcing N262 out of a position suitable to bond formation.

The data collected in the peptide ELISA experiments was subsequently used to design antigenic mimics with small gold nanoparticle scaffolds. Chapter III will go on to describe the conjugation of peptides A and 6 to tiopronin protected gold nanoparticles and applying these conjugates in a QCM immunoassay. Furthermore, a loop configuration, with CSGSG linkers on both ends of the sequence, will be evaluated on two sizes of nanoparticle. Additionally, it would be useful to see if the full length peptide maintains the helix-loop-helix structure in solution with the linkers attached, as glycine residues can disrupt helicity. If it does, it would be interesting to see whether certain deletions off of either end disrupt this secondary structure.

Acknowledgements

I would like to begin by thanking Dr. David Wright, Dr. James Crowe, and Dr. David Cliffel for their advice on approaching the epitope mapping experiments on the discontinuous, winding path that it ended up taking. Similarly, I would like to thank Dr. Sam Kuhn and Dr. Chris Keefer for their earlier assistance with this project. Most importantly, I would like to acknowledge my initial training/mentoring from Dr. Aren Gerdon, who carved out much of the early research that led to this study. I would like to acknowledge Malgorzata Broncel, Ryan Rutledge, Holly Carrell, and Joshua Swartz for their aid in peptide synthesis, characterization, and purification. I would also like to

thank Catherine Prudom, Alex Rutledge, and Ryan Rutledge for their help with ELISA assay optimization. Finally, I would like to thank Jay Forsythe, Michal Kliman, Kellen Harkness, and Andrzej Balinski for their help with mass spectrometry.

CHAPTER III

GOLD NANOPARTICLES PRESENTING PEPTIDES AS BIOMIMICS OF HRSV F PROTEIN ANTIGENIC FUNCTION

Introduction

Having a better understanding of the nature of peptide epitopes based on HRSV F antigenic site A, the research went on to employ these materials in combination with tiopronin protected gold nanoparticles, discussed in Chapter I. The research aimed to determine whether or not different peptide epitopes were active (bound by an antibody) on gold nanoparticles, whether the recognition was specific, the effect of simultaneously changing the size of the nanoparticle and identity of an inert spacer between the nanoparticle and peptide, and quantifying the resulting binding interaction for a working “mimic” that was produced. The significance of these results lies in the fact that if an antibody can recognize a nanoparticle, then it is possible that an immune response to the same nanoparticle could result in serum specific to both the nanoparticle and the native protein that inspired it. A nanoparticle conjugate of this design may even be capable of evoking the production of memory cells *in vivo*, validating it as a novel subunit nanovaccine. Additionally, as the peptide and nanoparticle research progressed, a novel immunosensor platform for the diagnosis of HRSV was developed.

As was discussed in Chapter II, some of the early results in this chapter were not informed by information from literature or research presented in Chapter II. However,

the results that are most emphasized and the future directions that are suggested, presented later in this chapter, follow the findings discussed in Chapter II.

Background

Nanoparticles Presenting Peptides as Antigenic Mimics

(Note: much of this background material appears in a previously written review article by this author, Brian Huffman, and David Cliffler, however rewritten and truncated for clarity and a narrowed focus).¹

Given their similar size dimensions to biological macromolecules such as enzymes, receptors, immunoglobulins, antigens, DNA, and carbohydrates, small gold nanoparticles have gathered much interest as biomimetic platforms. These nanomaterials can be surface functionalized during particle assembly with a biomolecule in situ, by direct covalent attachment, or by place-exchange with the biomolecule after particle assembly. In many cases, these conjugate materials have long-term stability. Additionally, nanoparticles can impart conformational structure to a biomolecule, contain a number of different biomolecules within a single supramolecular structure, and are often non-toxic. Furthermore, the methods by which these materials are made provide simpler routes to biofunctionality than classical biological methods such as genetic engineering and directed evolution. Given these fundamental ideas and motivations, the research took from the work of interdisciplinary scientists and proceeded to adapt their concepts to the problem of HRSV, discussed in the previous chapter. It is thought that, ultimately, there

are a number of situations in which nanotechnology will prove more effective than the currently used clinical technology.

A significant body of work exists describing the application of nanomaterials to biological problems. Here, the focus is on a subset of this work that concentrated on using peptides and small metal nanoparticles to mimic the antigenic behavior of whole proteins. An early and straightforward example of this is the synthesis of nanoparticles with a protecting peptide from the histidine-rich protein II (HRP-II) of *Plasmodium falciparum*.¹¹¹ Using standard fmoc procedures, Wright and co-workers recreated this peptide and used it as a stabilizing ligand on different metal core particles: ZnS, Au⁰, Ag⁰, TiO₂, and AgS. These particles were recognized with good specificity by a monoclonal antibody specific for *Plasmodium falciparum*. Their group was able to detect the peptide-encapsulated particles as they would the whole protein with a colorimetric antigen capture assay, showing that their particle mimics the protein-protein interaction of the intact native structure.

Recently, our group has developed several gold nanoparticles that mimic antigens of clinical interest. The first was a glutathione (GSH) passivated gold cluster (GS-MPC) that was then detected with a polyclonal anti-GSH antibody.¹⁰⁵ The antibody very specifically recognized the GSH-MPC compared to a tiopronin protected nanoparticle, even though both surface ligands only differ by, effectively, one amino acid, as seen in Figure 16. While glutathione is not a traditional antigen, it serves as a proof of concept that a very small (< 3 nm) MPC can be functionalized with a surface peptide, and then specifically recognized by a corresponding antibody.

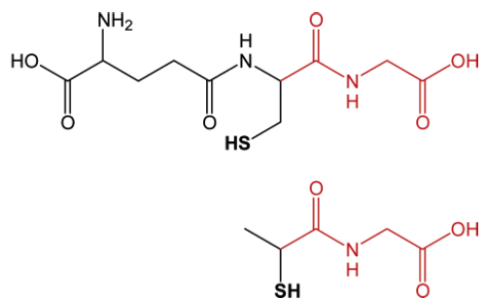


Figure 16: Comparison of the glutathione (top) and tiopronin (bottom) ligands used to functionalize MPCs. Tiopronin is a truncated form of the tripeptide glutathione, with overlap shown in red.¹⁰⁵ Copyright of the American Chemical Society.

Another study from our group focused on a tiopronin gold nanoparticle with a well characterized epitope from the hemagglutinin (HA) protein of influenza.¹¹² The 10-amino acid peptide was synthesized with a terminating cysteine residue to promote place-exchange chemistry. The specific peptide sequence was selected because it is present in a neutralizing site for influenza and there is a commercially available monoclonal antibody specific for this epitope. The same study also compared 2-D SAMs to 3-D nanoparticles, as illustrated in Figure 17. The HA-MPC was more efficient in presenting the peptide to the antibody as it resulted in a higher ratio of antibody to peptide binding when compared to the 2-D surface.

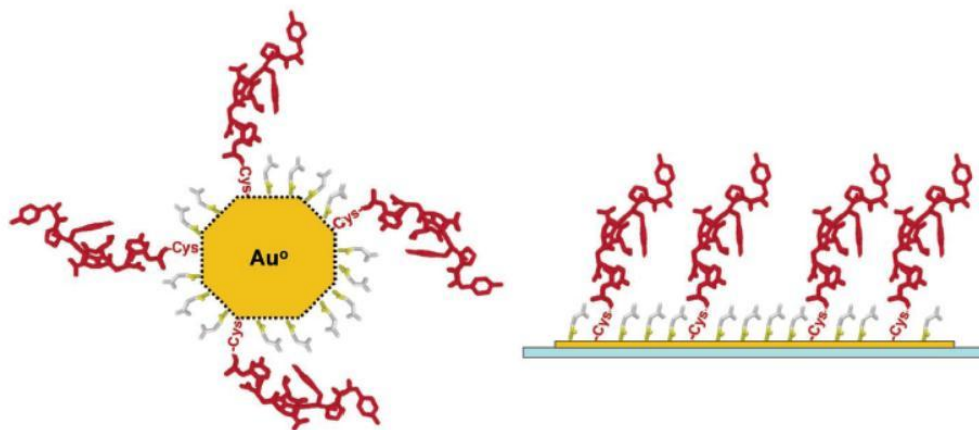


Figure 17: 10-amino acid HA peptide on a 3-D gold tiopronin nanoparticle (at left) and the same 10-amino acid sequence as a 2-D SAM with tiopronin spacers (at right).¹¹² Reprinted with permission. Copyright 2005 of the American Chemical Society, reprinted with permission.

An important aspect of nanoparticles presenting peptide epitopes is whether the nanoparticle bound peptide conformation reflects that of the peptide in the native antigen. Specifically, in our research group, Gerdon and coworkers studied the protective antigen (PA) of *B. anthracis*¹¹⁰, which is one of three precursors of the anthrax toxin. PA was selected for because it precedes the other two proteins (edema factor and lethal factor) in their transport for infection, which makes it an ideal target for neutralizing antibodies. Specifically, the C-terminus and two internal loops of the PA protein were identified as cell-receptor sites, making them ideal candidates for the study. As in previous studies in our group, tiopronin MPCs were place-exchanged with three relevant peptides from the regions on PA mentioned previously. As two of the three PA epitopes selected were loop regions, corresponding peptides were designed so that they could mimic the epitope's native conformation by integrating cysteine residues on both the N and C-terminus.

Cysteine residues at both termini allowed for bidentate attachment across the nanoparticle surface to reconstruct the natural loop. Previous work by Murray and coworkers had reported that ligands attached to the surface will migrate across the MPC to find the most stable conformation possible, as they are in a dynamic equilibrium with the solution phase.^{33, 58, 113} Migration of peptides at a nanoparticle surface suggested that the bidentate peptide was capable of “walking” itself into a conformation similar to the native antigen. Other nanoparticles were synthesized using the same peptide, except with a single cysteine residue on the C-terminus for monodentate attachment, allowing for comparison with the bidentate peptide nanoparticle. Figure 18 illustrates the bidentate versus the monodentate attachment strategy.

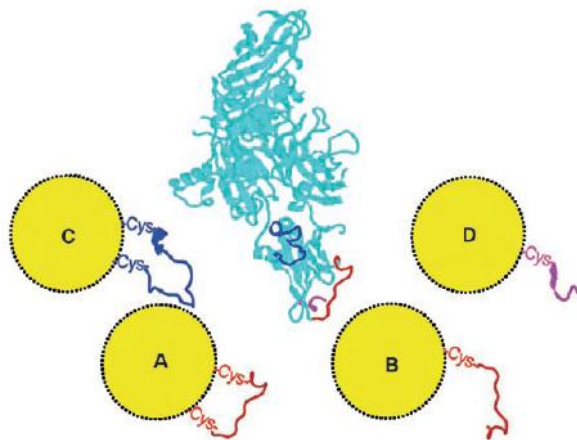


Figure 18: Loop presenting MPCs (left) shown compared to the native protein (middle) and the linear presenting MPCs (right).¹¹⁰ Reprinted with permission of John Wiley & Sons, Inc.

Nanoparticle peptide conjugates were analyzed using a quartz crystal microbalance platform. The results from this study were that the loop-presenting (bidentate peptide)

nanoparticle was strongly recognized by one of seven commercially available monoclonal antibodies, while the linear epitope nanoparticle was recognized only weakly. The loop epitope had a higher affinity (K_a) for this particular antibody than the linear epitope, especially at physiological pH and ionic strength, confirming that the loop-presenting nanoparticle was more readily recognized by the antibody. Preferential recognition of the loop epitope suggests that the commercial antibody has a more structurally constrained paratope, or that the loop presented less steric interference between the antibody and the critical binding residues.

Given their high density of functional groups, peptides are not limited to use as only a biological recognition agent. For example, Naik and co-workers used multifunctional peptides as both the reducing agent, gold-protecting ligand, and presented epitope.¹¹⁴ Peptide A3 was selected from a phage display library and found to both bind to gold and reduce it. Flg, a peptide commonly used in tagging proteins with a biomolecular recognition domain, was also found to reduce gold. Resulting Flg-A3 and A3-Flg conjugated gold nanoparticles prepared in a one pot synthesis were capable of binding to anti-Flg IgG on glass slides.

As previously mentioned, nanoparticles are useful scaffolds for holding multiple molecules into one supramolecular structure. As an extension of peptide epitope protected gold MPCs, in collaboration with the research group of David Wright, tiopronin MPCs containing, in their monolayer, flag epitope (flag-MPC), HA epitope (HA-MPC), flag and HA epitope (flag/HA-MPC), or no epitope were synthesized.¹¹⁵ The peptide epitopes were attached to the cluster via a cysteine terminated polyethylene glycol

hexamer, via place exchange, to provide enhanced accessibility. QCM immunosensors, as previously described, using either anti-flag or anti-HA IgG were used to evaluate the immunological activity of the mimics synthesized. Detection of the HA-MPC and flag/HA-MPC using the anti-HA immunosensor, and the flag-MPC and HA/flag-MPC using the anti-flag immunosensor was subsequently accomplished. Neither one detected the tiopronin MPCs without peptide epitopes. In all these trials, biological recognition serves as a quick means to identify useful peptide nanoparticles and to determine binding constants.

More recently, Mancin and coworkers described a variety of metal cores coated with a helical 11 amino acid peptide.¹¹⁶ H-Ala₃-(Aib-Ala)₄-OMe, where Aib is α -aminoisobutyric acid, was grafted onto a variety of metal cores (with tritylmercaptopropionic acid) and onto silica nanoparticles. The specific primary sequence has been known for holding an α -helical structure in a variety of media. In Mancin's experiments, the peptide held the helical structure after grafting onto all of the tested nanoparticles, as was confirmed by circular dichroism. For the metal nanoparticles, the peptide was used as the primary protecting ligand during reduction with sodium borohydride. These nanoparticles were recognized effectively by immune cells, according to observations with confocal microscopy. These peptide conjugated nanoparticles, and control nanoparticles with a non-helical pentapeptide were taken up equally as well by macrophages. When tested with monocytes, the undecapeptide outperformed its uncoiled counterpart by a factor of two or three in terms of amount of

material taken up in cells. The conducted experiments are an interesting example of how these conjugates can be employed in living systems.

The research group of David Cliffler is currently engaged in adapting nanoparticle mimics *in vivo*. Particularly, much of the research focuses on toxicity and antigenicity. Simpson and coworkers showed that while gold-tiopronin nanoparticles are toxic in mice, the addition of a small amount of tetraethylene glycol into the nanoparticle monolayer eliminates this toxicity.¹¹⁷ Antigenicity is currently being investigated, and there has yet to be a published study showing the generation of native antigen specific sera production in mice after challenge with a peptide-nanoparticle conjugate.

The current investigation utilizes water soluble tiopronin nanoparticles, bidentate and monodentate place exchange strategies with peptides, QCM immunosensing, and information gathered from epitope mapping (discussed in the previous chapter). The resulting data supports the synthesized nanomaterial as a further example of how straightforward methods can be used to mimic the effects of complex biological agents.

Quartz Crystal Microbalance Immunosensing

The QCM instrument has been described previously in Chapter II. A useful review on piezoelectrics in analytical life sciences, written by Janshoff and coworkers,⁹⁴ describes piezoelectric immunosensors, such as the QCM, and their advantages and disadvantages. Summarily, the QCM is a scaled down version of the SPR in terms of analytical capability in biosensing, with somewhat lower sensitivity, and more medium-related

complications (signals affected by solution conductivity, viscosity, non-rigid interactions, etc.). Ultimately, it is still a sensitive, label-free technique that has been well-established for the detection of antigens. The strategies described have been useful to our research group in a number of other disease detection studies¹¹⁸⁻¹²⁰ and in the validation of antigenic nanoparticle mimics.^{92, 105, 110, 112} Adapting some of these strategies, the construction of a QCM immunosensor platform for HRSV detection, centered on the commercial IgG Palivizumab(PZ), was undertaken. This work was extended to validate a gold nanoparticle antigenic mimic of HRSV F protein.

Methods

Materials

$\text{HAuCl}_4 \cdot 3\text{H}_2\text{O}$ was synthesized according to standard methods from electrochemically purified Canadian gold maple leaf coins (99.99%).¹²¹ Reagent and optima grade solvents, N-2-mercaptopropionylglycine (tiopronin), bovine serum albumin (fraction V, 96%), sodium borohydride, thioanisole, and anisole were purchased from Sigma-Aldrich. Common laboratory salts and concentrated ammonium hydroxide were reagent grade and purchased from Fisher scientific. Concentrated sulfuric acid was purchased from EMD. Absolute ethanol was purchased from Pharmco-AAPER. Hydrogen peroxide (30% v/v) was purchased from Acros. Peptide synthesis materials (f-moc protected and side-chain protected amino acids, coupling reagents, and resins) were provided generously by the David Wright research group. 18 M Ω Water was obtained from a U.S.

Filter Modulab water system with a 0.2 μm external filter, or from a Barnstead NANOpure Diamond water purification system. Dry nitrogen is provided in house. Monoclonal antibody 1214, 1129, Palivizumab, and human respiratory syncytial virus were provided generously by the Dr. James Crowe, Jr. research group. Work areas that contained HRSV were cleaned thoroughly with 70% isopropyl alcohol solution. Amicon Ultra molecular weight cut-off centrifuge tubes were obtained from the molecular biology core at Vanderbilt University. Snakeskin pleated dialysis tubing (10,000 MWCO) was purchased from Thermo Scientific. Deuterated solvents (99.9% D) were purchased from Cambridge Isotope Laboratories.

Peptide Synthesis

Peptides were synthesized as discussed in Chapter III. Some peptides were purified by size exclusion chromatography instead of semi-prep HPLC. Peptides used in this study are displayed in Table 6.

Table 6. Peptides that were conjugated to nanoparticles in this study. Series represents the set of experiments in which they were used. Each series evolved based on the results of the last series, as discussed later. The ID will be used to refer to peptides later in shorthand (*e.g.* peptide 2-L represents the peptide with ID “L” from series 2). N-terminus describes whether or not the N terminus was acetylated (AcNH is acetylated and NH₂ is not acetylated), if a cysteine residue (C) was added here for place exchange, or whether serine-glycine-serine-glycine (SGSG) or hexaethylene glycol (PEG₆) spacer was incorporated. Primary epitope sequence indicates the amino acid sequence that was adapted from HRSV F antigenic site A. C-terminus indicates whether or not the C-terminus was amidated (CONH₂ is amidated and COOH is not), whether a cysteine residue was incorporated, and if a spacer was used. Projection follows from the location of the cysteine residue, indicating whether the peptide is immobilized by monodentate attachment at the N-terminus thus projecting the C-terminus away from the nanoparticle surface (N to C) or vice versa (C to N), or whether it is immobilized by bidentate attachment at both termini (looped).

Series	ID	N terminus	Primary Epitope Sequence	C terminus	Projection
1	F	H ₂ N-C	LSLINDMPITNDQKKLMSNNVQ	COOH	N to C
1	L	H ₂ N-C	LSLINDMPITNDQKKLMSNNVQ	C-COOH	looped
2	F	AcNH-PEG ₆ C	NSELLSLINDMPITNDQKKLMSNN	CONH ₂	N to C
2	R	AcNH	NSELLSLINDMPITNDQKKLMSNN	PEG ₆ C-CONH ₂	C to N
2	L	AcNH-PEG ₆ C	NSELLSLINDMPITNDQKKLMSNN	PEG ₆ C-CONH ₂	looped
3	F	AcNH-CSGSG	NSELLSLINDMPITNDQKKLMSNN	CONH ₂	N to C
3	L	AcNH-CSGSG	NSELLSLINDMPITNDQKKLMSNN	GSGSC-CONH ₂	looped
3	F	AcNH-CSGSG	SLINDMPITN	CONH ₂	N to C

Synthesis of Au₂₁₆Tiopronin₁₂₉ Nanoparticles

Tiopronin MPCs were synthesized as previously described.¹²² 5.25 g (15.4 mmol)

HAuCl₄ · 3H₂O was dissolved in 500 mL 6:1 methanol:acetic acid and chilled in an ice bath for 30 minutes, giving a yellow solution. 7.56 g (46.2 mmol) tiopronin was then added to the solution, forming a ruby red intermediate. Upon dissolution of the tiopronin, 5.84 g (154 mmol) sodium borohydride in approximately 10 mL water was immediately

and rapidly added to the mixture. A violent, exothermic reaction results, leaving a black solution. The solution is stirred overnight, yielding polydisperse nanometer sized clusters. The resulting solution is rotary evaporated *in vacuo* to remove the methanol. The resulting precipitate/viscous acetic acid solution is redissolved in water, pH adjusted to 1 with concentrated hydrochloric acid and placed in dialysis tubing (cellulose ester, MWCO = 10 kDa). The dialysis proceeds for 2 weeks changing the water at least twice daily until the water does visually turn a color. ^1H NMR: 4.00 ppm broad singlet (tiopronin methylene on cluster), 3.76 ppm broad singlet (tiopronin CH on cluster), 1.66 ppm very broad singlet (tiopronin methyl on cluster). TEM: average particle diameter of $2.2 \text{ nm} \pm 0.6 \text{ nm}$. UV/Visible spectroscopy: no surface plasmon resonance band observable. TGA: 33 weight percent organic (tiopronin). Average formula: $\text{Au}_{216}\text{Tiopronin}_{129}$.

Synthesis of $\text{Au}_{118}\text{Tiopronin}_{71}$ Nanoparticles

Tiopronin MPCs were synthesized as previously described.¹²² 500 mg $\text{HAuCl}_4 \cdot 3\text{H}_2\text{O}$ was dissolved in 70 mL 6:1 methanol:acetic acid and chilled in an ice bath for 30 minutes, giving a yellow solution. 620 mg tiopronin was then added to the solution, forming a ruby red intermediate. Upon fading of the solution to near colorless, 500 mg sodium borohydride in a minimum of water was immediately and rapidly added to the mixture. A violent and exothermic reaction results, leaving a black suspension. The solution is stirred overnight, yielding polydisperse nanometer sized particles. The

resulting solution is centrifuged, and the solvent decanted. The particles were then resuspended in methanol, and centrifuged a second time. ^1H NMR: 4.00 ppm broad singlet (tiopronin methylene on cluster), 3.76 ppm broad singlet (tiopronin CH on cluster), 1.66 ppm very broad singlet (tiopronin methyl on cluster). TEM: average particle diameter of $1.8 \text{ nm} \pm 0.7 \text{ nm}$. UV/Visible spectroscopy: no surface plasmon resonance band observable. TGA: 33 % by mass organic (tiopronin). Average formula: $\text{Au}_{118}\text{Tiopronin}_{71}$.

Synthesis of $\text{Au}_{696}\text{Tiopronin}_{265}$ Nanoparticles

Tiopronin MPCs were synthesized as previously described.¹²² 500 mg $\text{HAuCl}_4 \cdot 3\text{H}_2\text{O}$ was dissolved in 70 mL 6:1 methanol:acetic acid and chilled in an ice bath for 30 minutes, giving a yellow solution. 110 mg tiopronin was then added to the solution, forming a ruby red intermediate. Upon fading of the solution to near colorless, 500 mg sodium borohydride in a minimum of water was immediately and rapidly added to the mixture. A violent, exothermic reaction results, leaving a black suspension. The solution is stirred overnight, yielding polydisperse nanometer sized particles. The resulting solution is centrifuged, and the solvent decanted. The particles were then resuspended in methanol, and centrifuged a second time. ^1H NMR: 4.00 ppm broad singlet (tiopronin methylene on cluster), 3.76 ppm broad singlet (tiopronin CH on cluster), 1.66 ppm very broad singlet (tiopronin methyl on cluster). TEM: average particle diameter of $2.9 \text{ nm} \pm$

0.8 nm. UV/Visible spectroscopy: no surface plasmon resonance band observable.

TGA: 24 % by mass organic (tiopronin). Average formula: Au₆₉₆Tiopronin₂₆₅.

Place Exchange to Form Series 3 Peptide-Nanoparticle Conjugates

20 mg of Au₆₉₆Tiopronin₂₆₅ was dissolved in 2 mL water. Then, a 1:10 stoichiometric peptide:tiopronin mass of peptide was dissolved in 3 mL of water. The solutions were mixed together and stirred for 72 hours. The resulting nanoparticle-peptide conjugate solutions were subsequently transferred to 10,000 MWCO centrifuge filters, and centrifuged a total of 10 times. The resulting clean solutions were analyzed by ¹H NMR to determine purity and exchange percentages and by UV-Vis to determine nanoparticle concentrations by Beer's law. Drying of the solution was avoided in order to reduce particle agglomeration. Series 1 and 2 peptides (see Table 6) were place exchanged by similar methods, except that dialysis in 10,000 MWCO membranes was used in place of centrifuge filters, and the use of buffers during place exchange and purification was utilized if there was a solubility or stability problem. Series 1 peptides were exchanged with Au₂₁₆Tiopronin₁₂₉, and series 2 peptides were exchanged with Au₁₁₈Tiopronin₇₁.

QCM Immunosensor Construction and Detection of HRSV

A stable frequency baseline was collected while PBS was pumped through the flow cell with a peristaltic pump. Protein G (200 µg/mL) was pumped through the flow cell until

saturation was reached as indicated by a level frequency reading, at which point the solution was switched back to PBS. In the same manner, BSA (1 mg/mL) was then flowed, followed by Palivizumab (40 µg/mL). HRSV, diluted in PBS from growth medium to the desired concentration, was then flowed for a period of about 10 minutes. All solutions were in PBS and flowed at a rate of 20 µL/min. After HRSV was flowed through the cell, all lines and flow cells were purged with 20% bleach solution to decontaminate.

Adaptation of the QCM Immunosensor to Detect Peptide Presenting Gold Nanoparticles

The above Scheme was followed for sensor construction, except that some concentrations were changed to optimize sensitivity and/or save on material. Protein G was used at 50 µg/mL, BSA at 1mg/mL, and PZ at 10 µg/mL. Detection of the nanoparticle solution was achieved by diluting the water solution in PBS to a minimum of 4:1 to avoid drastic differences in solution conductivity and viscosity, which causes inaccuracies in converting the frequency signal to bound mass. The nanoparticle solution was then flowed through the cell as normal.

Results and Discussion

QCM Immunosensor for HRSV

(Note: In concert with Dr. Yibin Zhang, a QCM based immunosensor for HRSV was developed.¹²³ As the data is largely that of Dr. Zhang's, only the major results that are necessary to the understanding of the peptide presenting gold nanoparticle data that follows are discussed.)

A QCM immunosensor strategy for SARS-associated coronavirus¹²⁴ was adapted to specifically and quantitatively detect HRSV. The platform, depicted in Figure 19, is composed of an Fc binding cell wall protein such as Protein A, G, or L from *Staphylococcus Aureus*, a blocking agent such as bovine serum albumin (BSA), and a polyclonal or monoclonal (mAb) detection antibody.

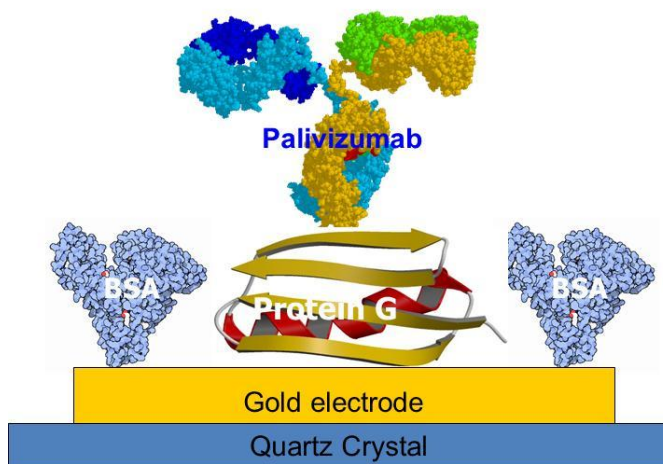


Figure 19: Cartoon schematic of the QCM based immunosensor for HRSV detection. Gold electrodes wrapped about piezoelectric quartz are functionalized with Protein G, which binds PZ in an orientation amenable to HRSV detection. BSA is used to fill in bare gold spaces left after adsorption of Protein G.

Dr. Yibin Zhang was responsible for determining the ideal combination of sensing antibody and Fc binding protein (data not provided here), and determined that the combination of Protein G and Palivizumab optimized the sensitivity and specificity of the instrument towards HRSV. The sensor construction and subsequent detection of HRSV from cultured growth medium diluted in PBS is displayed in Figure 20.

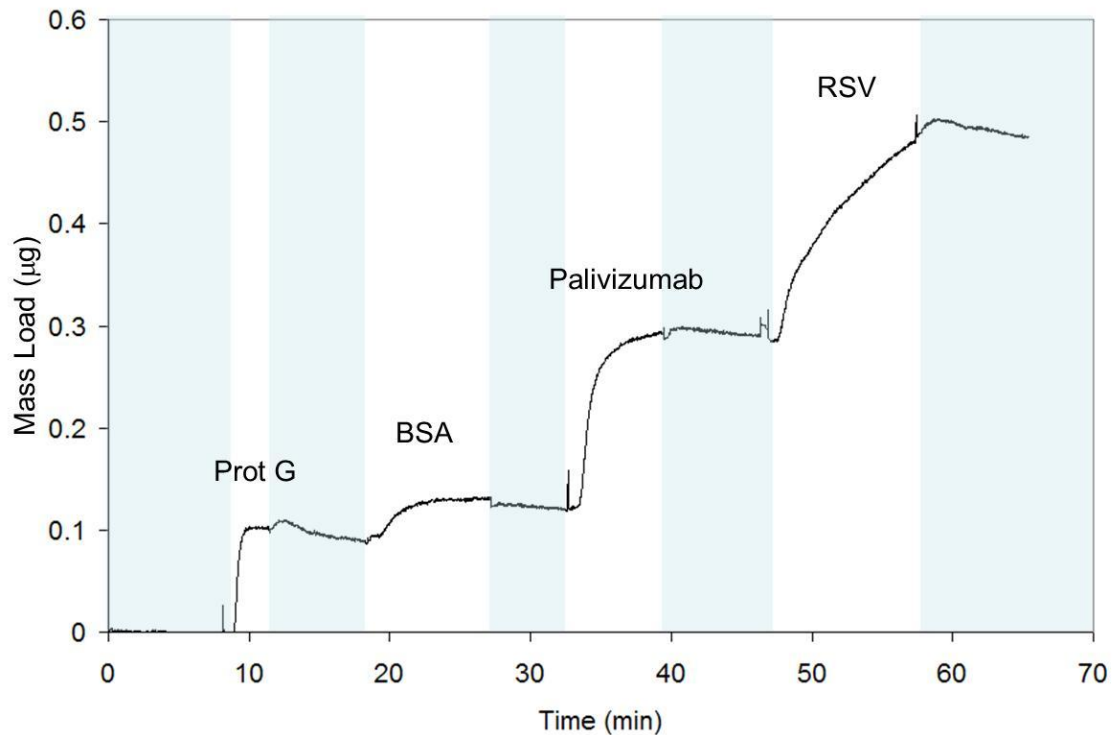


Figure 20: Detection of HRSV with the QCM-PZ immunosensor. Light blue indicates that PBS is being flowed without any analyte. Prot G indicates that 200 µg/mL Protein G is flowed through the cell for the corresponding time duration in white giving a total immobilized protein mass of 99 ng on the gold electrode surface, BSA is 1 mg/mL and gave a mass of 35 ng, Palivizumab is 40 µg/mL and gave a mass of 229 ng, and RSV is 8×10^5 PFU/mL yielding a detected viral mass of 210 ng. All solutions were in PBS and flowed at a rate of 20 µL/min. Figure designed by Dr. Yibin Zhang.

Experiments to evaluate the specificity of the sensor are displayed in Figure 21. These experiments looked at replacement of the antibody and antigen to investigate non-specific binding, associated with false positives. Anti-HA and anti-PA were compared to PZ for detection of HRSV and HRSV growth medium and human metapneumovirus (HMPV), a close relative of HRSV, were compared to HRSV for detection by PZ. All detection steps were run for 10 minutes.

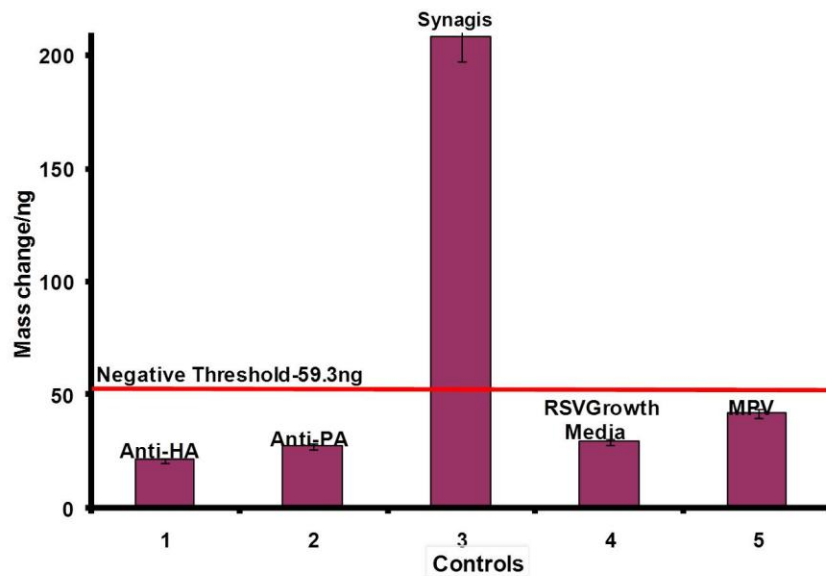


Figure 21: Detection and control experiments for the QCM-PZ immunosensor. Experiments 1 and 2 are sensors detecting HRSV with anti-HA(mouse monoclonal 12CA3 from the Vanderbilt antibody core) and anti-PA (mouse monoclonal anti-PA83 from Alpha Diagnostics) replacing PZ. Experiment 3 is the detection experiment with HRSV and PZ (labeled as Synagis in this figure). Experiments 4 and 5 use the PZ immunosensor, but RSV growth medium and HMPV are substituted for HRSV during the detection step. Figure designed by Dr. Yibin Zhang.

The results from the HRSV growth medium are taken as a negative background because it is present in the positive HRSV sample. A negative background was therefore determined as the signal of HRSV growth medium plus three standard deviations, which is 59.3 ng. Anything below this was determined to be a negative result for detection. Neither of the control antibodies provided significant signal when compared to PZ and to the negative threshold, indicating that HRSV is not electrostatically or physically sticking to other proteins in the sensing layer. Also, none of the other antigens provided a significant signal. The lack of HRSV growth media binding would indicate that the signal is not from contaminants in the HRSV sample that originate from the viral culture. The lack of HMPV binding suggests that the interaction between the Fab region of PZ and the antigenic surface protein of HRSV, in this case F, is of a nature dependent upon the specific primary and secondary structure of the HRSV F protein.

In conclusion, a QCM platform using the combination of protein G and PZ was found to be sufficient for the specific detection and quantitation of HRSV in buffer. The sensor was also found to be capable of detection of HRSV in infected MDCK cells and in human patient nasal wash samples. The sensor had a limit of detection of 9×10^3 PFU/mL.

Development of Peptide Presenting Gold Nanoparticles

Peptides listed in Table 6 were placed exchanged successfully onto tiopronin protected gold nanoparticles. TGA and TEM yielded the number of gold atoms in the nanoparticle core and the number of tiopronin molecules in the unexchanged material, and ^1H NMR yielded the ratio of peptide to tiopronin on the surface, as demonstrated in Figure 21.

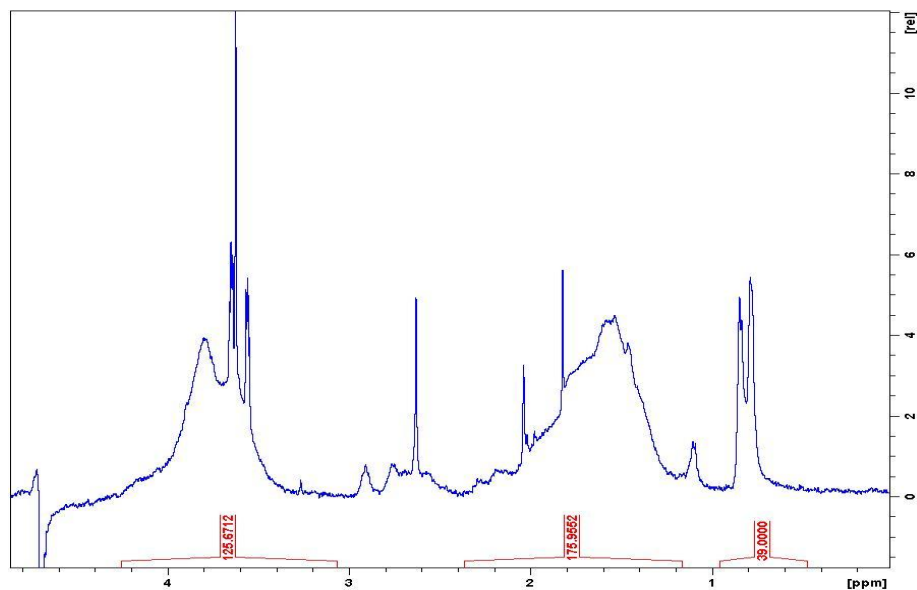


Figure 22: ^1H NMR, with double water-gate solvent suppression, of a peptide-nanoparticle conjugate, in this case $\text{Au}_{696}\text{Tiopronin}_{255}\text{Peptide}(3\text{-F})_{10}$. The extent of peptide exchange is determined by integrating the peak at 0.8 ppm, which represents leucine, isoleucine, and valine methyl protons and comparing that to the peak at 1.5 ppm, which represents tiopronin methyl protons.

Table 7 lists nanoparticle mimics that were synthesized and evaluated with the QCM immunosensor.

Table 7: Nanoparticle mimics studied with the QCM HRSV immunosensor. Peptide IDs refer to Table 3-x. n_{Au} , $n_{\text{tiopronin}}$, and n_{peptide} refer to the number of gold atoms, tiopronin molecules, and peptide molecules per nanoparticle, respectively. d_{TEM} is the diameter of the gold core as determined by TEM. PZ detection qualitatively describes the relative amount and nature of detection.

Peptide ID	n_{Au}	$n_{\text{tiopronin}}$	n_{peptide}	d_{TEM} (nm)	MW (kDa)	PZ detection
3-F	696	261	4	2.7	191	strong
3-L	696	253	6	2.7	198	negligible
3-FS	696	259	6	2.7	187	none
2-F	216	126	3	1.8	72.1	weak, non-specific
2-R	216	127	2	1.8	69.1	none
2-L	216	127	2	1.8	69.6	none
1-F	118	69	2	2.2	40.3	none
1-L	118	67	2	2.2	39.9	none
none	696	265	0	2.7	178.9	none
none	118	71	0	1.8	34.6	negligible, non-specific

Detection of Peptide Presenting Gold Nanoparticles with the QCM Immunosensor for HRSV

As previously summarized in Table 7, many of the nanoparticle mimics evaluated did not interact significantly with PZ. The two notable exceptions were

$\text{Au}_{696}\text{Tiopronin}_{261}\text{Peptide}(3\text{-F})_4$ (mimic A) and $\text{Au}_{118}\text{Tiopronin}_{71}\text{Peptide}(2\text{-F})_3$ (mimic B).

As Mimic B was found to non-specifically bind to the non-sensing proteins on the gold surface (data available upon request), Mimic A will be the focus of the remainder of this chapter. Of importance, one should recall that mimic A was functionalized with the same

peptide that gave the strongest signal in a peptide ELISA assay, as discussed in Chapter II (referred to there as peptide A, and here as peptide 3-F). The primary sequence of this peptide and of peptide 2-F contains the same sequence as peptides studied by MedImmune⁷⁹ and, more recently, by McLellan and coworkers.^{90, 125} The authors were not aware of the latter two works at the time that the following studies were conducted.

Mimic A is of the most interest as it bound strongly and specifically to the QCM HRSV immunosensor. A proof of concept experiment was performed in which a sensor was constructed in the usual way (see methods), except that PZ was left out entirely. In this instance, mimic A was not detected by the sensor. Upon addition of PZ, however, the mimic was detected by its strong binding to the sensor, as shown in Figure 23.

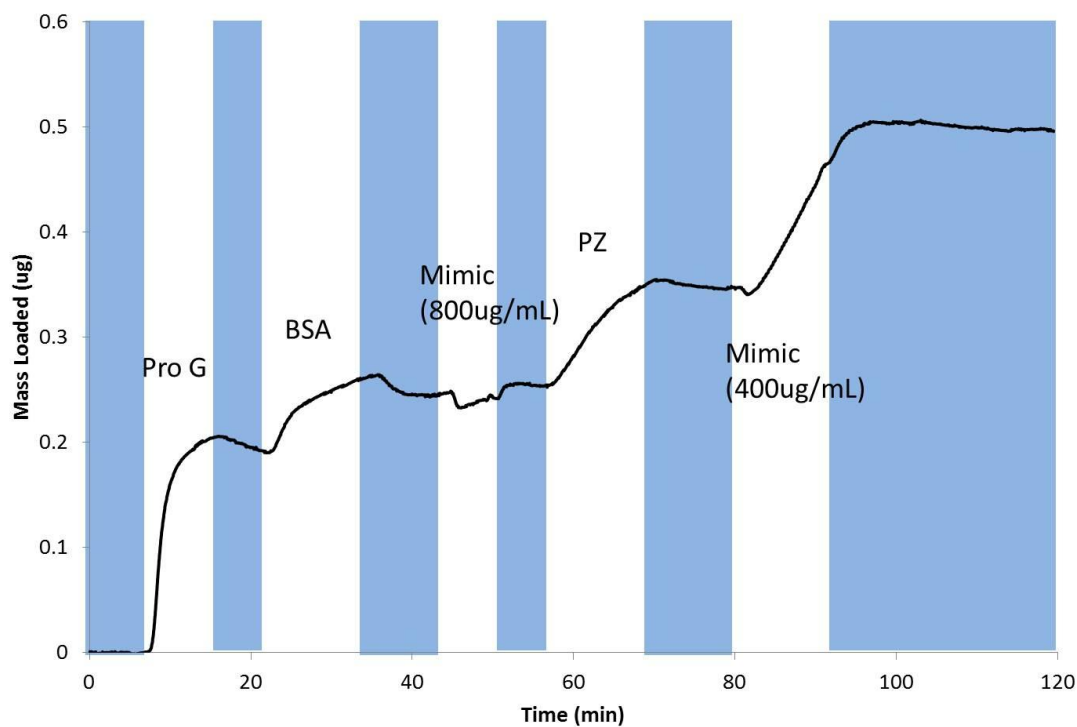
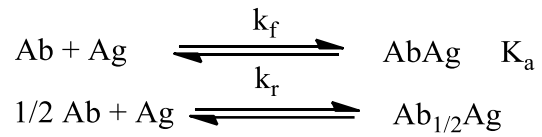


Figure 23: Detection of $\text{Au}_{696}\text{Tiopronin}_{255}\text{Peptide}(3\text{-F})_{10}$ by the QCM immunosensor with and without PZ. Blue sections represent the flow of PBS without analyte. White sections indicate the binding of protein G (50 $\mu\text{g}/\text{mL}$, 192 ng bound), BSA (1 mg/mL, 53 ng bound), nanoparticle mimic (818 $\mu\text{g}/\text{mL}$, no detectable amount of material bound), PZ (10 $\mu\text{g}/\text{mL}$, 92 ng bound), and nanoparticle mimic again (409 $\mu\text{g}/\text{mL}$, 150 ng bound after 15 minutes of flow), respectively.

In order to further characterize the affinity of mimic A for the PZ sensor, a concentration study was undertaken. Six concentrations of mimic A in PBS were evaluated for their bound mass and binding on rate in order to determine k_f , k_r , and K_a for Scheme 3-1.



Scheme 3-1: Langmuirian binding model for an antigen and antibody. The first case is appropriate for large antigens, such as virions, and the second case better describes smaller antigens (peptides, small proteins, nanoparticles).

The data for mimic detection, along with data for the construction of the sensor layer for each experiment is summarized in Table 8.

Table 8: Summary of mimic A detection at various concentrations, along with sensor characterization data for each experiment. n is the number of bound molecules of the corresponding protein. θ is the percent coverage of Protein G by PZ. NP is the mass of mimic A bound after the 3 minutes in the middle of the binding curve. m_{\max} is the theoretical maximum mass of nanoparticle that could bind in either a 1:1, 2:1, or 4:1 model (see Scheme 3-1). None of the sample concentrations analyzed provided an empirical m_{\max} in the time durations allowed, which were limited by the amount of sample available for analysis. * indicates that the data could not be determined due to an instrumental error. Sensor construction data for 818 $\mu\text{g}/\text{mL}$ was lost due to a crash of the data logging program before the detection step.

[Mimic A] ($\mu\text{g}/\text{mL}$)	ProG (ng)	n_G $\times 10^{11}$	BSA (ng)	n_{BSA} $\times 10^{11}$	PZ (ng)	n_{PZ} $\times 10^{11}$	$\theta_{\text{G:PZ}}$	NP _{3m} (ng)	m_{\max} 1:1 (ng)	m_{\max} 2:1 (ng)	m_{\max} 4:1 (ng)
32.7	69	19.2	*	*	45	1.81	9.39%	8.9	61	122	244
32.7	101	28.1	40	3.6	43	1.73	6.13%	9.2	58	116	233
32.7	42	11.7	66	5.95	26	1.04	8.91%	7.1	35	70	141
78.8	145	40.4	65	5.86	108	4.33	10.70%	12	146	292	584
78.8	*	*	*	*	99	3.97	*	20	134	268	536
78.8	106	29.5	53	4.78	98	3.93	13.30%	17	133	265	530
315	69	19.2	*	*	45	1.81	9.39%	35	61	122	244
315	101	28.1	40	3.6	43	1.73	6.13%	43	58	116	233
315	42	11.7	66	5.95	21	0.84	7.20%	23	28	57	114
409	192	53.5	53	4.78	92	3.69	6.90%	42	124	249	498
409	149	41.5	49	4.42	76	3.05	7.34%	43	103	206	411
409	141	39.3	28	2.52	68	2.73	6.94%	43	92	184	368
492	64	17.8	82	7.39	99	3.97	22.30%	81	134	268	536
492	*	*	141	12.7	133	5.34	*	113	180	360	720
818	*	*	*	*	*	*	*	365	*	*	*
818	*	*	*	*	*	*	*	305	*	*	*
818	*	*	*	*	*	*	*	334	*	*	*

Normally, it is straightforward to determine equilibrium association (K_a) and dissociation (K_d) from m vs. C data, but in our case, the inability to determine saturation data renders this method unfeasible. Binding coefficients were instead determined from the maximum on rates at each concentration. Figure 24 illustrates the concentration dependence of the on rate.

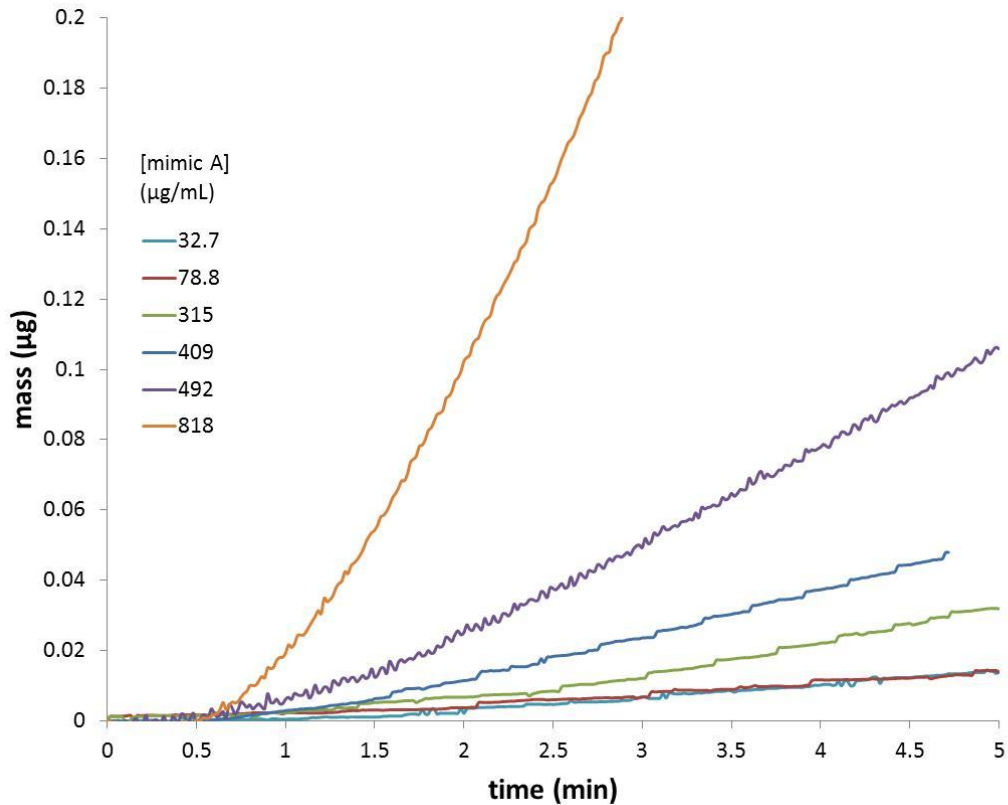


Figure 24: Representative QCM mass versus time curves at various concentrations of mimic A during the detection step.

For any binding model in Scheme 3-1, the kinetics are characterized by:

$$\ln\left(1 - \frac{m_t}{m_{max}}\right) = -(\tau^{-1})t \quad (3-1)$$

where m_t is the bound mass at time t , m_{max} is the maximum mass that can bind to the sensor, the total quantity in the natural logarithm is the uncovered surface percentage and the fractional quantity is the surface coverage percentage at a given time, and τ is the time

constant associated with a given concentration of antigen.^{126, 127} In order to determine m_{max} in the absence of data at saturation, a calculated value is used based on the average number of PZ molecules bound to the sensor. For a 2:1 binding model, which is expected for this system, $m_{max} = 210$ ng. This value of m_{max} provides better fits of data to theory than if individually calculated values for each sensor are used, probably because bound mass is not expected to track linearly with immobilized antibody due to the “hook effect.”^{128, 129} The negative inverse time constant can be determined from the slope of the linear portion of a linear plot of equation 3-1, in the form of the logarithmic quantity versus t , as illustrated in Figure 25 for one of the 409 $\mu\text{g}/\text{mL}$ experiments.

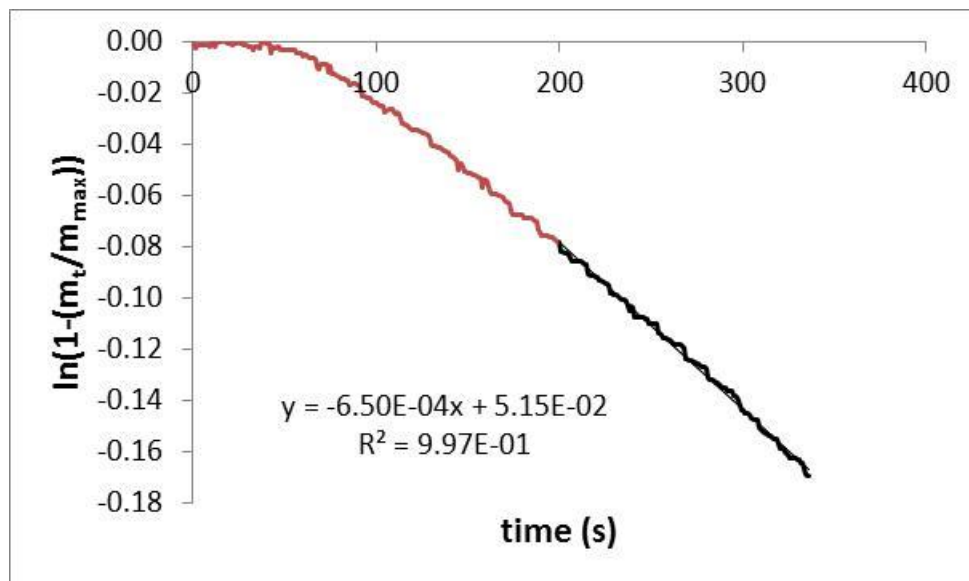


Figure 25: Plot to determine the time constant for mimic A binding to the Palivizumab sensor, τ , for a single experiment. For this 409 $\mu\text{g}/\text{mL}$ experiment, $-\tau^{-1} = -6.50 \times 10^{-4} \text{ s}^{-1}$. The slope is only determined for the linear portion (black), where the binding rate has reached a maximum.

The binding coefficients are determined from the equation:

$$\tau^{-1} = k_f C + k_r \quad (3-2)$$

where C is the bulk concentration of mimic A. A linear plot of τ^{-1} versus C (in mol/L) yields a slope equal to k_f and a y-intercept equal to k_r . For a 2:1 binding model, this looks like Figure 26.

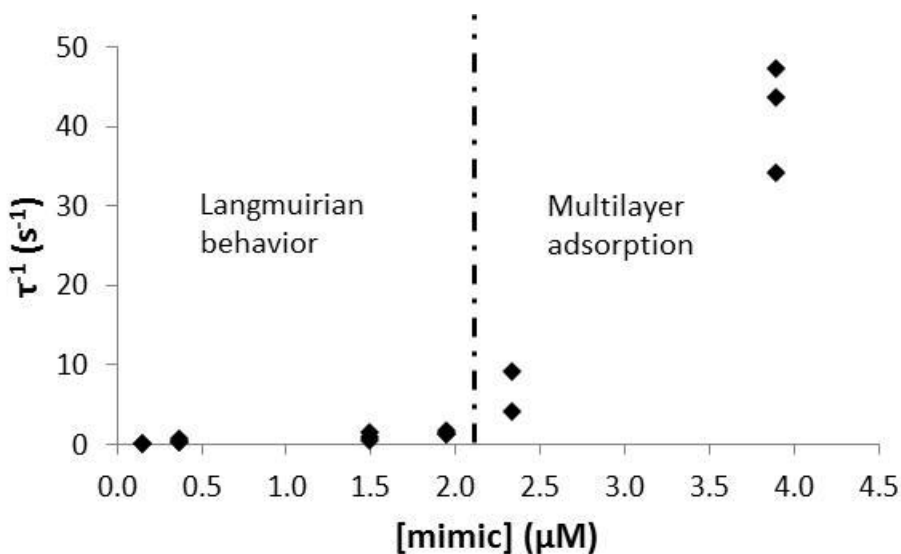


Figure 26. Plot of individual time constants determined for each concentration. Assuming a Langmuir isotherm, a linear plot will give a slope equal to k_f and a y-intercept equal to k_r . Above $\sim 2 \mu\text{M}$, linearity is broken, and the use of those data points to determine binding coefficients is not feasible. The data for the most concentrated sample, $3.90 \mu\text{M}$, is questionable, as it quickly violates the 2:1 binding model (as in Figure 24).

From the data, it appears that the 2:1 Langmuir binding model is not valid for the entire process of mimic interacting with the sensor surface. A plausible explanation is found when the assumptions of the Langmuir isotherm are examined. The model assumes that surface coverage is restricted to a single monolayer and that interactions between adsorbates are negligible and all binding sites are equivalent. The equivalence of binding sites is violated to a certain extent, as there is no unidirectional relationship between the number of PZ molecules and the mass bound to the surface (see Table 8). Deviations were attributed to negative steric effects overtaking positive effects of increasing the total number of binding sites. Steric effects do not, however, explain the data in Figure 26. A more informed explanation was found by breaking the other two assumptions of the Langmuir isotherm. It was, therefore, assumed that the mimics could interact with each other, which would, in turn, lead to multilayer coverage. If true, one would expect that a 2:1 Langmuir model is insufficient. Plausibly, the system follows Langmuirian adsorption up to a certain concentration, which was defined as the point at which linearity is broken. If true, multilayer adsorption is catalyzed by surface immobilization of the first monolayer in a fashion similar to systems that follow a BET isotherm.^{130, 131} This theory also explains the reason why it was difficult to achieve saturation of the sensor (indicated by a plateau in the signal) after a somewhat lengthy period of time and use of a significant amount of material. Examining the four lowest concentrations, the plot in Figure 27 is produced.

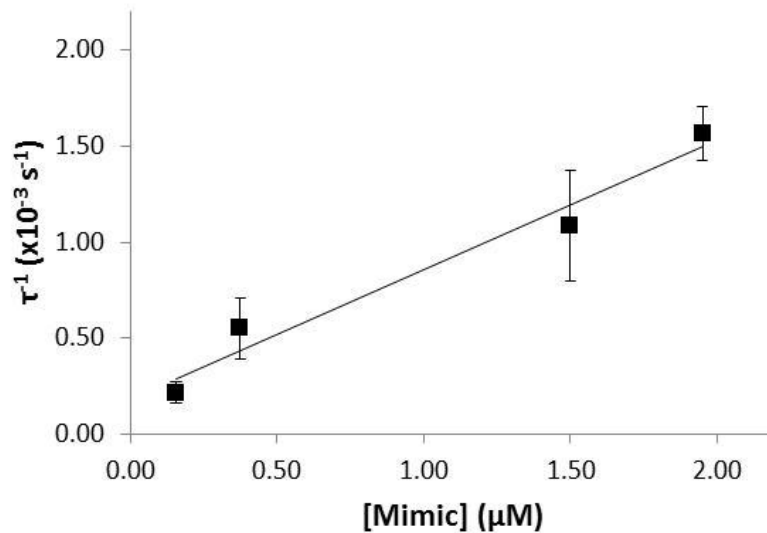


Figure 27: Plot to determine binding coefficients using the four lowest concentration samples.

If the four lowest concentrations are assumed to follow a Langmuirian isotherm, which they appear to, then, for a 2:1 binding model, it is determined that $k_f = 6.74 \times 10^2 \pm 0.88 \times 10^2 \text{ M}^{-1} \text{ s}^{-1}$, $k_r = 1.84 \times 10^{-4} \pm 1.09 \times 10^{-4}$, and, therefore, when one considers that

$$K_a = \frac{[Ab_{1/2}Ag]_s}{[Ab_{1/2}]_s [Ag]_{aq}} = \frac{k_f}{k_r} = \frac{1}{K_d}$$

(3-3)

then $K_a = 3.66 \pm 2.22 \times 10^6 \text{ M}^{-1}$, and $K_d = 292 \pm 177 \text{ nM}$. These values are in the range expected for mAb/antigen interaction. The value of K_d suggests that the affinity of PZ for the mimic is between ~100 and ~300 fold weaker than PZ for the F protein ($K_d = 1.4 \text{ nM}$).⁸⁶ The binding is competitive with that of epitope scaffolds constructed by McLellan and coworkers ($K_d = 87 \text{ to } 3950 \text{ nM}$) with the same primary epitope

sequence.¹²⁵ The advantage of this mimic is that it does not require recombinant genetic techniques to produce; rather, it involves straightforward laboratory techniques and automated peptide synthesis equipment. While nanoparticle and peptide synthesis have their own unique challenges, it is suspected that this is much more straightforward and cost effective on the basis of materials costs and training time of mentored students.

The most significant problem that was encountered with this material was its poor solution stability at ambient conditions. After a few weeks the solutions lost their activity and visible amounts of precipitate could be seen in the stock solution. Observed agglomeration of this nature might be inhibited by refrigeration, freezing, or purging with inert gas. Chemical modification is another option that is worth exploring in the future. Tiopronin carboxylate groups on one nanoparticle can form salt bridges with peptides on another nanoparticle, leading to agglomeration. The effect of salt bridges was suspected on the basis of having worked with similar peptides on tiopronin nanoparticles in the past, and using pH 8.4 borate buffer to avoid precipitation, presumably by deprotonating side chains and allowing for charge shielding. Similar problems with p-mercaptobenzoic acid protected nanoparticles was reported in the literature.²⁹ Borate buffer was not used here because the nanoparticles were initially stable at pH 7. The use of an alternative water solubilizing ligand, such as 1-mercaptotetraethylene glycol,¹³² could solve this problem.

In conclusion, a strong binding HRSV F protein mimic has been synthesized using straightforward and relatively cost effective techniques that can be taught to a novice science student. Mimic A performs nearly as well as the state of the art subunit mimic

($K_d = 87$ nM),¹²⁵ but not as well as the native protein antigen ($K_d = 1.4$ nM), for palivizumab binding.⁸⁶ The performance of this mimic could be improved by optimizing the size of the mimic, experimenting with bidentate attachment on different sizes of nanoparticles, modifying the protecting ligand (1-mercaptotetraethylene glycol),¹³² and optimizing the peptide loading. Given this performance, the mimic should be investigated as a novel subunit vaccine, which is needed in the clinic during the RSV season. This novel material could also be studied as a non-infectious calibration standard for a number of HRSV immunosensors.

The QCM platform that has been developed, while novel and cost-effective, underperforms the SPR in a number of regards. One issue that was not formally raised in the previous discussion is the lack of a stable signal. Often times the signal will drift, and has to be mathematically corrected. Furthermore, it is also problematic that the QCM signal tracks with temperature, which may be the source of the drift.¹³³ Additionally, the difficulty in keeping air bubbles out of the solution leads too often to useless data, increasing the number of experiments to reach a sufficient N value for most studies. The immobilization strategy used is too inconsistent, and is suspected to be responsible for the variance in detection data. That being said, the QCM was effective at detecting the HRSV virion and the nanoparticle mimic with sufficient specificity.

Acknowledgements

I would like to thank Dr. David Wright for the suggestion to use borate buffer for nanoparticle stabilization. I would also like to re-highlight the contributions to this project from Dr. Yibin Zhang. Furthermore, I would like to acknowledge various nanoparticle synthesis advice gathered along the way from Dr. Brian Huffman, Brian Hixson, and Dr. Kellen Harkness. Also, I would like to thank Dr. Brian Huffman, Dr. Leslie Hiatt, and Dr. R. Gerald Keil for their advice on nanoparticles and QCM immunosensing experiments.

CHAPTER IV

SECM OF “WIRED” GOLD NANOPARTICLES TO DETERMINE ELECTRON TRANSFER KINETICS: PROOF OF CONCEPT FOR POTENTIAL COMPONENTS IN NANOMOLECULAR CIRCUITS

Introduction

The current chapter continues with the theme of kinetic studies of gold nanoparticles, but turns the attention from matters of clinical interest to the realm of materials science, as well as moving away from more classical understandings of kinetics to quantum mechanically defined electrons. More specifically, the practical application associated with the experiments that follow lies within the field of molecular electronics, where electron transfer rates are among attributes that define what a given material can and cannot accomplish. The chapter begins with small gold nanoparticles, as in the preceding chapters, but now functionalized with ligands not amenable to aqueous solution. The ligands used are interesting and potentially useful for their electronic properties; straight chain alkanethiols as insulators and a relatively new class of molecule deemed “molecular wires” which are known for their metal-like conductivity or, more accurately, resonant tunneling. The nanoparticles themselves are known for their electronic properties, and therefore, the combination of the two should yield interesting nanomaterials for integration into miniaturized and efficient electronic devices. In the following pages, the electronic properties of these materials and how they fit into the field of molecular electronics, the way in which they can be brought together into a single unit, and characterization of the electronic properties of these nanoparticle conjugates in

solution by the scanning electron microscope are discussed. It was hypothesized that integrating a “molecular wire” into the protecting monolayer of otherwise insulated gold nanoparticles should increase the electron transfer rate, as conductance happens faster, or more often, than tunneling.

Background

Molecular Electronics

In a 2000 editorial in *Nature*, Daniel Feldheim suggested that more research into the effect of structure on electronic properties of nanomaterials in circuits would lead to the discovery of new electronic properties and new applications.¹³⁴ Specifically, he cites applications such as the development of miniaturized devices at a rate that smashes Moore’s law, energy efficient memory storage devices, and extremely sensitive chemical and biological sensors. In the decade that followed, a great number of advances have been made towards these ends, even if molecular and nanoscale electronics are not yet commercially available. These technological advances, along with the excitement surrounding the versatility of gold nanoparticles as previously discussed, motivated the current study which marries the two fields of molecular electronics and nanoparticle science.

The idea of using thiolate protected gold nanoparticles in nanomolecular electronics is not a new one. For instance, in the same year, Schiffrin and coworkers reported on a molecular switch that consisted of a single gold nanoparticle with 60 redox active

bipyridine ligands attached to it and a gold electrode. A schematic of this device is shown in Figure 28.

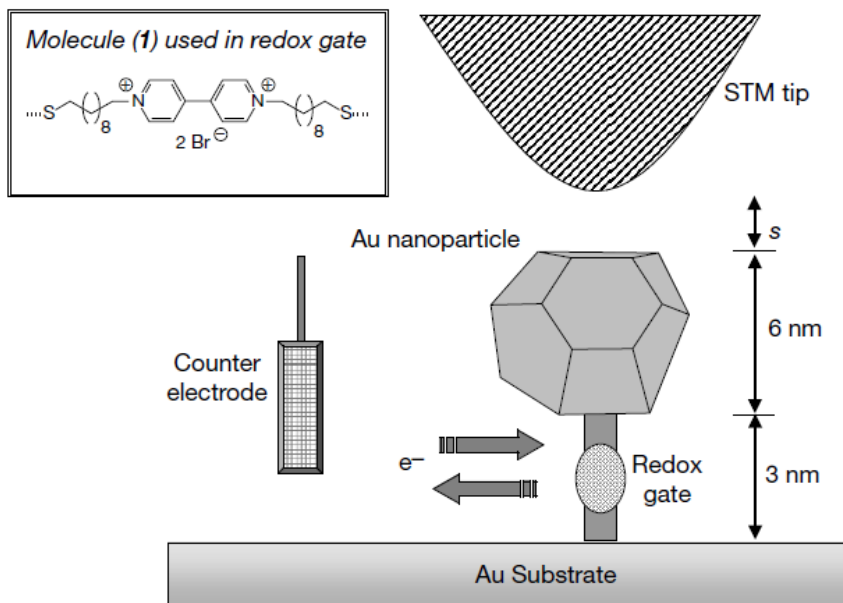


Figure 28: Nanoparticle-bipyridine redox switch.¹³⁵ Copyright 2000, Nature Publishing Group, reused with permission.

Self-assembled dinonanethiol-bipyridine molecules (molecule (1) in Figure 28) on gold attach the nanoparticle to the surface, and their redox state can be tuned by controlling the voltage. An STM tip measures a current-voltage ratio of about 30 nA when the bipyridine is in its reduced state, but decreases markedly when it is in its oxidized state. When the bipyridine ligand is replaced with hexanedithiol, an insulator and non-redox active compound, negligible current is measured at the STM tip. The proposed low voltage molecular switch, similar to a Schmitt trigger, was estimated to require a mere 30 electrons to operate, only 60 redox active molecules, and occupied a volume of about 9 x

9 nm. As Feldheim points out, however, this device could never fill the role of a Schmitt trigger as it operates too slowly and the gain is too low to be considered commercially feasible.¹³⁴ (A Schmitt trigger is a switching circuit that changes an output signal when a positive feedback voltage input signal is sufficiently high.) Instead, he suggested that biosensors are a feasible application area for these types of devices.

Recently, Blum and coworkers showed that nanoparticle-molecular wire networks can be assembled with extraordinary spatial regularity using well defined cowpea mosaic virions (CPMV).¹³⁶ In this study, CPMV is genetically engineered to include cysteine residues at repeated amino acid positions that are fixed by the folding in the virus to well defined spatial coordinates. Addition of 5 nm gold nanoparticles allows for binding at each cysteine residue with 2 and 3 nm gaps between nearest and second nearest neighbor nanoparticles, respectively. The gaps are then filled with 3 nm di-Pt molecular wires and 2 nm OPV molecular wires (defined in Figure 29).

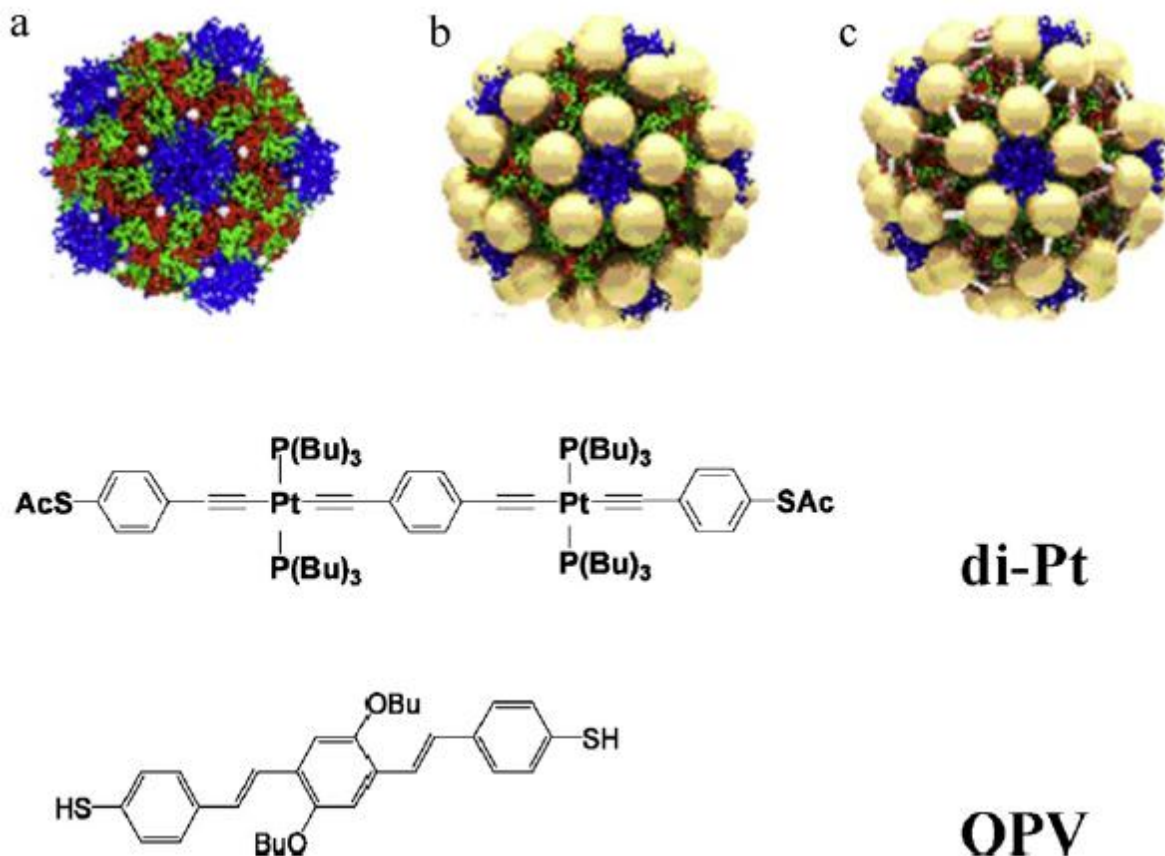


Figure 29: Cowpea mosaic virus-gold nanoparticle-molecular wire conjugate molecular electronic nanosensor. (a) Model of EF-CPMV based on crystallographic data. Cysteine mutation sites shown in white. (b) Model of EF-CPMV with bound 5 nm gold nanoparticles. (c) Model of EF-CPMV showing molecular network of gold nanoparticles with di-Pt (shown in brown) and OPV molecules (shown in white). Conducting molecules used to assemble the nanosensor. di-Pt; 1,4-C₆H₄ [trans-(4-AcSC₆H₄CPt(PBu₃)₂CC)]₂ is 3 nm long, and OPV; oligophenylene-vinylene is 2 nm long.¹³⁶ Copyright 2011, Elsevier, used with permission.

Lysine residues are then biotinylated, resulting in an avidin capturing nanosensor. The sensing is accomplished by measuring current-voltage curves of these nanosensors before and after avidin exposure. The proximity of charges on various avidin proteins changes the conductance of the overall nanoparticle-molecular network in a way that tracks with

the protein charge. The sensors exhibited good specificity when compared to non-biotinylated controls.

Given this background literature in nanomolecular electronics, it would be useful to describe the electronic properties of the separate components discussed in the above devices: gold nanoparticles and molecular wires.

Electrochemical Properties of Gold Nanoparticles

Gold nanoparticles have often been cited for having interesting and useful electrochemical properties. One of the more interesting properties gold nanoparticles possess, in this regard, is their ability to act as a nanoscale capacitor; that is, they are small and soluble like molecules but can undergo a relatively great many redox events within a given voltage window with respect to a small molecule. Using square wave voltammetry, Hicks and coworkers were able to generate voltammograms displaying a great number of charging and discharging events for highly monodisperse hexanethiolate protected gold nanoparticles (AuHexanethiolate).¹³⁷ Figure 30 shows a similar experiment performed in our lab.¹³⁸

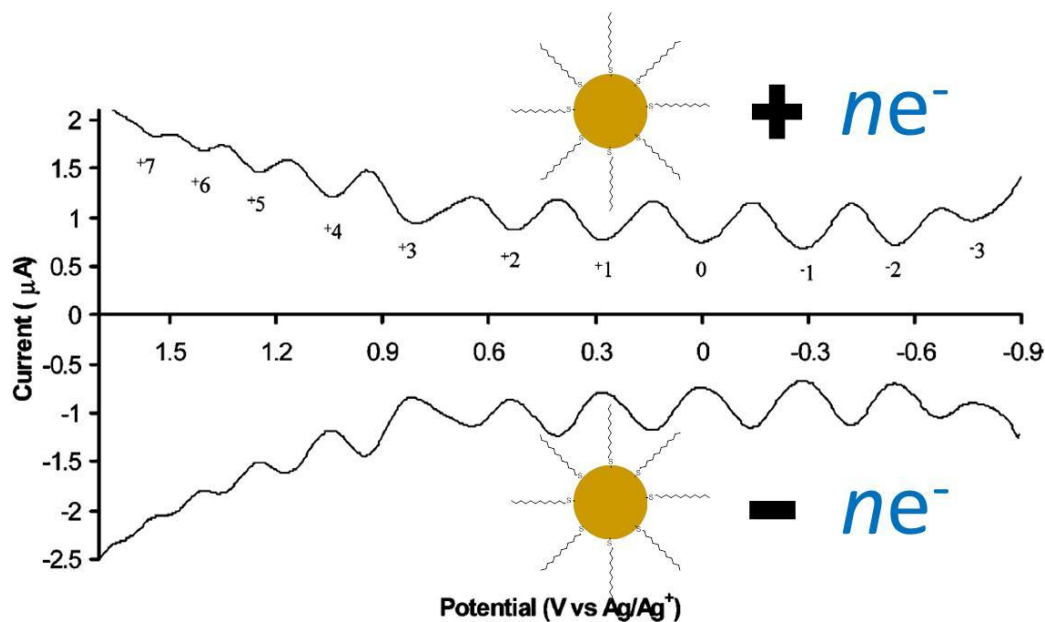


Figure 30: Square wave voltammogram of AuHexanethiolate nanoparticles.¹³⁸ Within the voltage range shown (-0.9V to +1.6V), the nanoparticle stores and reversibly discharges 10 electrons.

These peaks are associated, more specifically, with double layer charging. The capacitance on a single nanoparticle is, therefore, equal to the series capacitance of the stern layer and the diffuse layer. In the case of more polydisperse nanoparticles, the charging behavior still occurs, but the observation of discrete peaks is obscured, as a greater number of redox events are occurring and overlapping in the voltammogram. Therefore, while the behavior is only observed for highly monodisperse nanoparticles, polydisperse nanoparticles should be useful as nanoscale capacitors as well. In order to use this property in a molecular electronics application, it is prudent to assess electron transfer dynamics associated with this charging.

In the solid phase, a number of studies have examined electron transfer with nanoparticles. The Murray group studied the electron self-exchange in deprotonated Au₁₄₀(MUA)₂₀(C6)₃₃/Zn nanoparticle multilayer films on mercaptoundecanoic acid (MUA) self-assembled monolayers (SAMS) on Au disk electrode. Using Cottrell experiments, electron diffusion coefficients in the range of 10⁻⁸ cm/s, electron hopping k values in the range of 10⁶ s⁻¹, and electron self-exchange k values of 10⁸ M⁻¹ s⁻¹ were determined.¹³⁹ Later, the same research group published a study proving that arenethiolate protecting ligands lead to films with faster electron transfer rates and higher conductivities than alkanethiolate ligands.¹⁴⁰ Furthermore, lengthening an alkyl spacer before the aryl group decreased the electron transfer rate. Other groups have investigated gold nanoparticle films with cytochrome C,¹⁴¹ at a mercury junction,¹⁴² on 3-mercaptopropyltrimethoxysilane functionalized glass slides,¹⁴³ and on SAMs of 2-(Dimethylamino)ethanethiol,¹⁴⁴ to highlight some of the many important contributions. The difference between the molecules discussed emphasizes the importance of ligand structure to electron transfer. The importance of the current study, in the scope of the discussed investigations, is the characterization of nanoparticle electron transfer kinetics in the solution phase in order to eliminate effects associated with the solid phase such as packing geometry, interparticle interactions, film thickness, and solid-solid interfaces.

Molecular Wire Molecules

Molecular wires are a class of small molecule that are characterized by delocalized HOMO orbitals, energetically contained within the Fermi level of an attached metal electrode. In the context of a metal-molecule-metal junction, this allows electrons to flow through the molecule in a manner known as “resonant tunneling.” Resonant tunneling is similar in speed to conductance in metals, and certainly faster than through-space tunneling. Resonant tunneling exists in molecules that are rigid, conjugated, and fully coplanar with themselves. These structural properties lead to a high degree of π -conjugation and, therefore, molecular orbitals that extend across the length of the molecule. The concept of a molecular wire is visually illustrated in Figure 31.¹⁴⁵

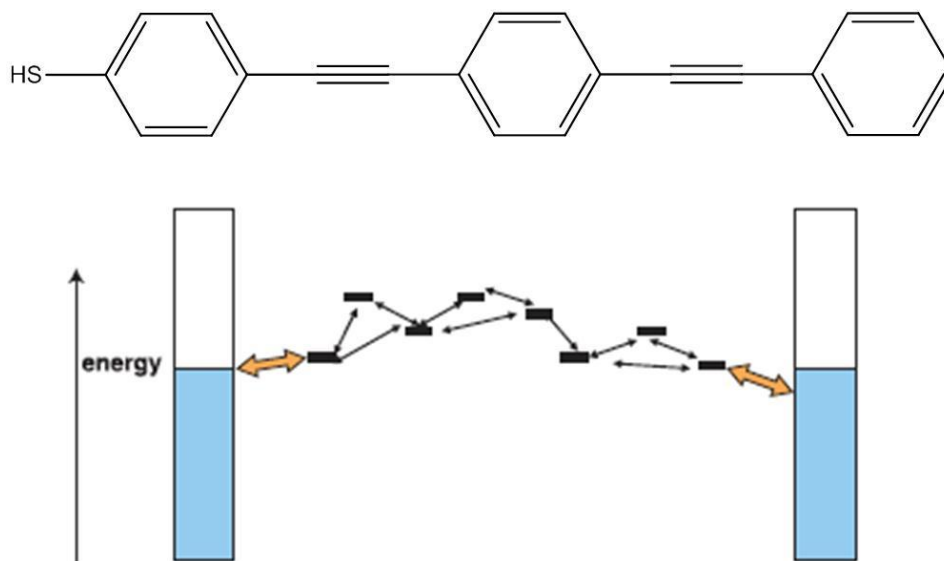


Figure 31: The molecular wire ligand (top, (S-[4-(2-Phenylethynyl)phenyl]ethynylphenyl]thiol, PEPEPSH)) features closely spaced molecular orbitals (bottom) that are energetically within the Fermi level of a metal.¹⁴⁵ Copyright 2003, American Association for the Advancement of Science, reused with permission.

When thought of as a series of within molecule electron transfers, it is also important to note that these molecules tend to have low reorganization energies from a neutral to oxidized or reduced state, corresponding with small changes in bond angles and lengths.¹⁴⁶

Theories on the electronic behavior of molecular wires have been evaluated in a number of studies, usually involving the formation of a metal-molecule-metal junction or junctions. Of note, Ratner and co-workers self-assembled mono- and dithioacetates on the tip of a 10 μm gold wire, and approached it within a small distance of a second gold wire, end to end.¹⁴⁷ The approach of the two wires was controlled by a deflection wire within a magnetic field, bent by a Lorentz force provided by a small DC current. The approach was monitored by measuring current at 0.5 V. Having constructed such an apparatus allowed them to measure current-voltage profiles in a circuit that were dependent on how electrons negotiated the gap between the two wires, which was filled by the SAM molecules. Their experimental setup represents a multi-molecule version of the single molecule junction described previously. Current voltage profiles obtained using SAMs of monothioalkyl (2), dithioalkyl (1), conjugated monothiolalkynylaryl (4), and conjugated dithioalkynylaryl (3) molecules are displayed in Figure 32, along with structures of evaluated molecules (1-4).

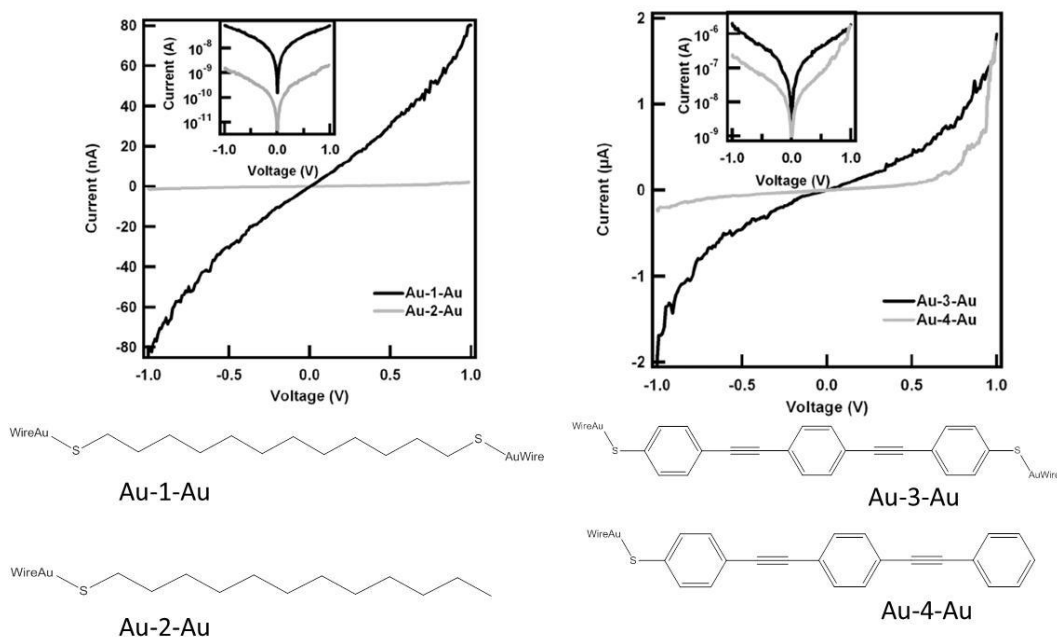


Figure 32: Current-voltage profiles of molecular wires sandwiched between gold wires. Two covalent sulfur-gold contacts shows higher current than single sulfur gold contacts for either case. The conjugated system (3 and 4, at right) shows greater current (μA vs. nA) than the alkane system (1 and 2, at left) (molecular lengths are similar). Copyright 2003, John Wiley and Sons, reused with permission.

Summarily, this study found that having a thiol contact on the other end of the molecule (in addition to the one attached to the gold surface), as in molecules 1 and 3, improved conductivity by at least an order of magnitude over the monothio- molecules 2 and 4. Additionally, the alkynylaryl “molecular wire” molecules, 3 and 4, had conductivities two orders of magnitude higher than the alkyl molecules. This important study highlights the concepts of a molecular wire attached to a classical conductor by use of sulfur “alligator clips” as a viable strategy for nanomolecular electronic device construction.

Tour and coworkers successfully integrated these types of molecules into a functional device.¹⁴⁸ Using gold electrodes sandwiching a molecular wire, they were able to create a binary memory device with write, read, and erase capabilities, as shown in Figure 33.

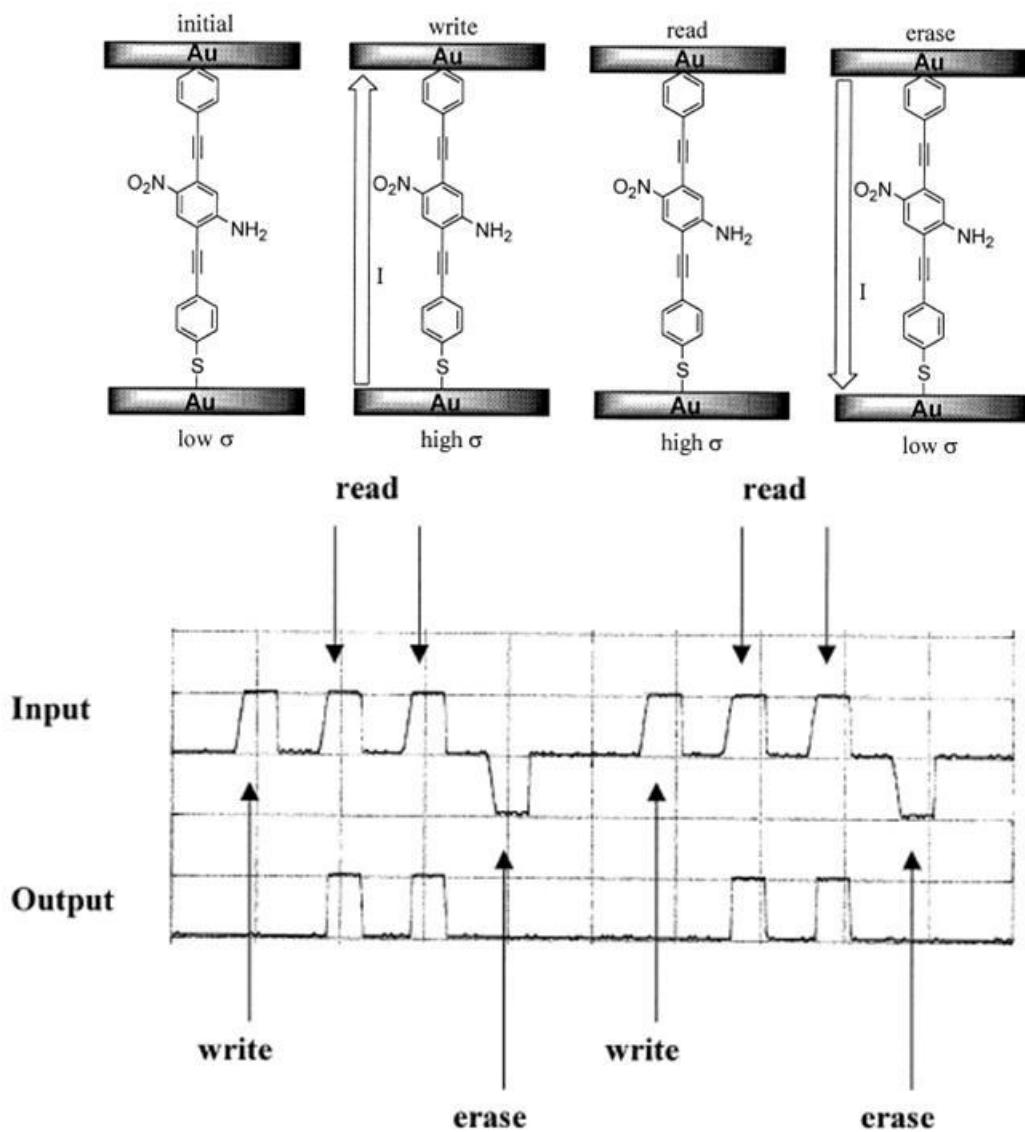


Figure 33: Read-write computing system with gold electrodes sandwiching molecular wires.¹⁴⁸ Writing is accomplished by reductive current, and erasing is accomplished by oxidative current. Copyright 2001, John Wiley and Sons, reused with permission.

Memory, in this case, is in the form of a stored conductance instead of a stored voltage. The increased conductance state that is stored is the result of electron injection into the molecule. The device was designed as a way for their laboratory to test potential molecular wires in a pass/fail evaluation. Interestingly, the device was found to be robust, as no drop off in read signals occurred after an appreciable amount of time, and some devices can last continuously through a year of operation, which correlates with approximately one billion cycles. Aside from its use as a testing, the read/write system was a great proof of concept that small molecule molecular wires can be integrated into a useable device. With this motivation, the research proceeded to adapt molecules of this class to gold nanoparticles with the hope that both components could be integrated into a functional device for a materials or biological application.

Scanning Electrochemical Microscope

Our group developed a method to evaluate electron transfer kinetics in the solution phase by using the scanning electrochemical microscope (SECM). The SECM was first described in 1989 by Bard and Kwak.¹⁴⁹ The instrument consists of an ultramicroelectrode in a glass sheath that comes to a tip, controlled by a piezoelectric motor (or some other motor capable of micron spatial resolution). In feedback mode, it is operated in a solution that contains an electroactive substance, and it registers a normal chronoamperometric response when far away from a given substrate ($i_{t,\infty}$), but it measures a differential feedback current as it approaches. The direction of the current difference

depends on the substrate: positive for a conductive surface and negative for an insulating surface. Alternatively, one can measure redox active species generated at spatially discrete areas of a substrate by using the instrument in substrate generation/tip collection mode. The SECM has found use in a number of studies as an imaging technique in biological and materials applications. In an imaging study, the tip is rastered across a substrate, and differences in current are observed depending on whether it is over an insulator or conductor, or whether it is over an area of the substrate that is generating an electroactive species. Some brief examples should help clarify this concept. Mauzeroll, Bard, and coworkers were able to examine single cell metabolism of the cytotoxic compound menadione in Hep G2 cells (Figure 34a) using the substrate generation/tip collection mode.¹⁵⁰ Wilburn and coworkers were able to image pores formed in lipid bilayer membranes by alamethicin (Figure 34b) using electroactive Ru-hex leakage from below the membrane as an imaging indicator.¹⁵¹ Using feedback mode, Black and coworkers examined libraries of ruthenium-platinum thin films, potential fuel cell anode catalysts, in a 25 x 25 mm array (Figure 34c) with acid as the redox mediator.¹⁵²

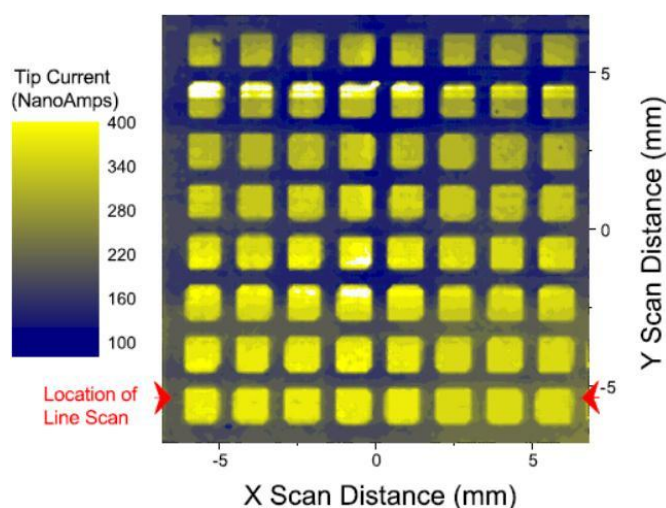
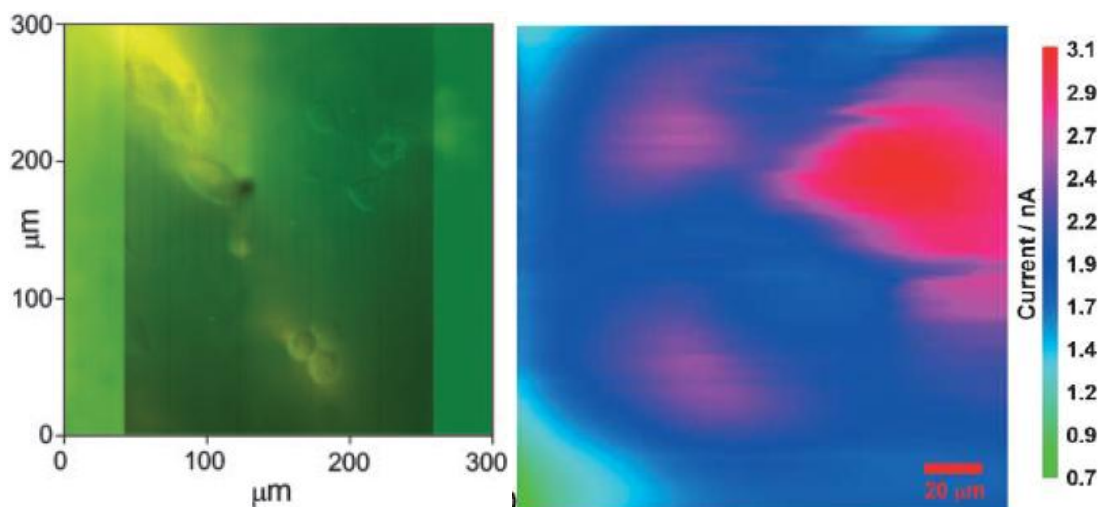


Figure 34: SECM as a useful imaging technique in biological and materials applications. (A) SECM image superimposed on a transparent optical image of Hep G2 cells challenged with menadione. Challenge causes Hep G2 cells to metabolize this compound into the redox active thiodione, which is ejected from the cell by ATP dependent pump (higher current, lighter green area).¹⁴⁰ Copyright 2004, National Academy of Sciences, reused with permission. (B) Alamethicin pore formation in a bilayer lipid membrane allows leakage of redox active Ru-hex, which is detected by the SECM tip.¹⁴¹ Copyright 2006, Royal Society of Chemistry, reused with permission (DOI: 10.1039/B510649D). (C) Combinatorial library of ruthenium-platinum thin films, imaged by SECM, in feedback mode, with H₂SO₄ containing buffer to look for optimal anode catalysts for fuel cells.¹⁴³ Copyright 2005, IOP Publishing, Ltd., reused with permission.

SECM can also be used in the approach mode in order to determine information about the electroactive species in solution, as supposed to using the electroactive species to probe the substrate, as displayed in Figure 35.

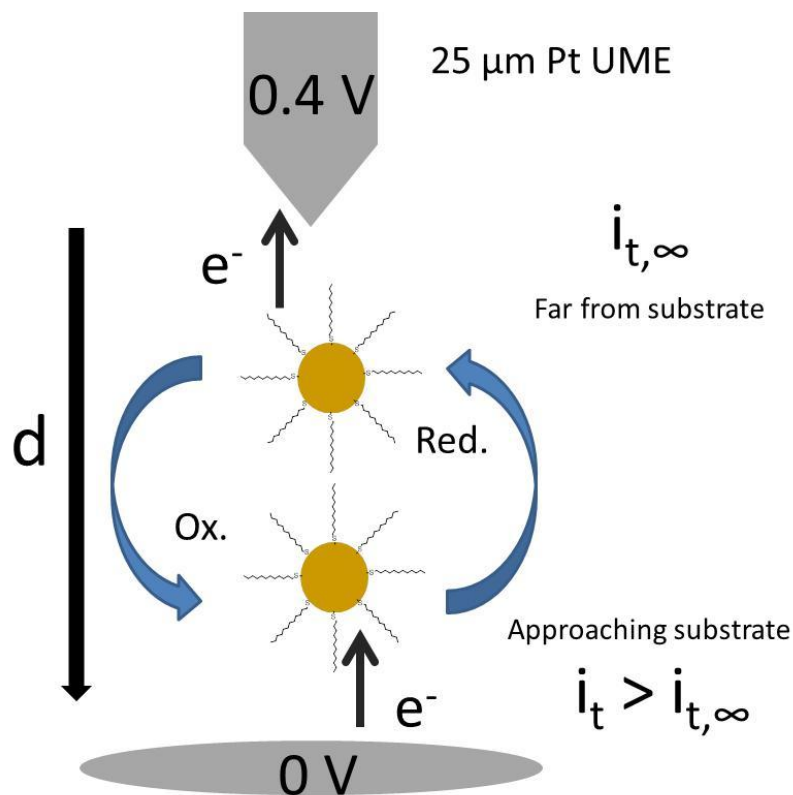


Figure 35: SECM experimental design to measure electron transfer between platinum electrodes and solvated gold nanoparticles. Nanoparticles are initially oxidized at the tip by a cathodic voltage. Diffusion, mainly, carries the oxidized nanoparticles to the substrate electrode, where they are subsequently reduced. The tip current (i_t) increases as the tip approaches (*i.e.* distance, d , decreases) due to a higher local concentration of reduced species as the electrical double layers of both electrodes begin to merge.

Notably, in the scope of this study, Murray and coworkers showed how this technique was capable of measuring electron transfer kinetics between Au_{38} clusters and aqueous redox species at a liquid/liquid interface.¹⁵³

Using similar methodology in a single-phase organic solvent system, our lab was able to show that, for increasing alkanethiol chain length on a gold nanoparticle, the electron transfer rate slows.¹³⁸ Approach curves for increasingly longer alkanethiolate protecting groups are displayed in Figure 36.

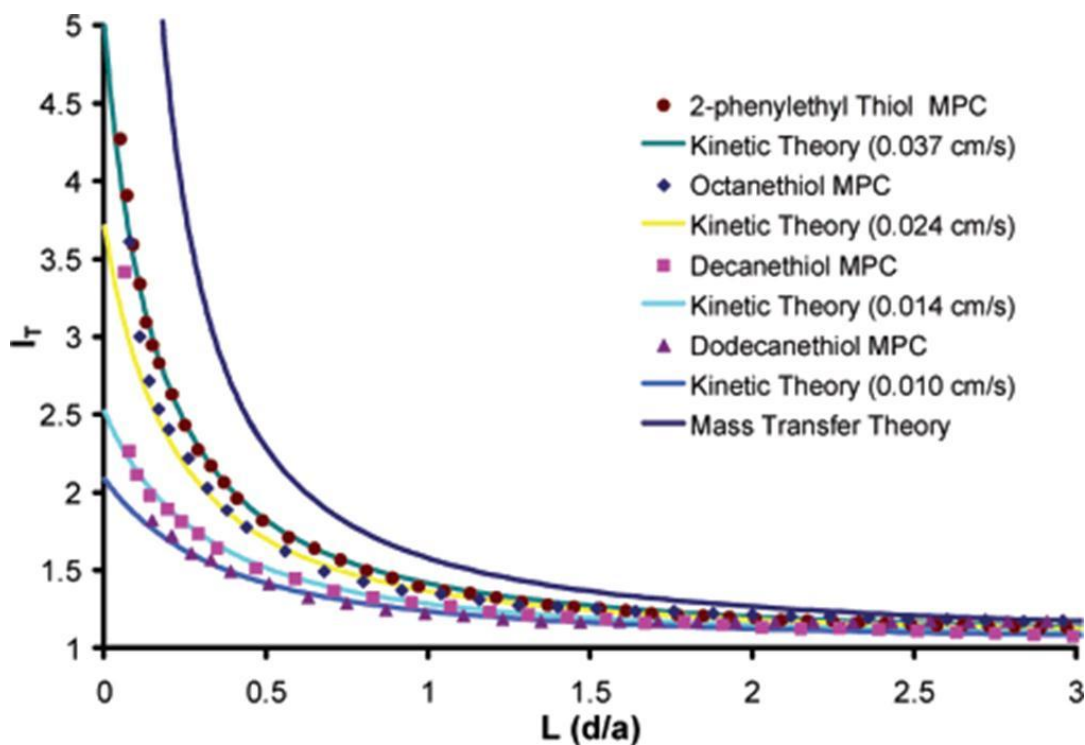


Figure 36: SECM approach curves of AuAlkanethiolate nanoparticles in anhydrous dichloromethane with 1V Pt UME, 0V substrate electrode (vs. Ag/Ag^+). Solutions were 20 mg nanoparticle in 5 mL dichloromethane with 0.1 M TBAPF₆.¹³⁸ The dark blue line for mass transfer theory represents a case where feedback is not limited by diffusion and electron transfer rate, calculated from equation 4-6. Kinetic theory represents curves that are best fit from equation 4-5. Approach curves for nanoparticles fall further off of this line as electron transfer is slowed due to lower tunneling probabilities. Copyright 2006, American Chemical Society, reused with permission.

Peterson reasoned that the electron transfer rate became slower with protecting alkanethiol chain length because the tunneling probability is reduced with greater tunneling distance. This is represented in Figure 36, qualitatively, by the falling off of approach curves from that predicted by mass transfer theory, given by equation 4-5 in the discussion that follows.

The unique attributes of UMEs allow for examination of limiting effects on total current. Quantitatively, the electron transfer rate can be backed out by modeling a best fit to the approach curve. Steady-state current is defined by:

$$i_{t,\infty} = 4nFDC^*a \quad (4-1)$$

where $i_{t,\infty}$ is the steady-state tip current far from the substrate, n is the number of electrons transferred, F is Faraday's constant, D is the diffusion coefficient of the electroactive species, C^* is the bulk concentration of electroactive species, and a is the radius of the disk UME. Mass transfer limited current as the tip approaches the surface is given by:

$$i_{t,M} = nFAm(L)C^* \quad (4-2)$$

where i_t is the tip current while approaching the substrate, and $m(L)$ is the mass transfer coefficient as a function of L , the normalized tip to substrate distance ($L = d/a$, where d is

the raw tip to substrate distance). If current is kinetically limited, and the process is unidirectional at the electrode, which is assumed to be true for a biased electrode, then:

$$i_{t,K} = nFAk_f C^* \quad (4-3)$$

where k_f is the forward electron transfer rate constant. In the case where the current is both kinetically limited and mass transfer limited, it is useful to use:

$$\frac{1}{i_{t,exp}} = \frac{1}{i_{t,M}} + \frac{1}{i_{t,K}} \quad (4-4)$$

where $i_{t,exp}$ is the experimental tip current at a given distance that is limited by both electron transfer kinetics and mass transfer.

The dimensionless normalized tip current is used to evaluate limiting behavior:

$$I_{T,exp}(L) = \frac{i_{t,exp}}{i_{t,\infty}} = \frac{I_T(L) \left(\frac{4D}{\pi a} + k_f \right)}{\frac{4D}{\pi a} I_T(L) + k_f} \quad (4-4)$$

where $I_T(L)$ is a computational fit to a non-limited experimental system,¹⁵⁴ given by:

$$I_T(L) = 0.68 + \left(\frac{0.78377}{L} \right) + 0.3315e^{-1.0672/L} \quad (4-5)$$

In equation 4-5, it is important to note that because $I_T(L)$ is a ratio of currents, n and C cancel out. Equation 4-4 implies that the *shape* of an approach curve is not dependent upon concentration or the number of electrons transferred. Ultimately, the approach curve is only dependent upon the diffusion coefficient, the electron transfer rate constant, and the electrode geometry.

Using this approach, it was hypothesized that integrating a “molecular wire” into the protecting monolayer of alkanethiolate protected gold nanoparticles should increase the electron transfer rate at a biased platinum electrode, as conductance happens faster, or more often, than tunneling, as illustrated in Figure 37.

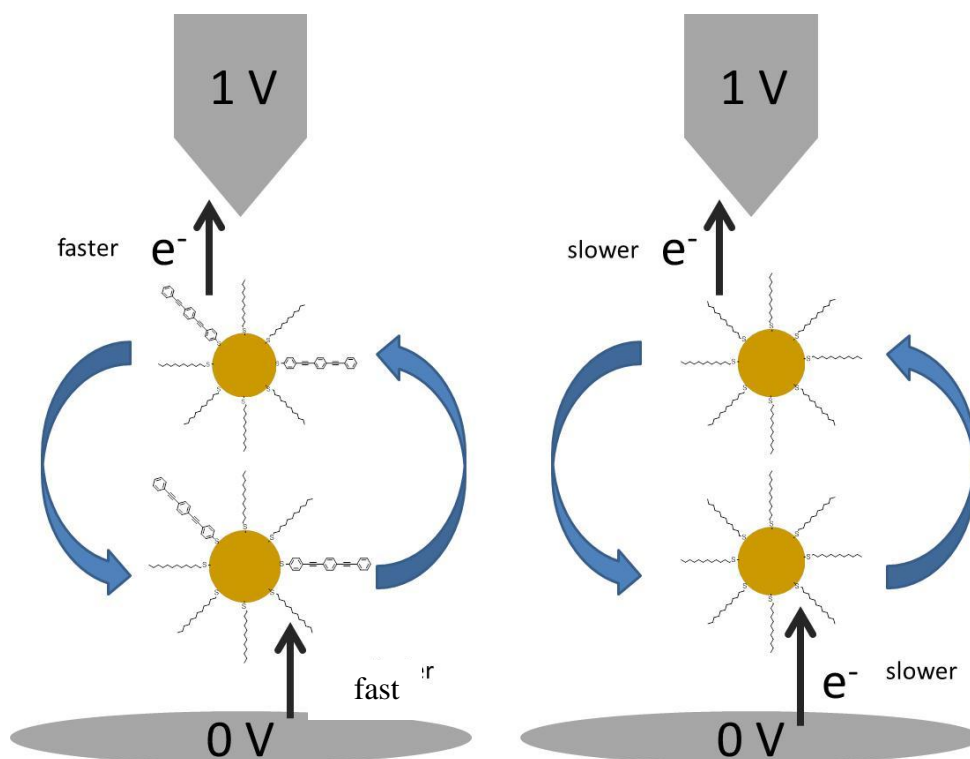


Figure 37: Proof of concept experiments to confirm whether “wired” AuDodecanethiol nanoparticles (left) exhibit faster electron transfer than their “unwired” precursors (right).

Methods

Materials

$\text{HAuCl}_4 \cdot 3\text{H}_2\text{O}$ was prepared as described previously.¹²¹ $\text{HAuCl}_4 \cdot 3\text{H}_2\text{O}$ was synthesized according to standard methods from electrochemically purified Canadian gold maple leaf coins (99.99%).¹²¹ Reagent and optima grade solvents, alkanethiols (90%), sodium borohydride, lithium borohydride, tetrabutylammonium hexafluorophosphate (TBAPF_6) and S-[4-(2-

phenylethynyl]phenyl]ethynylphenyl]thioacetate (PEPEPSAc) were purchased from Sigma-Aldrich. Anhydrous dichloromethane (99%) from Sigma Aldrich was used from a sure-sealed bottle. Common laboratory salts were reagent grade and purchased from Fisher scientific. Concentrated sulfuric acid was purchased from EMD. Absolute ethanol was purchased from Pharmco-AAPER. Hydrogen peroxide (30% v/v) was purchased from Acros. Chemicals for peptide synthesis (f-moc protected and side-chain protected amino acids, coupling reagents, and resins) were provided generously by the David Wright research group. 18 M Ω Water was obtained from a U.S. Filter Modulab water system with a 0.2 μ m external filter, or from a Barnstead NANOpure Diamond water purification system. Electrodes were purchased from CH instruments, or were previously fabricated in this research group and handed down. Diamond paste was purchased from. Alumina was purchased from. Deuterated solvents (99.9% D) were purchased from Cambridge Isotope Laboratories.

Synthesis of Au₁₁₂₀ Dodecanthiolate₆₉₀

1.5 g of tetraoctylammonium bromide (a phase transfer agent) was dissolved in 80 mL of toluene. 0.31 g of H₂AuCl₄ was dissolved in 25 mL of water. To the vigorously stirring tetraoctylammonium bromide solution, the gold solution was added slowly. The resulting orange gold-containing organic phase was isolated and chilled in an ice bath for 30 minutes and stirred vigorously. 0.38 g of NaBH₄ was dissolved in 25 mL of water. To the stirring organic solution, 260 μ L of 1-hexanethiol was added. Immediately, the

NaBH₄ solution was added over a period of 10 seconds. The resulting black solution was stirred for 30 minutes on ice, and then additionally overnight at room temperature. The organic phase was isolated and rotary evaporated to yield a black solid. The solid was dissolved in a minimum of toluene and precipitated in 400 mL of ethanol at -20 °C overnight, which was then decanted and centrifuged. The precipitate was collected on the walls of a round bottom flask by dissolution and rotary evaporation and sonicated in 400 mL of acetonitrile and then ethanol. ¹H NMR: 1.45 ppm, 0.98 ppm broad peaks. TEM: 3.4 ± 1.1 nm. UV/Vis: slight surface plasmon band observed. TGA: 34.5 % organic material.

Synthesis of Au₂₂₈Octanethiol₉₂

HAuCl₄ (300 mg) and 160 mg LiBH₄ were dissolved separately in freshly distilled THF (30 mL total), and then purged with argon. The gold solution was chilled to near 0°C in an ice bath. Then, 1-octanethiol (280 µL) was added via syringe to the gold solution. After a few seconds, the LiBH₄ solution was added dropwise to the mixture. It is important to add the LiBH₄ shortly after addition of the 1-octanethiol, or precipitation of oligomeric precursor material will decrease the yield and increase the polydispersity and size of the nanoparticles. CAUTION: LiBH₄ reacts with gold very exothermically; therefore caution should be observed during addition, and care should be taken to quench and clean the area of any excess LiBH₄ as it tends to float during weighing. The resulting black to brown solution was stirred overnight. To this, 30 mL of water were added, and

this was extracted into 60 mL diethyl ether and washed with brine 3 times. After rotoevaporation of the solvent, the nanoparticles were suspended in acetonitrile, centrifuged, suspended in ethanol, centrifuged, and washed by drying on a round bottom flask and sonicating in a large excess of acetonitrile and/or ethanol until spectroscopically clean. Characterization data: TEM: 2.0 ± 0.8 nm. TGA: 25.0% organic material. UV-Vis: slight SPR band observed at 520 nm. ^1H NMR: 0.98 and 1.50 ppm broad resonances.

Deprotection of S-[4-(2-Phenylethynyl)phenyl]ethynylphenyl]thioacetate (PEPEPSAc)

100 mg of PEPEPSAc was dissolved in 8 mL of dichloromethane and 2 mL of methanol. 4 drops of concentrated sulfuric acid was added to this. The reaction was stirred overnight under a reflux condenser to slow solvent evaporation. The volume was reduced, if necessary, and poured onto a silica gel plug topped with a filter paper. Fractions were collected in increasing gradients of dichloromethane in hexanes. Fractions that yielded a white solid upon evaporation were collected first (in low dichloromethane). Yellow solids were collected in later fractions (increasingly higher dichloromethane). White fraction (S-[4-(2-phenylethynyl)phenyl]ethynylphenyl]thiol, PEPEPSH): ^1H NMR 7.51 ppm, m, 7H (aromatic); 7.38 ppm, m, 6H (aromatic); 3.54 ppm, s, 1H (thiol). First yellow fraction (di-S-[4-(2-Phenylethynyl)phenyl]ethynylphenyl]disulfide, PEPEPS₂): 7.52 ppm, m, 14H (aromatic);

7.36 ppm, m, 12H (aromatic). ^1H NMR were taken on a Bruker AV 400 MHz instrument.

Place exchange reactions with PEPEPSAc and PEPEPS₂

20 mg of Au₁₁₂₀Dodecanthiolate₆₉₀ was dissolved in 4 mL toluene with 8 mg PEPEPSH and stirred for 7 days. The product was dried onto a round bottom flask and sonicated in 100 mL acetonitrile for 20 minutes, 3 times, and with ethanol for 20 minutes, 3 times.

20 mg of Au₂₂₈Octanethiol₉₂ was dissolved in 4 mL toluene with and stirred for 72 hours. These particles were suspended and then centrifuged from acetonitrile and then from ethanol. Further purification was accomplished by drying them in a round bottom flask, and then sonicating in an excess of acetonitrile and then ethanol, once each.

Scanning Electrochemical Microscopy Experiments

Nanoparticle samples were dissolved in anhydrous dichloromethane (20 mg in 5 mL) with 200 mg TBAPF₆. These solutions were pushed through nylon syringe filters (0.45 μm). 2 mm Pt substrate electrode was treated by polishing with successively smaller grit diamond paste, and then finally polished on a polishing wheel (0.1 and 0.05 μm Micropolish II with 8" Microcloth on a Metaserv 2000 Grinder/Polisher (Buehler)). The polished tip was then sonicated in deionized water and then in ethanol. A smooth surface was observed using an Olympus BX4 optical microscope (< 1000x magnification).

Occasionally, it was cleaned by holding in piranha solution for 1 minute. Finally, it was cleaned by constant scanning from -0.4 to 1.4 V (vs. silver wire quasi-reference electrode, with a Pt counter wire) in 0.1 M H₂SO₄ with 0.1 M KCl until a lack of hysteresis in the cyclic voltammogram was observed. The tip was rinsed with water and ethanol. The 25 μm Pt UME was treated similarly. During polishing of the UME, care was taken not to create a tip surface with an RG > 5 (usually around 2-3 in these studies).

Ag/Ag⁺ quasi-reference wire electrode was prepared by applying a potential of 1V across the wire for about 1 minute, resulting in a blackened layer of AgCl. The AgCl layer was lightly scraped with fine grit sand paper to reveal some uncoated surface.

The UME was fitted into the plastic holder of a piezoelectric motor and visually positioned over the center of the Pt substrate electrode, which is fitted into a plastic well with the reference electrode. The well was filled with the nanoparticle solution and approached at a faster rate until an increase in current was observed (UME @ 600 mV, substrate at 0 mV), at which point it was stopped and backed up a minimum 80 μm. Approach curves were collected with the UME at 200-600 mV and the substrate always at 0 mV (vs. Ag/Ag⁺). Dichloromethane was replenished when necessary to a visually identical volume (close to the brim). In between sample changes, the chamber and electrodes were rinsed with anhydrous dichloromethane until the rinsate was not colored.

Nanoparticle Surface Quantitation

For dodecanethiolate nanoparticles, samples were prepared in DCTB matrix in toluene at approximately 400:1 matrix/analyte ratio. All MALDI-IM-MS analyses were performed using a Synapt HDMS (Waters Corp., Manchester, UK), equipped with a frequency-tripled Nd:YAG (355 nm) laser operated at a pulse repetition frequency of 200 Hz. All spectra were acquired in the positive ion mode at laser energy settings approximately 10% above threshold values.

Gold-containing ion signals were extracted and identified using the MassLynx 4.1 (Waters Corp.) software package. Processed spectra were exported to Microsoft Excel, in which a custom spreadsheet was constructed for the remainder of the data processing. three stoichiometries identified previously: $Aux+1Lx$, $AuxLx$, and $AuxLx+1.32$ Within these stoichiometries, an appropriate list of permutations was constructed with every possible combination of ligands and modifications such as sodium coordination and methyl esterification. Protons were added or subtracted as necessary to achieve a +1 charge state. Each processed spectrum was filtered by abundance, with any signal below 1% relative abundance with respect to the base peak discarded to reduce false positive identification. The remaining peaks were compared to the expected gold-thiolate ion list. Any observed peak within 30 ppm mass accuracy of an expected peak was matched and used for quantitation.

For octanethiolate nanoparticle samples, a concentrated solution in $CDCl_3$ was prepared, and standard 1H experiments run on a 500 MHz Bruker NMR, 64+ scans. Non-solvent

residual peaks in the aromatic region were calibrated to 13 for the 13 aromatic protons in PEPEPS, and compared to the combined peaks for the alkane chain, representing 17 protons for octanethiol. The stoichiometric ratio was matched to the original nanoparticle formula to yield an estimation of average nanoparticle composition (semi-quantitative).

Results and Discussion

A Note About Surface Ligand Quantitation

In the research group of David Cliffel, a methodology for ion mobility-MALDI mass spectrometry (IM-MALDI-MS) to quantify the relative composition of the protecting monolayer of gold nanoparticles was developed.⁶⁵ As the technique was new, and the instrument was often used for other applications, it was only applied to a couple of the samples referred to in this chapter, but was proven effective in the analysis of similar samples not discussed here. Example data is shown below in Figure 38 for Au₁₁₂₀Dodecanthiolate₆₉₀.

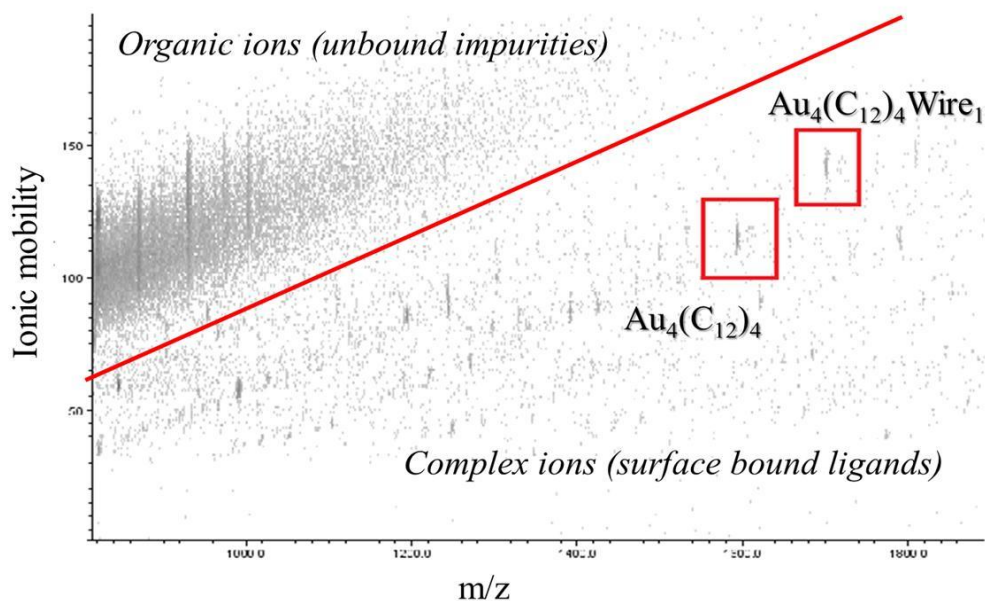


Figure 38: MALDI-IM mass spectrum of AuDodecanethiolate nanoparticles functionalized with the molecular wire. The intensity ratio of the tetrameric species with no wire and the tetrameric species with one wire molecule yields the ratio of dodecanethiolate to molecular wire in the protecting monolayer.

IM-MALDI-MS *allows* for the separation of organic impurities from gold complexes, improving the signal to noise ratio for species important to quantify the surface composition. It was shown that the relative ratios of tetrameric $\text{Au}_4\text{Ligand}_4$ ratios yields accurate quantitation when compared to the standard ^1H NMR analysis that has been used to accomplish this task in the past. In the particular sample in Figure 37, two ions were identified as tetramers: $\text{Au}_4\text{Dodecanethiol}_4$ and $\text{Au}_4\text{Dodecanethiol}_3\text{PEPEPS}_1$. The ratio of the two peaks yields a result of 7 % PEPEPS was present in the nanoparticle monolayer. A second sample with a greater feed ratio of PEPESH (during place exchange) yielded a result of 20% PEPEPS. ^1H NMR quantitation was obscured with this sample, as the solvent residual peak in the spectrum (CDCl_3) interfere with accurate

quantitation, so the values for the average molecular formula of place exchanged AuOctanethiol nanoparticles, discussed later, are treated as only good estimates when compared to the quantitation in the AuDodecanethiol samples that will be discussed.

SECM Qualitative Observation of AuDodecanethiol Electron Transfer Rates

SECM approach curves for Au₁₁₂₀ Dodecanthiolate₆₉₀ exhibited a constant negative current drift through most of the approach, and terminated in a negative feedback, similar to that of the approach to a non-conductive surface. The approach is displayed in Figure 39, below.

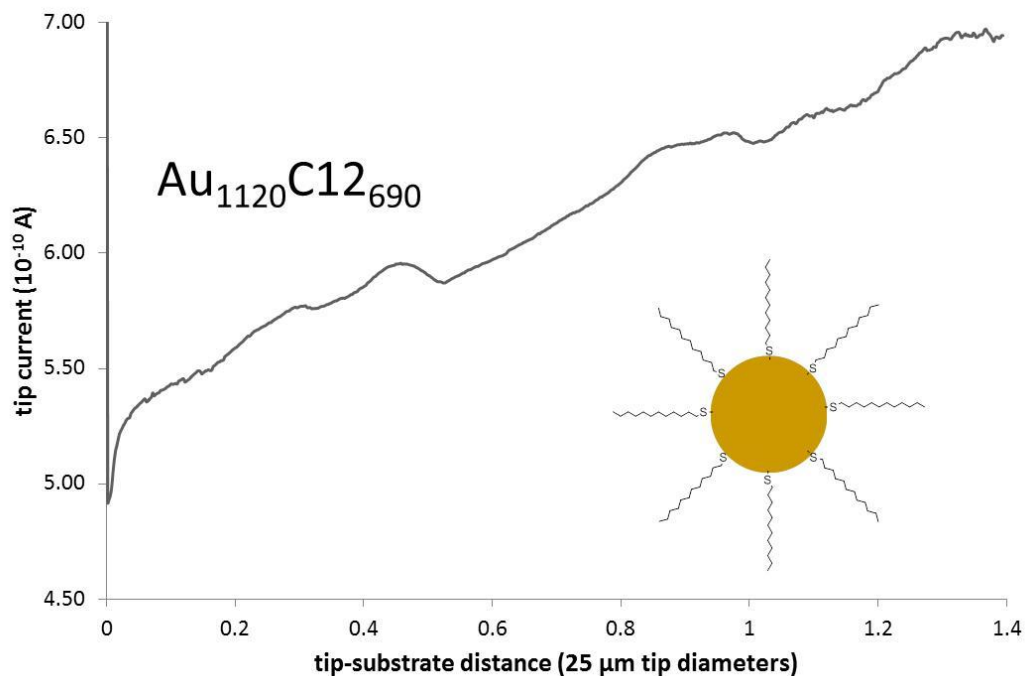


Figure 39: SECM approach curve with 1V Pt UME through larger AuDodecanethiolate nanoparticles, 0V Pt substrate electrode (vs. Ag/Ag^+), in dichloromethane with 0.1M TBAPF_6 . Total tip current instead of normalized tip current is displayed as an accurate, stable value for $i_{t,\infty}$ could not be determined due to the constant current drift.

The negative feedback was, in this case, attributed to a combination of slow electron transfer and slow diffusion. Essentially, when the tip was near the substrate electrode, there was not a higher local concentration of reduced species. It was thought that a layer of oxidized nanoparticle, which has continually diffused from the tip electrode over the course of the entire approach, has created an insulating thin layer cell over the substrate electrode.

When the solution is removed from the cell and replaced with a solution of $\text{Au}_{1120}\text{Dodecanethiolate}_{660}\text{Wire}_{30}$ an entirely different result is obtained, as demonstrated in Figure 40.

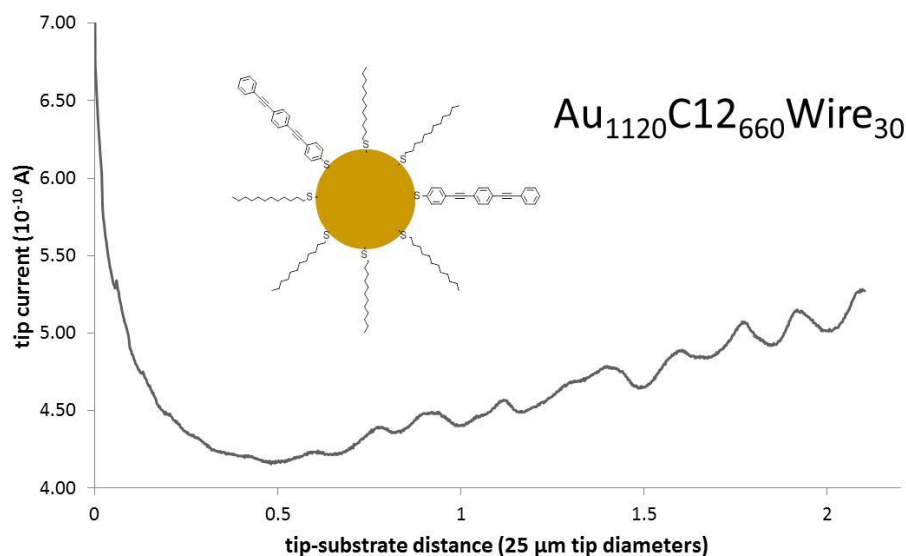


Figure 40: SECM approach curve with 1V Pt UME through larger “wired” $\text{Au}_{1120}\text{Dodecanethiolate}_{660}\text{Wire}_{30}$ nanoparticles, 0V Pt substrate electrode (vs. Ag/Ag^+), in dichloromethane with 0.1M TBAPF_6 .

While the constant drift was still observed in this experiment, a positive feedback finally arose under a half tip diameter away from the substrate electrode. In this instance, it was proposed that the wire imparted fast electron transfer kinetics upon the nanoparticles, and a feedback loop was established close to the surface. The positive feedback result was repeated three times in the same cell with the same electrode. Eventually, the results became irreproducible as absolute tip current was continually lower with each

experiment. Constantly drifting current over the course of multiple experiments suggested that the electrodes were increasingly fouled by excess thiol impurities.

Improved Synthesis of Alkanethiol Nanoparticles Reduces Current Drift

Cleaner preparations of gold nanoparticles were anticipated to solve the problem of negative current drift, presumably due to self-assembly of excess ligand on the UME surface. The improved single phase synthesis discussed below allowed for cleaner nanoparticles without the use of excessive washes with a battery of solvents.

Tetraoctylammonium bromide has been known to stick to the alkanethiolate monolayer in these preparations, as stated by David Schiffrin, one of the authors of the original Brust synthesis paper.¹⁵⁵ TOABr, in turn, presumably holds on to excess thiols present in solution, making purification difficult. To get around this problem, Schiffrin used a lengthy soxhlet extraction which reduced the overall yield.¹⁵⁵

A better way to attain cleaner alkanethiolate nanoparticle preparations that was found was to eliminate the phase transfer reagent completely. Elimination of the phase transfer reagent was accomplished by substituting lithium borohydride for sodium borohydride, allowing for a solvent system of purely anhydrous tetrahydrofuran, instead of a two phase system. Consequently, nanoparticles which were easier to clean post-place exchange were produced. Upon further review of the literature, a very similar method to the one employed had already been published by Rowe and coworkers.⁷ To illustrate how much easier to purify these preparations are, ¹H NMRs of two samples of

AuDodecanethiol nanoparticles (from the two different preparatory methods) prepared with the same stoichiometric amounts of reactants and purified with identical methods are displayed in Figure 41.

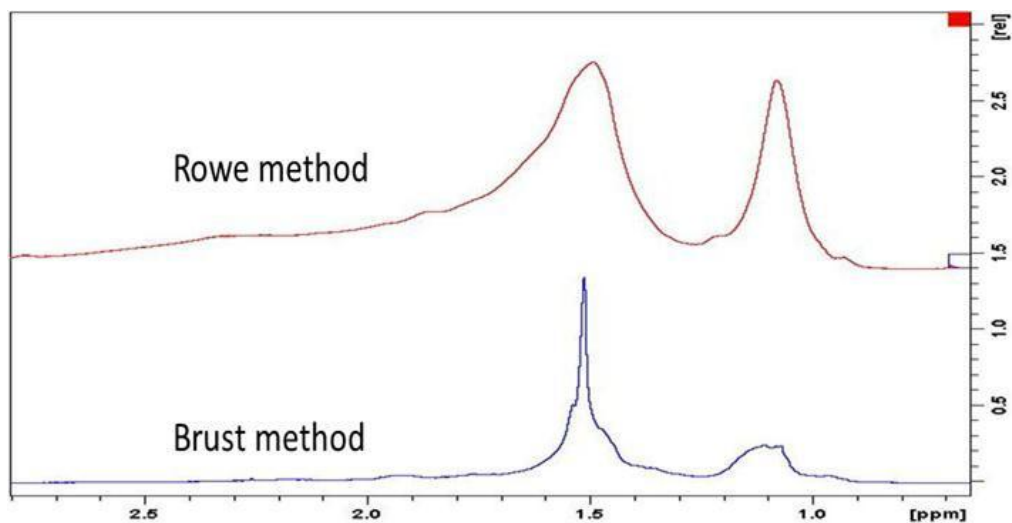


Figure 41: Comparison of ¹H NMR spectra of dodecanethiol gold nanoparticles synthesized by the Brust method (blue), and by the method of Rowe and coworkers (red) after identical purification methods. The red spectrum is visibly cleaner than the blue spectrum judging by the peak width and smoothness.

Both nanoparticle preparations were purified by the same steps of centrifuging out of ethanol once, and then sonicating on glass three times with acetonitrile. Broader and more well-defined peak shapes for the nanoparticles prepared by the method of Rowe and coworkers versus those of the Brust method indicate lower remaining excess thiol, and the lack of tetraoctylammonium. The place exchanged products of these preparations were remarkably easier to clean, very amenable to centrifugation, and if additional dry sonication steps were required, they were generally fewer.

SECM Quantitative Observation of AuOctanethiol Electron Transfer Rates

Using AuOctanethiol nanoparticles produced with the improved method discussed above, it was possible to generate positive feedback approach curves that could be fit to equation 4-5 with some success for both wire functionalized and unfunctionalized samples. Three samples were studied in the same manner as described above (generating approach curves, switching solutions, generating approach curves, switching back to the original solution, repeat ad infinitum) at three different voltages: 200, 400, and 600 mV. The three different samples were Au₂₂₈Octanethiol₉₂ (unfunctionalized), Au₂₂₈Octanethiol₉₀PEPEPS₂ (from exchange with disulfide, PEPS₂), and Au₂₂₈Octanethiol₈₉PEPEPS_{2.6} (from exchange with free thiol, PEPSH). 400 and 600 mV experiments gave comparable results, but the 200 mV experiments were markedly different. The data for the Au₂₂₈Octanethiol₉₂ was baseline corrected, and a numerically identical correction was applied to the other samples in order that equation 4-5 could be fit. The correction eliminated negative current drift due to moisture, impurities, or electrode irregularities; therefore, the values for k_f are relative. The best corrected approach curves generated for wired and unwired gold octanethiol nanoparticles, all at a tip bias of 400mV, are displayed in Figure 42.

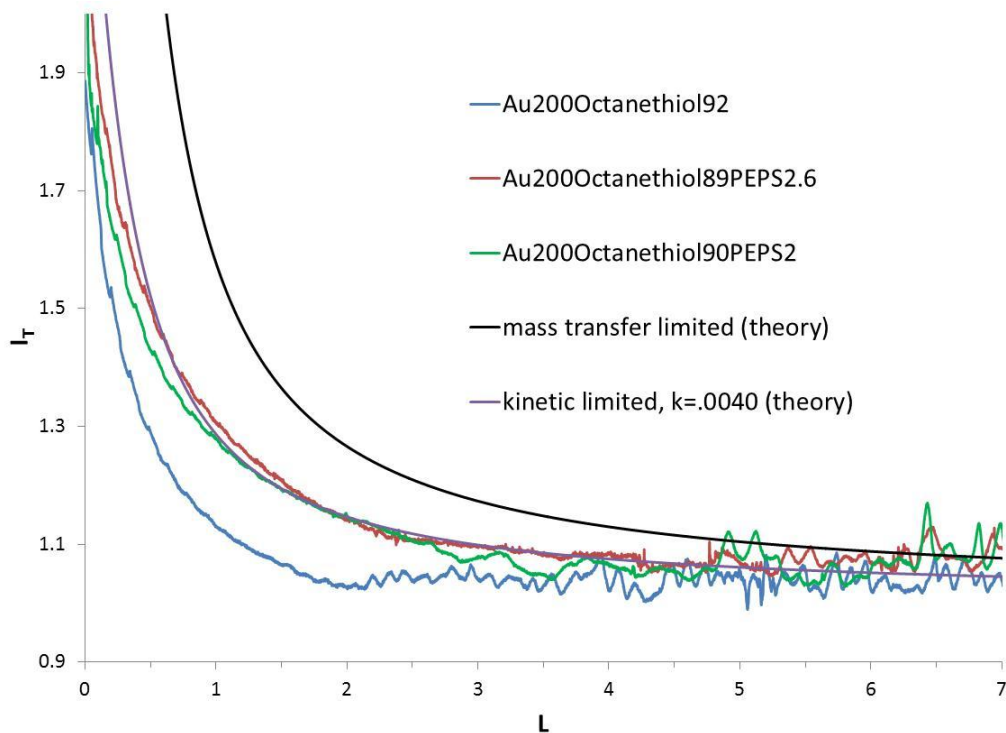


Figure 42: SECM approach curve through Au₂₂₈Octanethiol₉₀PEPEPS₂, Au₂₂₈Octanethiol₉₀PEPEPS_{2.6}, and Au₂₂₈Octanethiol₉₂. Conditions: 25 μm Pt tip at 0.4 V, 2 mm Pt substrate electrode at 0 V (vs. Ag/Ag⁺), 1 mL aliquot of a solution of 5 mg nanoparticle in 20 mL dichloromethane with 0.1M TBAPF₆. The black curve represents the expected result of mass-transfer-only limited system, in accord with equation 4-6, while the purple curve is the kinetic and mass transfer limited theory with $k_f = 0.0040$ cm/s. Bot wire functionalized particles (red and green) have faster electron transfer kinetics than the unfunctionalized particles (blue).

It would be expected that the place exchange percentage from the disulfide would be lower than that of the thiol, but that given a long reaction time, the values of disulfide place exchange would approach that of the thiol place exchange.

Using equation 4-5, it was possible to determine values for k_f , assuming a diffusion coefficient calculated using the Stokes-Einstein equation, $D_{SE} = 2.52 \times 10^{-6}$ cm²/s. The

value of D_{SE} is not dissimilar to values obtained for the diffusion coefficients of other gold-alkanethiolate nanoparticles of a similar core diameter by the Taylor dispersion method.¹⁵⁶ The values for k_f calculated from the curve are gathered in Table 9.

Table 9: Approximate electron transfer kinetic constants determined for $\text{Au}_{228}\text{Octanethiol}_{92-n}\text{PEPEPS}_n$.

n PEPEPS	$k_f(10^{-3} \text{ cm s}^{-1})$
0	1.2
2	3.2
2.6	4.0

In all of these experiments, it should be considered that the mixed kinetic and mass transfer limited model described by equation 4-5 might not entirely describe the system, due to the applied baseline corrections. Additionally, it should be noted that the difference between k_f values obtained for AuOctanethiolate nanoparticles in these experiments ($1.2 \times 10^{-3} \text{ cm/s}$) and AuOctanethiol nanoparticles from the Peterson study ($2.4 \times 10^{-2} \text{ cm/s}$). A number of possibilities were considered. Initially, experiments were hampered by a constant drift, and that was, correctly attributed to a dirty nanoparticle preparation. Having identified and dealt with this problem, further deviations and their possible causes were considered. Absorption of water from air by the dichloromethane is one possible source of deviation. It is thought that water can act as an electron sink, stealing electrons from reduced material as it diffuses back to the tip, causing a drop in feedback current. Another possibility is that the shape of the positive feedback curve is slightly different than expected due to a hemispherical electrode surface or a recessed

electrode surface. The equations used in calculations of electron transfer rate and current are derived assuming a flat disk geometry. Differences in nanoparticle structure are also possible, but difficult to probe or comment on. Possible factors resulting from this are ligand packing, organization, and nanoparticle geometries with more or less edge and vertex sites resulting from slightly different synthetic conditions. Structural differences may have caused the electrons to find slightly different paths to the nanoparticle from a change in distance between the nanoparticle core and the electrode, from a change in the presentation of the ligand orbitals to the electrode, and/or a change in the nature of the double layer.

In conclusion, the data supports the hypothesis that molecular wire molecules behave as conductors on gold nanoparticles in solution, consequently increasing electron transfer kinetics. These functionalized materials can be obtained by straightforward place exchange reactions with the free thiol or disulfide of PEPEPSAc. It seems that a small increase in surface concentration of the wire molecule resulted in a small increase in electron transfer. Much work remains on this topic to characterize the effects of surface concentration, wire size, and wire functional group chemistry. Additionally, MALDI-IM-MS should be more useful than ^1H NMR for quantifying relative amounts of surface ligands due to less interference.

The wired nanoparticle project is currently ongoing. Dave Crisostomo is currently investigating the effects of alkanethiol ligand length, nanoparticle size and dispersity, and PEPEPS surface concentration. Additionally, other electrochemical properties of wired versus unwired alkanethiol nanoparticles are being probed. From there, it would be

valuable to study the variation of molecular wire length by comparison with PEPEPSH to the molecule PEPSH (shorter by one phenylethynyl unit). Due to a lack of success with the standard method to produce PEPSH,¹⁵⁷ which was complicated by the lack of commercial availability of the starting material, alternative synthetic methods for PEPSH are included in Appendix E.

Acknowledgements

I would like to acknowledge Jeremy Wilburn for training me on the use of the SECM and in the fabrication and maintenance of UMEs. I would like to thank Gongping Chen and Fred Hijazi for their assistance with some of the earlier gold dodecanethiol data collected in this study. I would like to further thank Gongping Chen for her assistance with electrode polishing and analysis. Finally, I would especially like to thank Dave Crisostomo for continuing with this work.

CHAPTER V

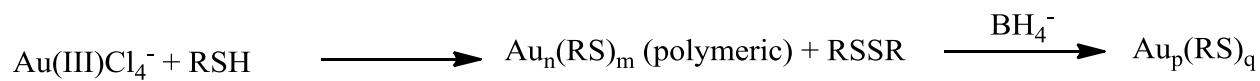
KINETIC INVESTIGATION OF TIOPRONIN PROTECTED GOLD NANOPARTICLE PRECURSOR FORMATION

Introduction

Much interest as has been paid to the variation of synthetic parameters and the consequences on nanoparticle formation;^{63, 158-165} however, the approaches have not adequately addressed fundamental issues about the formation of intermediate species on the way to the final nanomaterial. The experiments that follow attempted to gain insights into the make-up of the precursor material and how it is formed. Short of proposing a full mechanistic understanding of all aspects of gold nanoparticle precursor formation, this work addressed a number of important questions along this path. This chapter focuses primarily on the precursor formation during the synthesis of tiopronin protected gold nanoparticles as first synthesized by Templeton and coworkers¹²², but slightly modified to better interrogate the system.

Background

The modified Brust method employed by Templeton and coworkers had long been theorized to proceed by Scheme 5-1:



Scheme 5-1: General reaction scheme for the Brust method of nanoparticle synthesis. The reactions are unbalanced and Cl^- and H^+ are not shown as products. $\text{Au}_p(\text{RS})_q$ represents the final nanoparticle with a core of p Au atoms and a shell of q RS molecules.

On the basis of a mass spectrometry study by Geis and coworkers²⁷ and a later powder diffraction study by Simpson and coworkers (43c),¹⁶⁶ the tiopronin system is thought to go through the stable $\text{Au}_n(\text{RS})_m$ intermediate in Scheme 5-1, a tetrameric ring structure (Figure 43c). Later, in a landmark x-ray crystallographic study, Kornberg and coworkers (Figure 43a)⁴³ discovered Au-SR-Au staple motifs⁴⁵ on the surface of gold nanoparticles protected by p-mercaptobenzoic acid (PMBA) (Figure 43b). Further x-ray crystal structures of other monodisperse gold nanoparticles prepared by the Brust method or some variation on it displayed similar capping structures on the surface. Gold thiolate capping structures had been predicted earlier, computationally, by Häkkinen and coworkers.⁴²

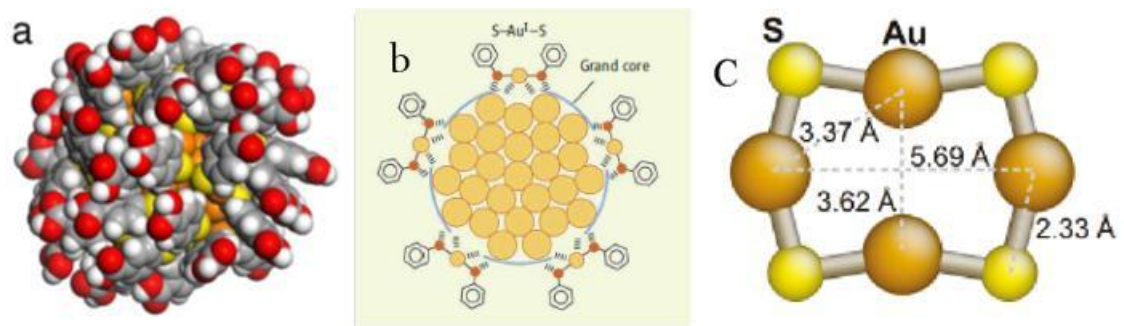
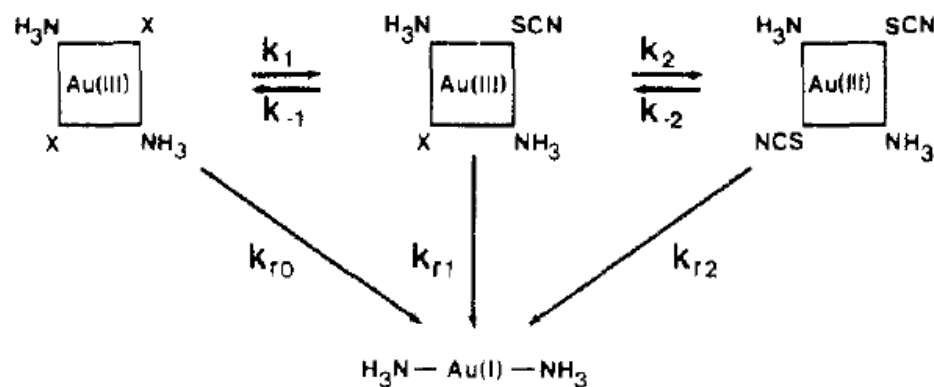


Figure 43: Nanoparticle and ring complex structures (a) PMBA nanoparticle crystal structure proposed by Jadzinsky, et. al.,⁴³ from Walter, et. al.¹⁶⁷ Copyright 2008, National Academy of Sciences, reused with permission. (b) PMBA staple motifs, from Whetten and Price,⁴⁵ Copyright 2007, American Association for the Advancement of Science, reused with permission, and (c) Au₄Tiopronin₄ cyclic structure (R group of tiopronin now shown), Amsterdam density functional theory prediction from Simpson, et. al.¹⁶⁶ Copyright 2010, American Chemical Society, reused with permission.

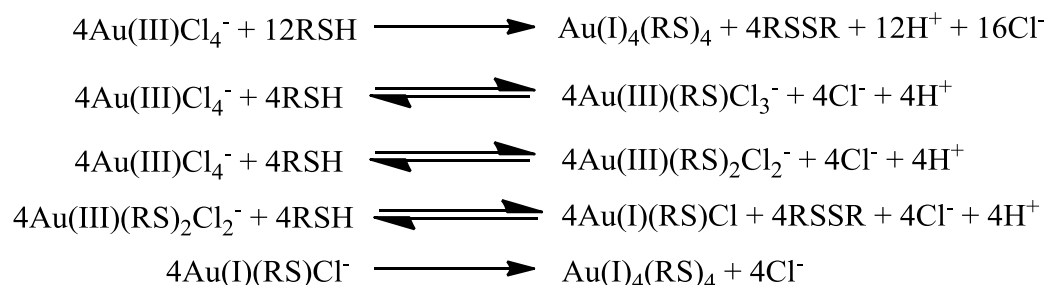
Notably, the precursor material formed before the final borohydride reduction, whether a cyclic or chain polymer structure, bears structural similarity to the capping structures in the reported crystal structures. Harkness and coworkers demonstrated that different ligands prefer different cyclic stoichiometries (some with equal but greater or lesser numbers of gold and thiol per cycle), but that tiopronin prefers the cyclic tetramer (four gold atoms and four thiolate molecules) completely.¹⁶⁸ Furthermore, these precursor structures can be liberated from gold nanoparticles and measured using MALDI-MS. It is clear that gold nanoparticles are not always, and possibly never can be, a solid gold core surrounded by a ligand shell. Instead, it appears that there is a solid grand core and a loose ligand-gold shell which structurally resembles the precursor material. Better understanding of the precursor material and its formation, therefore, is important to the continued progress in the synthesis of Brust nanoparticles.

The ligand exchange and reduction of Au(III) complexes has been the subject of a small number of prior studies; consequently, discussion of some of the more prominent results is prudent. Elding has studied the exchange and reduction of Au(III) halides. Notably, as a possible analogue to this study, they fully characterized the ligand exchange kinetics and subsequent reduction of haloamminegold(III) with thiocyanate,¹⁶⁹ with dimethylsulfide,¹⁷⁰ and with thione containing ribonucleic acids.¹⁷¹ The general scheme that they deduced for the reaction of haloammineaurate with thiocyanate, displayed in Scheme 5-2, seemed to proceed in a similar fashion to what was visually observed for the reaction of gold and tiopronin.



Scheme 5-2: Reaction pathways for the exchange and reduction of haloamminegold(III) by thiocyanate, as proposed by Elmroth and coworkers.¹⁶⁹ Copyright 1989, American Chemical Society, reused with permission.

None of the literature reviewed¹⁷²⁻¹⁷⁴ reports kinetics and mechanism for the reaction of a terminal organic thiol or thiolate with Au(III)Cl_4^- , but the following Scheme 5-3 for this reaction was generated with the cited studies for other sulfur containing molecules in mind.



Scheme 5-3: Plausible reaction mechanism for the reaction of Au(III)Cl_4^- with tiopronin featuring competitive ligand exchange and reduction.

In the current study, the theories discussed above in the context of standard kinetic and mechanistic study of transition metal complexes, as presented by Wilkins,¹⁷⁵ were applied to the reaction between Au(III)Cl_4^- and tiopronin. With the results, the research aimed to provide insights on the pre-reduction steps of small gold nanoparticle syntheses of similar to the Brust method. Specifically, the Au(III) /tiopronin system was chosen as it leads to stable high-yield water-soluble clusters by straightforward methodology, as discussed in Chapter I. Knowledge of the pre-reduction conditions will aid researchers in developing standardized and better informed synthetic methods and, ultimately, routes to new nanomaterials. Indeed, Hainfeld and coworkers have already studied the variation in nanoparticle size with the variation in the size of the precursor polymer for the glutathione/tetrachloroaurate system.¹⁷⁶ The hypotheses were motivated by Richard Feynman's claim that "there is plenty of room at the bottom," as studying the complexes

prior to nanoparticle formation represents the basement of the nanoparticle synthesis picture.

Methods

Materials

For this section only, $\text{HAuCl}_4^- \cdot 3\text{H}_2\text{O}$ was purchased from Sigma-Aldrich, along with optima methanol, 70% perchloric acid, and tiopronin. Sodium perchlorate (biology grade) and sodium chloride were purchased from Fisher scientific.

UV-Visible Spectroscopy Kinetics Experiments

A Cary Bio-100 UV-Vis spectrophotometer was used to probe the initial rates, and full kinetic profiles of reactions between varying amounts of $\text{HAuCl}_4^- \cdot 3\text{H}_2\text{O}$ and tiopronin. Stock solutions of gold in methanol were prepared, and dilutions of this stock in methanol or salt/methanol were measured into 1 cm quartz cuvettes, and initial spectra were obtained. Then, an Eppendorf Research digital or Reference manual micropipette was used to inject an aliquot of a tiopronin stock solution in methanol or salt/methanol into the cuvette, followed by rapid mixing via blowing air through with a glass pipette and quickly shutting the instrument cover. Keeping the room dark allowed for reduction of the interference from other light sources just post-injection. Using the simple kinetics or scanning kinetics software packaged with the instrument, the change in the absorbance

peak at λ_{max} (local) = 320 nm is observed over a period of 15 minutes or up to 3 hours depending on the speed of the individual reaction and what information was desired. Points were taken continuously for the first 1 to 3 minutes, and then every 30 seconds to 1 minute thereafter. In order to investigate medium effects, stock solutions of 100 mM NaCl in methanol, 100 mM sodium perchlorate in methanol, or 101 mM perchloric acid in methanol were occasionally used for dilution or added to achieve the desired concentrations/ionic strengths.

Results and Discussion

Preliminary Observations

The reaction of Au(III)Cl_4^- with tiopronin in methanol has been followed at various stoichiometries, and the products have been characterized. At a $[\text{RSH}]:[\text{Au(III)}] < 3:1$, fading of the solution, suggesting the reduction of Au(III) to Au(I) is observed. If allowed to stand longer, the solution returns to yellow and the deposition of gold metal on the reaction vessel confirms the disproportionation of Au(I) to Au(III) and Au metal, as described by Gammons and coworkers.¹⁷⁷ At $[\text{RSH}]:[\text{Au(III)}] \geq 3:1$, the solution fades over the course of about an hour to clear, followed by precipitation of a white solid over the course of subsequent hours. Increasing $[\text{RSH}]:[\text{Au(III)}]$ from 3:1 to 5:1 changes the appearance of the white precipitate from more powdery to more ribbon like. It can be concluded from these observations that the stoichiometry of reaction is at least 3:1, which is consistent with the 4:1 ratio that is expected.

UV-Visible Spectroscopy

Given the bright color of its complexes in solution, the spectroscopic determination of Au(III) is straightforward. In the case of tetrachloroaurate(III), two absorbance maxima in the UV-Visible spectrum are readily apparent at 320 nm and 271 nm. During reduction of Au(III) to Au(I) by tiopronin, the band at 320 nm decreased in absorbance intensity over time, and a saddle with the absorbance at 271 nm near 288 nm was observed. A second saddle between the 271 nm absorbance maximum and a shoulder to the right of that peak was observed at about 250 nm. Time resolved spectra are presented in Figure 44 below.

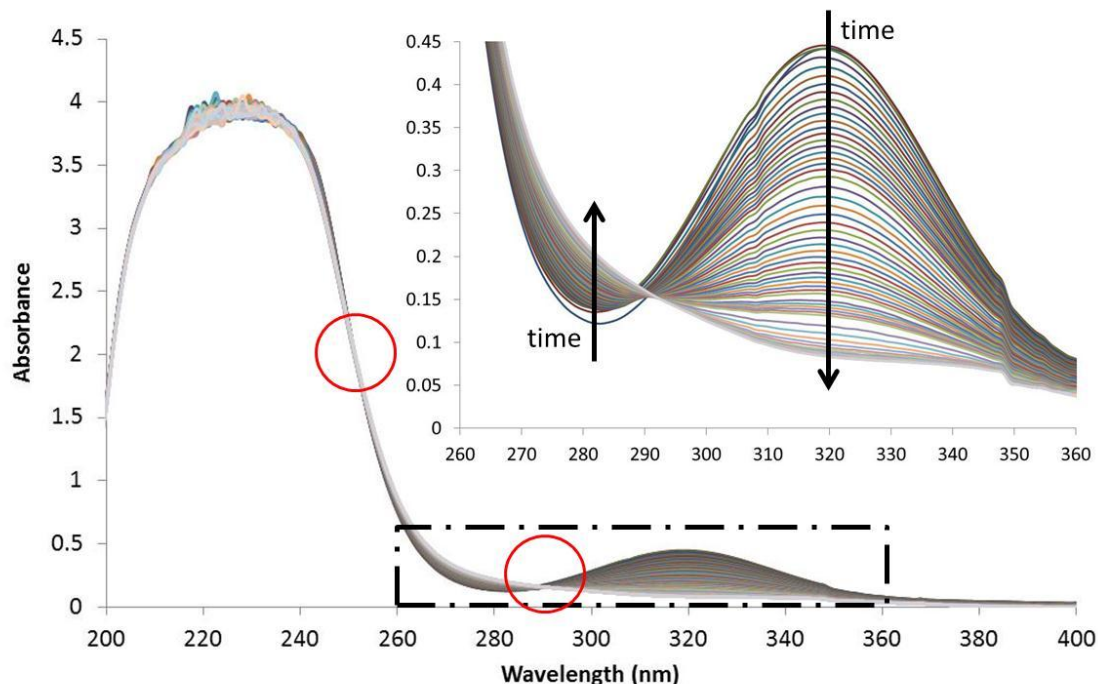


Figure 44: Time resolved UV-Vis spectra of AuCl_4^- undergoing reduction by tiopronin. For this specific experiment, the initial conditions were $[\text{tiopronin}] = 16.9 \text{ mM}$, $[\text{HAuCl}_4] = 0.0955 \text{ mM}$, $[\text{HClO}_4] = 6.00 \text{ mM}$, $[\text{NaCl}] = 1.00 \text{ mM}$, and $[\text{NaClO}_4] = 101 \text{ mM}$, all in methanol. Spectra were collected at approximately 30 s intervals for the first 1 min, every 1 min for the next 30 min, and every 5 min for the next 145 min. All spectra were collected at a scan rate of 20 nm/s with a spectral bandwidth of 2 nm. The local absorbance maxima at 320 nm (inset, zoomed in) started at $A = 0.442$, initially increased to $A = 0.445$ for the second scan, and decreases to a minimum of $A = 0.0833$ after 110 min of reaction time ($\pm 5 \text{ min}$). Isosbestic points at 250 nm and 288 nm are circled in red.

Upon further examination of the region around the saddle at 289 nm, the presence of an intermediate was apparent as the intensity just to right of the saddle initially increased, and just to the left initially decreased, as displayed in Figure 45.

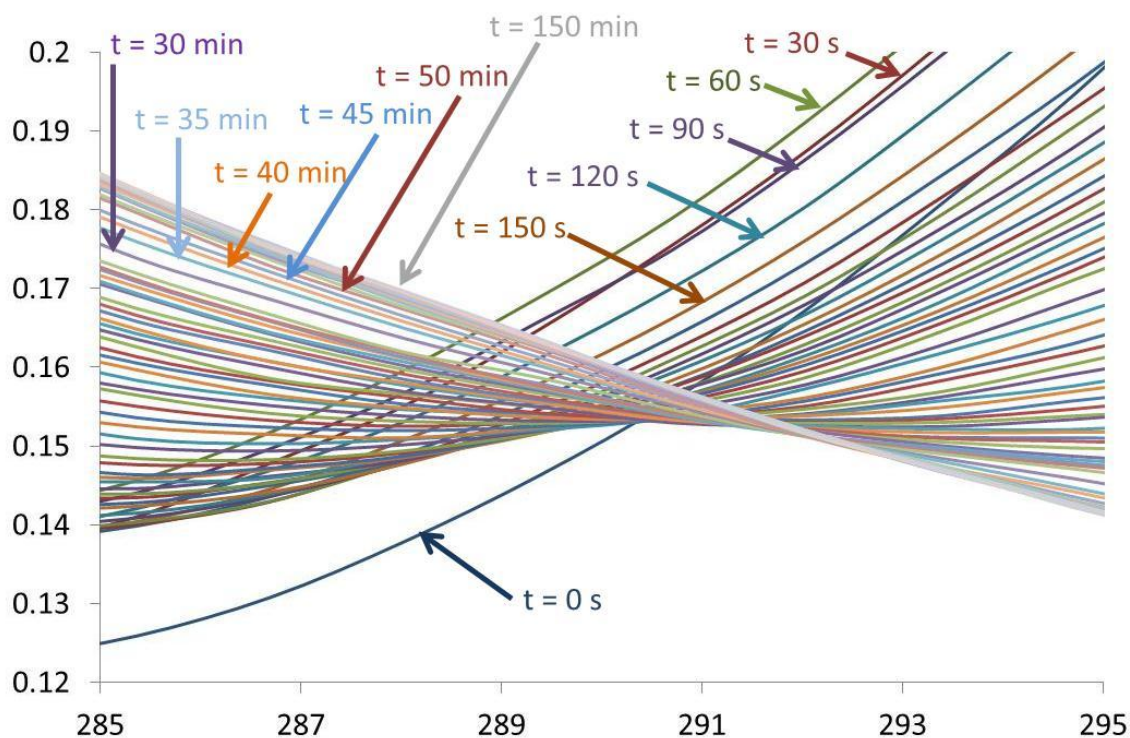


Figure 45: UV-Vis region containing the saddle at 289 nm for the gold(III)/tiopronin system. Colored arrows and labels correspond with the start time of each scan from the reaction start time for the corresponding colored spectra. Note the initial increase in intensity to the right of the saddle followed by a rapid decrease, and the opposite phenomenon on the left.

Eventually, the direction of absorbance change became a decrease to the right of the saddle and an increase to the left of the saddle. The presence of the two saddles in combination with the deviations in intensity change direction during the first 1 minute of reaction is consistent with a transition that originated from an intermediate species. This intermediate species is probably a substitution product, but could possibly be a 5-coordinate intermediate preceding the substitution product¹⁷⁸ or an intermediate for the reduction process with a second or third thiol bound to a substituted thiol, or a combination of any or all of the mentioned species.

The nature of the absorbance changes and multiple isosbestic points presented problems with accurate spectroscopic determination of Au(III). For instance, the non-zero absorbance upon completion of the reduction reaction at 320 nm could have been interpreted as an incomplete reaction, dynamic equilibrium, or interference from the tail of a transition not associated with Au(III). Also, the changing dynamics of the 320 nm absorbance band suggests that a combination of interference from another transition and/or a change in extinction coefficient may have caused a significant deviation in accurate determination of Au(III) concentration from the spectrum. Given few options to circumvent these difficulties, a kinetic analysis of the data was undertaken with the assumption that Au(III)Cl_4^- was chiefly responsible for the absorbance band at 320 nm.

When tetrabromoauric acid (HAuBr_4) was analyzed by identical methodology, a complete disappearance of the absorbance band at 390 nm was observed upon reduction with tiopronin, as illustrated in Figure 46. The kinetics of this system were difficult to evaluate quantitatively as the reaction was too fast to measure without a stop-flow system.

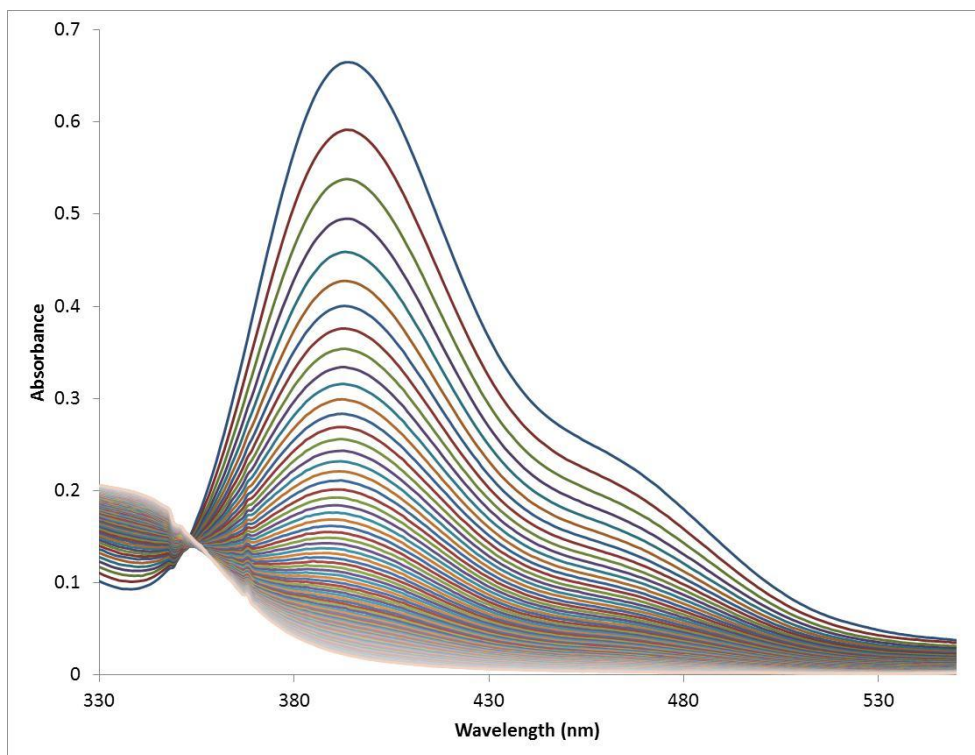


Figure 46: Time resolved UV-Vis spectra of tetrabromoauric acid undergoing reduction by tiopronin.

Given the fast kinetics and the lack of sufficient instrumentation to measure them accurately, the gold chloride system will be the focus of the discussion that follows.

The overall process that can be monitored with UV-visible spectroscopy by observing the decrease in absorbance at 320nm which corresponds to the reduction of Au(III) (yellow) to Au(I) colorless in the presence of excess tiopronin. Using Beer's law, a calibration curve for Au(III)Cl_4^- is easily obtained yielding an extinction coefficient of $\epsilon_{320\text{nm}} = 4660 \text{ M}^{-1} \text{ cm}^{-1}$, which is reasonably consistent with reported literature values. The dynamic

reaction profiles of three reactions at variable [RSH] and fixed [Au(III)Cl₄⁻] are shown below in Figure 47.

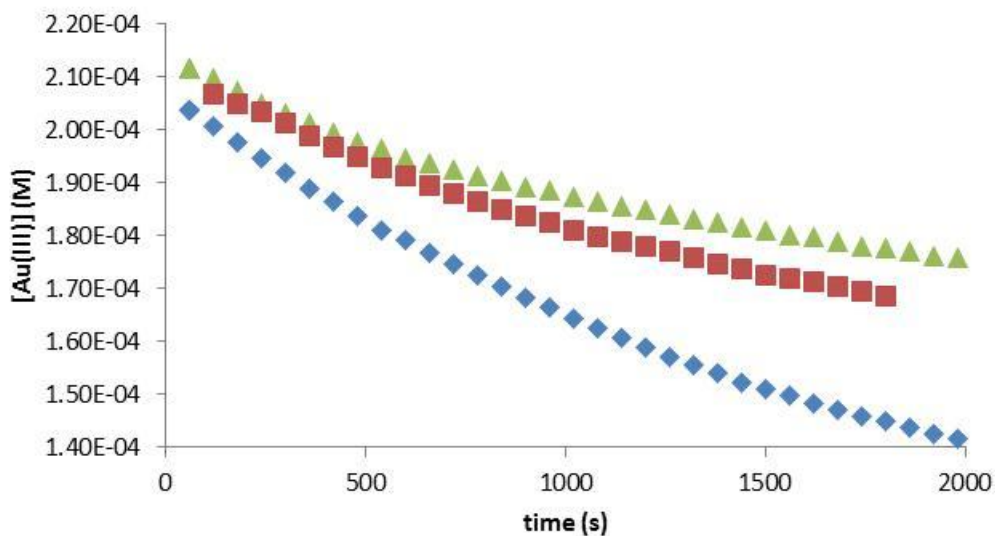


Figure 47: Dynamic reaction profiles of Au(III)Cl₄⁻ with tiopronin in a 3:1 (green), 6:1 (red), and 9:1 (blue) molar ratio.

Treating this reaction as a pseudo first order process, the rate law is:

$$-\frac{d[\text{Au(III)Cl}_{4-y}\text{RSH}_y]}{dt} = k[\text{Au(III)Cl}_{4-y}\text{RSH}_y]^m \quad (5-1)$$

where t is time in seconds, k is the pseudo rate constant, y is an integer value from 0 to 2, and m is the integer order of reaction with respect to the corresponding species. For

simplicity going forward, [Au(III)] will be considered as the concentration of all Au(III) species in solution. Pseudo first order conditions are followed when the dynamic reaction profile can be fit to the following linear equation if the process is first order with respect to AuCl_4^- ,

$$\ln[\text{Au(III)}]_t = \ln[\text{Au(III)}]_0 - kt \quad (5-2)$$

or to the following linear equation in the event that it is second order with respect to AuCl_4^- :

$$\frac{1}{[\text{Au(III)}]_t} = \frac{1}{[\text{Au(III)}]_0} + kt \quad (5-3)$$

Fitted plots are displayed below in Figure 48.

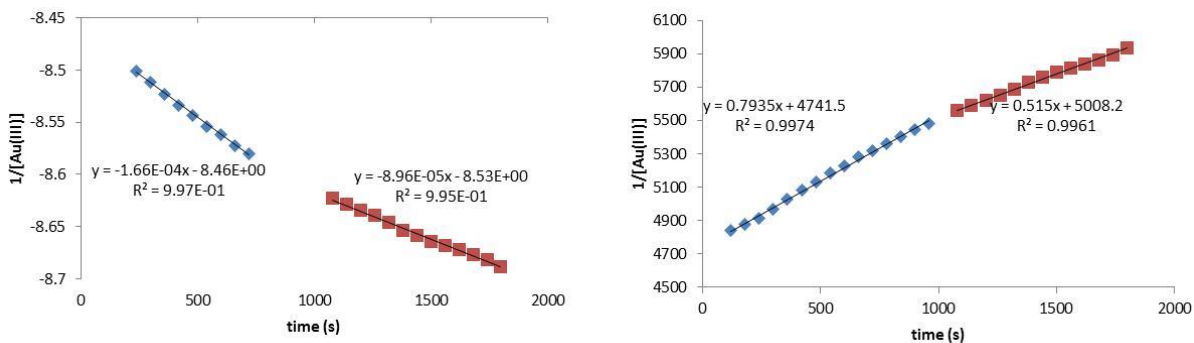


Figure 48: Plots to determine the order of reaction with respect to Au(III)Cl_4^- in pseudo first order conditions, both first order (left) and second order (right). Blue represents points from earlier time points in the reaction and red represents later time points in the reaction.

As the entire profile would not fit to either equations 5-2 or 5-3 for the entire process, the common conclusion is that there are consecutive reactions occurring. Indeed, if the plot is broken into two parts, linear fits are found for either first or second order for either time regime during the reaction course. Discrimination of first and second order processes by this method can be difficult. In the analysis that follows, only observation of the reduction process by the method of initial rates under pseudo first order conditions was attempted. The first step in the process was to vary $[\text{Au(III)Cl}_4^-]$ in deficiency with respect to tiopronin, shown in Figure 49 below.

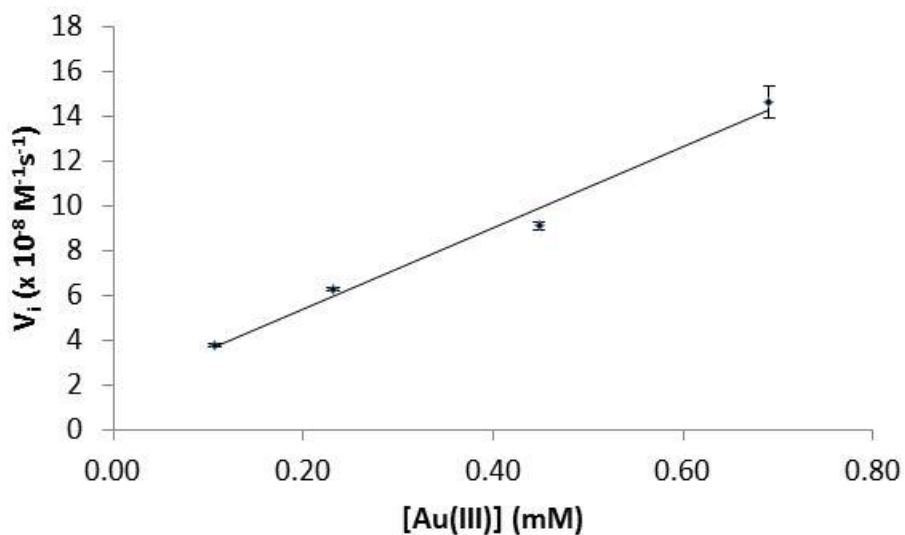


Figure 49: Plot to determine the reaction order and pseudo first order rate constant with respect to [Au(III)].

The relationship was nearly linear ($R^2 = 0.988$), but when examined more closely, it was apparent that the reaction order with respect to [Au(III)] was closer to $m = 2/3$. In order to convert the pseudo rate constant, k , to the real rate constant(s), the concentration of tiopronin, [RSH], was systematically varied. The rate data is presented in Table 10, and the variation of $k_{Au(III)}$ with [RSH] is displayed in Figure 50.

Table 10: Rate data for the reaction of Au(III)Cl_4^- with tiopronin in MeOH at unfixed ionic strength. The percent difference between the initial rate calculated using the rate law and the observed initial rate is taken as a measure of the usefulness of the rate law within this concentration regime to predict the initial rate of the initial process.

V_i ($\times 10^{-8} \text{ M s}^{-1}$)	$[\text{RSH}]/$ $[\text{Au(III)}]$	$[\text{RSH}]_i$ ($\times 10^{-3} \text{ M}$)	$[\text{Au(III)}]_i$ ($\times 10^{-3} \text{ M}$)	($\times 10^{-5} \text{ M}^{-$ $(2/3) \text{ s}^{-1}$)	$V_{i,\text{law}}$ ($\times 10^{-8} \text{ M s}^{-1}$)	% difference $V_{i,\text{law}}:V_i$
1.50	3.02	0.68	0.22	0.41	1.55	2.90%
2.94	6.71	1.35	0.20	0.85	2.89	-1.55%
4.59	9.67	2.03	0.21	1.29	4.46	-2.90%
6.30	11.68	2.71	0.23	1.66	6.35	0.68%
9.14	6.04	2.71	0.45	1.55	9.85	7.22%
14.65	3.92	2.71	0.69	1.87	13.14	-11.46%
3.77	25.39	2.71	0.11	1.67	3.78	0.30%

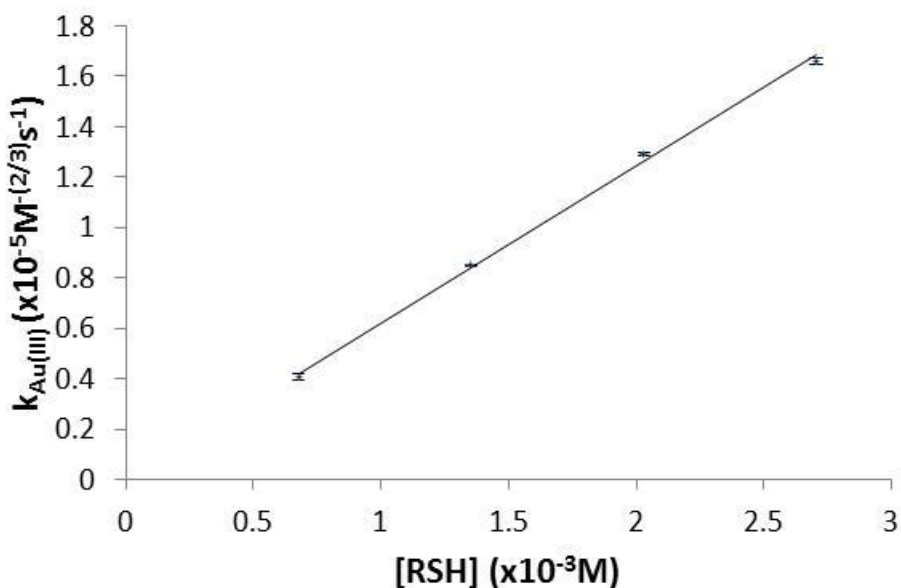


Figure 50: Plot to determine the order of reaction with respect to $[\text{RSH}]$, n , and the overall rate constant, k_{net} . The linear relationship signifies $n = 1$ and the slope is thus interpreted as the overall $5/3$ order rate constant.

The observed kinetic behavior corresponded with a reaction that was first order with respect to [RSH], and the overall second order rate constant was determined as the slope of the plot in Figure 48, according to the following equation:

$$k_{\text{Au(III)}} = k_{\text{net}}[\text{RSH}] \quad (5-4)$$

where k_{net} is the second order rate constant and the pseudo first order rate constant discussed earlier, k , has been re-labeled as $k_{\text{Au(III)}}$ for convenience. Therefore, $k_{\text{net}} = 6.22 \times 10^{-3} \text{ M}^{-2/3} \text{ s}^{-1}$ for the reaction at standard nanoparticle synthesis conditions (RSH: Au(III) < 5, room temperature, no adjustment to ion strength, no adjustment to pH).

In the event of a non-zero y-intercept, the following equation is necessary to describe the full rate law:

$$-\frac{d[\text{Au(III)}]}{dt} = k_1[\text{Au(III)}]^c + k_{\text{net}}[\text{Au(III)}][\text{RSH}] \quad (5-5)$$

where k_1 and c describe a second process for the reduction that is independent of [RSH]. However, the y-intercept is however insignificant compared to the variability of rates determined by the full rate law from the observed rates ($k_1[\text{Au(III)}] \ll \% \text{ difference}$), and can be ignored. It should be noted that Au(III) solutions degrade over time, and, given more accurate analytical methods, a small but measurable k_1 value would not be unexpected (*e.g.* solvolysis). That being said, a final rate law for the initial process in the reaction is determined to be:

$$V_1 = -\frac{d[\text{Au(III)}]}{dt} = k_{net}[\text{Au(III)}]^{2/3}[\text{RSH}] \quad (5-6)$$

While this rate law is practical for determining reaction velocities under conditions used during the synthesis of gold tiopronin nanoparticles, there are a number of shortcomings in using it to predict a mechanism. Furthermore, the the 2/3 order in [Au(III)] would imply an exotic mechanism, which raises skepticism.

Here, it is prudent to consider the effect of medium and other participants in the reaction. For instance, the variability of [H⁺] over the course of the reaction could have a varying medium or mechanistic effect on the rate, as both reagents are acidic, and, at some point, hydrogen atoms are lost from the tiopronin thiol groups, possibly as protons. It is also suspected that the [H⁺] concentration effects solvolysis and esterification reactions between primary reactants and solvent molecules (methanolysis, hydrolysis,¹⁷⁹ and methanol esterification). Another similar issue is with the [Cl⁻], as chloride is liberated from AuCl₄⁻ as tiopronin participates in equilibrium exchange reactions with gold prior to the final reduction. This would lead to a rate constant of the type:

$$k_{net} = k_{\text{Au(III)}}[\text{RSH}]^b[\text{Cl}^-]^c[\text{H}^+]^d \quad (5-7)$$

A handful of experiments were studied to assess the impact of [Cl⁻] and [H⁺] on the initial reaction under similar conditions to those above. The results are summarized in Table 11.

Table 11: Rate data at fixed [RSH] and [Au(III)] with variable [H⁺] (adjusted with perchloric acid/MeOH solution) and [Cl⁻] (adjusted with sodium chloride/MeOH solution). The concentrations are calculated assuming complete dissociation, although some ion pairing is expected to occur. Blue highlights the experiments where [Cl⁻] was varied and pink highlights experiments where [H⁺] was varied, while an experiment with no added [H⁺] and [Cl⁻] is in white. (a) indicates that while no [H⁺] was added, the exact [H⁺] concentration from dissociation of HAuCl₄ and the carboxylic acid group of tiopronin was not determined.

V _i (x 10 ⁻⁸ M s ⁻¹)	[RSH]/ [Au(III)]	[RSH] _i (x 10 ⁻³ M)	[Au(III)] _i (x10 ⁻³ M)	[H ⁺] _i (x10 ⁻³ M)	[Cl ⁻] _i (x10 ⁻³ M)	relative rate
1.27	26.27	2.71	0.10	a	16.67	0.34
1.29	21.43	2.71	0.13	a	4.17	0.34
1.24	25.44	2.71	0.11	a	1.07	0.33
2.28	23.52	2.71	0.12	38.67	0.00	0.60
2.17	24.59	2.71	0.11	77.33	0.00	0.57
2.67	28.36	2.71	0.10	116.00	0.00	0.71
3.77	25.39	2.71	0.11	a	0.00	1.00

It was determined that the presence of both initial [H⁺] and [Cl⁻] retard the reaction rate, but not in a concentration dependent fashion (at least not within the range studied here). Initial [Cl⁻] reduces the rate of reaction to about 1/3 and [H⁺] reduces the rate to about 2/3 of what it was without the presence of either species. Reduction in rate with the addition of substitution side products was consistent with a mechanism where both species were on the product side of an equilibrium process pre-reduction, which was suspected on the basis of previously mentioned mechanistic work on Au(III) reduction reactions. A variation of rate with concentration of either species might have been observed at lower concentrations of those species. Importantly, that the effects of [H⁺] on rate might have been attributable to other processes or species generated in the stock solution, such as methyl perchlorates, methyl esterified tiopronin, or hydrolyzed AuCl₄⁻, should be restated.

Additionally, the total ionic strength of the solution effects the kinetics of any reaction, especially those between charged species. In the current case, AuCl_4^- , Cl^- , and H^+ were all charged and likely were involved in the reaction. Ionic strength influences the reaction by mediating collisions between charged and polar species. The effect on rate constant was given by the following equation:

$$\log k = \log k_0 + \frac{2\alpha z_A z_B \mu^{1/2}}{1 + \mu^{1/2}} - \beta \mu \quad (5-8)$$

where k is the rate constant as a function of ionic strength μ , k_0 is the rate constant at zero ionic strength, z is the charge on reactant A or B, and α and β are free parameters. The $-\beta\mu$ term is to correct for ion pairing effects. This equation could be useful to either extrapolate rate constants determined at a given ionic strength to the reaction at low ionic strength, or to back out the ionic strength given the experimentally determined rate constant.

Accommodations should be made if the total reaction chain is suspected to have pre-reduction equilibria, or a final equilibrium state, since the reaction could very well exhibit a kinetically limited behavior at elevated concentrations of either reactant. This phenomenon is known as saturation kinetics. The initial reaction velocity, in this case, is given by a rate law of the form:

$$V_{i,sat} = -\frac{d[\text{Au(III)}]}{dt} = k[\text{Au(III)}] = \frac{a[\text{Au(III)}][\text{RSH}]}{1 + b[\text{RSH}]} \quad (5-9)$$

where a and b are experimentally determined parameters that relate to rate constants in different concentration regimes. If $b[\text{RSH}] < 1$, then the second order reaction is observed, and $k = a$. If $b[\text{RSH}] \sim 1$, then the reaction is mixed order. Eventually, if $b[\text{RSH}] > 1$, then the reaction is first order in Au(III), with $k = a/b$. The values of a and b can be determined by plotting a linearized form of the rate law as follows:

$$\frac{1}{k} = \frac{1}{a[\text{RSH}]} + \frac{b}{a} \quad (5-10)$$

where k will be considered k_{net} for $n = m = 1$ and the slope and intercept are interpreted as $1/a$ and b/a , respectively.

The experiments outlined in Table 12 were performed to evaluate saturation kinetics at fixed ionic strength. Saturation behavior was apparent (via observation of a loss in linearity, $R^2 = 0.9649$) in a plot of $k_{\text{Au(III),I}}$ versus $[\text{RSH}]$ at higher $[\text{RSH}]$ and higher $[\text{RSH}]:[\text{Au(III)}]$, displayed in Figure 51.

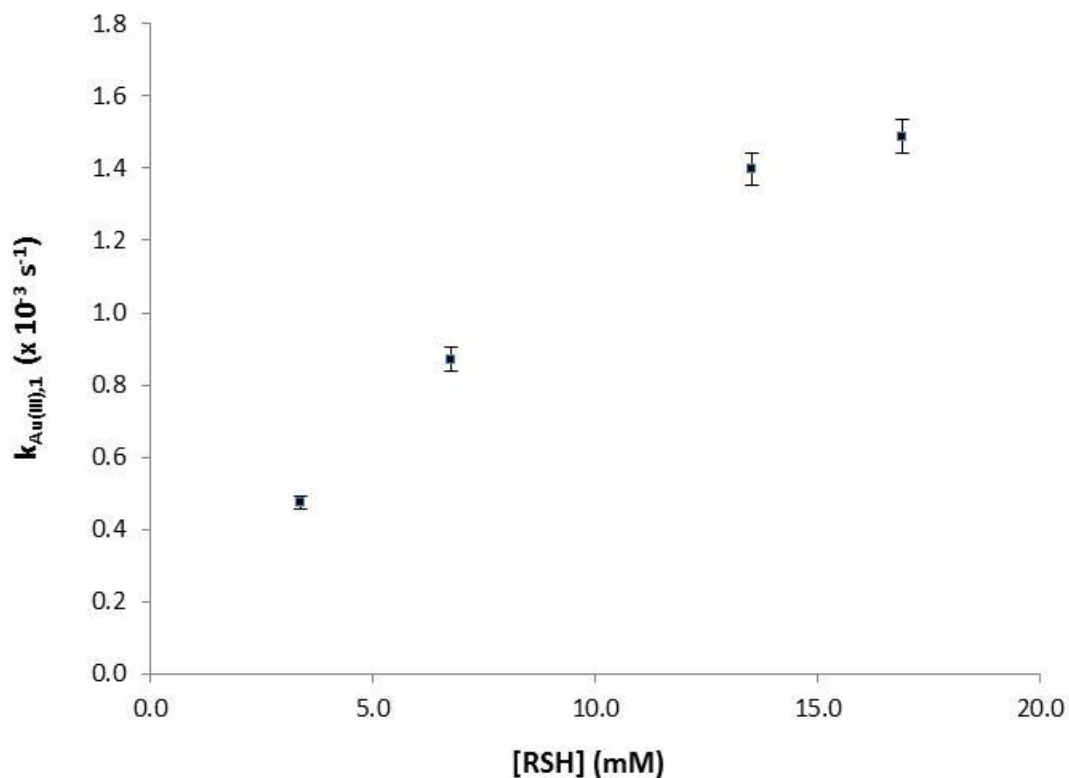


Figure 51: Saturation behavior was suspected when $k_{\text{Au(III)},1}$ lost a linear relationship with [RSH] at higher [RSH].

Table 12: Rate data for conditions designed to test saturation kinetics of the tiopronin/tetrachloroaurate system. All experiments in 101 mM NaClO₄ in methanol. $k_{\text{Au(III)},1}$ is the first order rate constant in this table, not the fractional 2/3 order determined previously. Blue highlights data where [Au(III)] was varied and pink highlights data where [RSH] was varied. The calculated rate data is described in the following text.

V_i ($\times 10^{-8} \text{ M s}^{-1}$)	[RSH]/ [Au(III)]	[RSH] _i ($\times 10^{-3} \text{ M}$)	[Au(III)] _i ($\times 10^{-3} \text{ M}$)	$k_{\text{Au(III)},1}$ ($\times 10^{-3} \text{ s}^{-1}$)	$V_{i,\text{sat}}$ ($\times 10^{-8} \text{ M s}^{-1}$)	% difference $V_{i,\text{sat}}:V_i$
4.59	344	16.9	0.0492	0.932	7.72	40.6%
32.7	89.0	16.9	0.190	1.724	29.81	-9.8%
65.4	41.8	16.9	0.404	1.617	63.47	-3.1%
14.1	179	16.9	0.0945	1.488	14.83	5.2%
12.9	147	13.5	0.0922	1.399	12.66	-1.9%
8.04	73.2	6.76	0.0924	0.871	7.80	-3.1%
4.56	35.2	3.38	0.0961	0.474	4.59	0.7%

The rate law determined previously was insufficient to characterize the reaction over a large [RSH] span, so the rate law in equation 5-9 was applied by determining coefficients a and b by using the linearized version, equation 5-10. The plot is displayed in Figure 52.

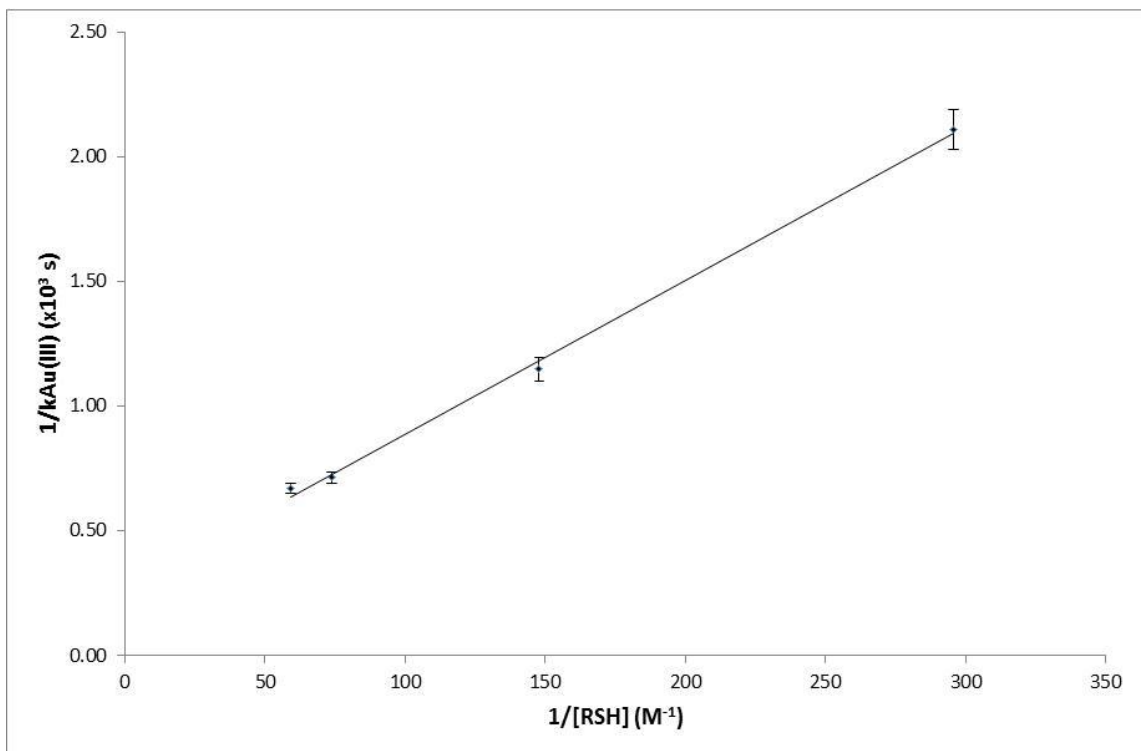
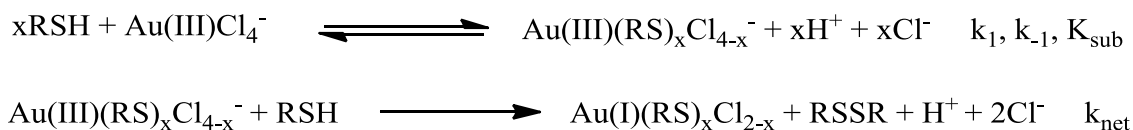


Figure 52: Determination of parameters a and b for the saturation kinetics rate law. The slope is $1/a$ and the intercept is b/a .

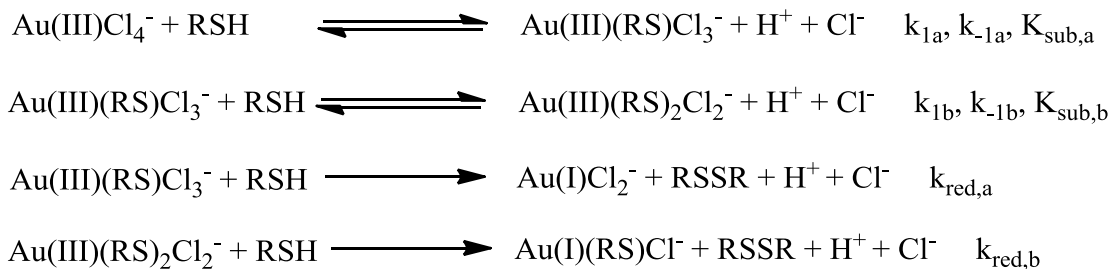
The linear equation determined that the parameters are $a = 0.162 \pm 0.005 \text{ M}^{-1} \text{ s}^{-1}$ and $b = 44.3 \pm 5.7 \text{ M}^{-1}$. This implies that the second order rate constant in the second order rate law, which is more closely followed at $b[RSH] < 1$, is $k_{2nd} = a = 0.162 \pm 0.005 \text{ M}^{-1} \text{ s}^{-1}$ and when $b[B] > 1$ then the first order rate law is more closely followed with $k_{Au(III)} = a/b = 3.66 \times 10^{-3} \pm 0.46 \text{ s}^{-1}$ at the given ionic strength in methanol.

Referring back to Table 12, it is apparent that the saturation kinetics rate law, equation 5-9, describes the data very accurately (on the basis of the % difference between the modeled and determined rates), with the exception of the reaction that was performed at the heaviest excess and highest concentration of RSH. This deviation is likely due to a second saturation point being reached, arising from the second equilibrium step, which is not accounted for in the rate law. A reaction scheme that can be associated with these observations, according to Wilkins,¹⁸⁰ is one where there are two consecutive reactions with one element of reversibility. For this reaction, that corresponds with Scheme 5-4.



Scheme 5-4: The Au(III)Cl₄⁻ tiopronin reaction viewed as a one exchange equilibrium, one reduction process.

Scheme 5-4 is a simplification of Scheme 5-5, which follows more closely the form of that proposed by Elding and coworkers.



Scheme 5-5: The two consecutive exchange equilibrium, two simultaneous reduction mechanism for Au(III)Cl₄⁻ and tiopronin.

Scheme 5-5 is difficult to evaluate because the determination of ligand exchange products is not possible with the current methodology as the UV-Visible spectrum of the exchanged products is not significantly different from the starting material. This scheme is, however, supported by the rate retardation upon initial addition of Cl^- or H^+ .

These Schemes are further supported by the fact that addition of Cl^- or H^+ reduces the rate of reaction. Examining the simplified Scheme 5-4, and using the following equations:

$$K_{sub} = \frac{[\text{Au(III)}(\text{RS})_x\text{Cl}_{4-x}]}{[\text{Au(III)}\text{Cl}_4][\text{RSH}]} = \frac{k_1}{k_{-1}} \quad (5-11)$$

$$\frac{d[\text{Au(I)}]}{dt} = k[\text{Au(III)}]_{total} = k_{red}[\text{Au(III)}] = \frac{k_{red}K_{sub}[\text{Au(III)}\text{Cl}_4][\text{RSH}]}{1 + K_{sub}[\text{RSH}]} \quad (5-12)$$

where K_{sub} is the substitution reaction equilibrium constant, $k = k_{\text{Au(III)}}$ for the pseudo first order process (not the 2/3 order process), k_1 is the substitution rate constant, k_{-1} is the dissociation rate constant, $[\text{Au(I)}]$ represents all produced Au(I) species and $[\text{Au(III)}]$ represents all Au(III) species, and k_{red} is the rate constant for the reduction of all Au(III) species to any Au(I) species, then equation 5-13 can be used to describe the system:

$$v = \frac{k_{red}K_{sub}[RSH][Au(III)]}{1 + K_{sub}[RSH]} \quad (5-13)$$

where $a = k_{red}K_{sub}$ and $b = K_{sub}$. This equation is of the form of 5-9, therefore, $k_{red} = 3.66 \pm 0.46 \times 10^{-3} \text{ s}^{-1}$ and $K_{sub} = 44.3 \text{ M}^{-1}$. The accuracy of this rate law (equation 5-9) in predicting the observed initial rates is displayed in Table 12. For all but the highest [RSH]:[Au(III)] (300:1), the model accurately predicted the initial rate within $\pm 10\%$. The error in the 300:1 experiment might suggest that a second saturation kinetics limit was reached, dictated by the second equilibrium in Scheme 5-5. Experiments are ongoing to reproduce these results across a large range of [RSH] in identical media (excess $[H^+]$, $[Cl^-]$, and μ). Studying the variation of initial rate with lower $[Cl^-]$ in order to determine equilibrium constants, such as Elding has done for the previously mentioned dimethyl sulfide and thiocyanate systems, is also desirable.^{169, 170}

Examination of the kinetics of the analogous bromide complex was also attempted. The reaction happens too fast at room temperature in methanol to accurately measure the initial rates ($t_{1/2} \ll 20\text{s}$, significant conversion occurs during the mixing of solutions). In one set of experiments, a negative reaction order with respect to gold was observed, but on the basis of the chloride experiments and given the speed of reaction, these results were disregarded. There is much speculation in the nanoparticle synthesis community that $AuBr_4^-$ would be a useful starting material for Brust type syntheses due to the decreased force constant of Br^- with respect to Cl^- making for a more labile Au(III) complex,¹⁸¹ and also because Br^- complexes are less susceptible to hydrolysis

reactions.¹⁸² Preliminary investigations have determined that Au(III)Br_4^- is reduced much faster by tiopronin than Au(III)Cl_4^- , and, furthermore, more readily goes to completion (100% conversion for Br^- as supposed to approximately 80% conversion for Cl^-). Differences in percent conversion were noted for our homemade HAuCl_4 trihydrate with the HAuCl_4 trihydrate purchased from Sigma-Aldrich. These differences could arise from either the presence of nitrates (originating from nitric acid used in the original synthesis) or catalytic amounts of iron or palladium contaminants (arising from novice students using metal spatulas or contaminated spatulas for retrieval of tetrachloroauric acid) oxidatively driving the final conversion of Au(I)(RSH)_2 to the polymeric or cyclic precursor material. Water content and excess acid should also be considered as possible sources of the differing behavior between the two samples.

In conclusion, a rate law that accurately describes the reaction at low $[\text{RSH}]:[\text{Au(III)}]$ (equation 5-6), and a rate law that describes the reaction fairly accurately across a larger range of $[\text{RSH}]:[\text{Au(III)}]$ (equation 5-9), were proposed. The latter rate law suggests that this reaction is mechanistically similar to the general Scheme proposed by Elding and coworkers for various substitution/reduction reactions of Au(III) complexes. In order to more completely support this mechanism, a thermodynamic study of this reaction would be necessary in order to observe whether the reduction proceeds via an inner-sphere or outer-sphere mechanism. If exchange must necessarily precede reduction, then one would expect changes in entropy consistent with an inner-sphere electron transfer. The development of a method to study the exchanged intermediates, $[\text{Au(III)(RS)}_x\text{Cl}_{4-x}]$,

both to prove their existence and to accurately determine equilibrium constants for the exchange processes (Scheme 5-5), would yield important data in the future.

In the near future, study of this system will continue to be pursued. It would be useful to set up collaboration with a research group in possession of a stop-flow instrument with temperature control in order to direct a proper kinetic evaluation with thermodynamic information. Going forward, it would be of great interest to marry these studies with studies of the polymer or cyclic complex growth, much like Hainfeld and coworkers did with the glutathione/Au(III)Cl₄⁻ system.¹⁷⁶ It is reasonably expectable that by systematically varying pre-reduction reaction time, temperature, and starting materials to control the exact composition of the precursor species could have effects on the size and surface structure of the final nanoparticle. These are experiments that could prove useful in explaining the previous work of the Murray research group where they varied Brust nanoparticle synthesis conditions to obtain different sized nanoparticles.⁶³

Acknowledgements

I would like to thank Dr. Kellen Harkness for his assistance with the background information, input on the kinetics experiments, and understanding of the reaction products. I would also like to acknowledge Andrzej Balinski for his assistance with the ongoing ¹H NMR kinetics experiments (not discussed here), and Matt Casey for verification of some of the preliminary observations discussed.

CHAPTER VI

SUMMARY OF CONCLUSIONS AND SUGGESTIONS FOR FUTURE WORK

Summary of Conclusions

As discussed in Chapter I, thiolate protected gold nanoparticles have gathered much interest in the past decade due to their ease of synthesis, ability to be functionalized, their biological interactions, and unique electronic, optical, and chemical properties. In the described research, we have utilized these properties to create functional nanomaterials with applications in biomimetics and nanomolecular electronics. Additionally, fundamental aspects of nanoparticle synthesis and characterization were studied.

A peptide functionalized tiopronin protected gold nanoparticle, with approximate average composition of $\text{Au}_{696}\text{Tiopronin}_{261}(\text{CSGSGNSELLSLINDMPITNDQKKLMSNN})_4$ was synthesized and found to strongly and specifically bind to the pharmaceutical monoclonal antibody Palivizumab in a quartz crystal microbalance immunoassay, as described in Chapters II and III. The strength of the binding, as determined by a kinetic concentration-dependent study ($K_d = 292 \pm 177$ nM) was competitive with a biomimetic peptide epitope scaffold which integrated the same linear peptide sequence ($K_d = 87$ nM)¹²⁵ This biomimetic nanomaterial may prove useful as a novel subunit vaccine for the prevention of human respiratory syncytial virus, pending *in vivo* analysis.

Alkanethiolate protected gold nanoparticles functionalized with molecular wire thiolate ligands were synthesized and evaluated using scanning electrochemical microscopy (see

Peterson et. al. 2006). Nanoparticles functionalized with wire molecules were found to exhibit faster electron transfer kinetics than unfunctionalized nanoparticles, described in Chapter IV. These “wired nanoparticles” might be useful in nanomolecular electronic devices.

For the case of water soluble tiopronin protected gold nanoparticles, which are useful in biological studies such as that presented in Chapter III, the complexation and reduction process preceding the final reduction step in their synthesis was studied, and a rate law was determined in Chapter V. In methanol/perchlorate solution, the reduction of tetrachloroauric acid trihydrate by tiopronin, as followed by UV-Visible spectroscopy, was found to follow saturation kinetics, consistent with a proposed mechanism where gold(III) is first complexed by one to two equivalents of tiopronin, followed by subsequent reduction by an additional equivalent of free tiopronin.

Additional accomplishments discussed include a comparative study of thermal gravimetric analysis and elemental analysis of thiolate protected gold nanoparticles (Appendix A), the synthesis and characterization of water soluble dendrimer-thiolate protected gold nanoparticles (Appendix B), and attempts at alternative synthetic routes to a molecular wire ligand (Appendix D).

In conclusion, a number number of studies with diverse applications were conducted which all utilized similar nanoparticle synthesis, functionalization, and characterization techniques. The studies underscore the versatility and potential applicability of these novel nanomaterials in a variety of areas, from materials to life sciences. Additionally,

new knowledge was gained on fundamental aspects of nanoparticle synthesis. The knowledge should prove useful in future attempts to exploit the underlying chemistry of nanoparticle synthesis in order to create more well-defined or completely novel nanomaterials.

Suggestions for Future Work

Biomimetic Nanoparticles

Many aspects of the biomimetic HRSV nanoparticle project elicit further investigation or methodological improvement. These aspects include peptide design, epitope mapping strategies, nanostructural considerations, mimic detection techniques, and in vivo evaluation for antigenicity. While some of these facets are currently under investigation for different systems, the HRSV biomimetic project is not currently active even though many avenues of research remain unexplored.

The rate limiting step to designing a useful peptide for conjugation to a nanoparticle had always been the lack of any crystal structure data for either the F protein, the antibody, any complex related to the two. Now that this data is available^{88-90, 125}, and given the results obtained in Chapter II, much more informed decisions about peptide design in the context of nanoparticle biomimetics should be forthcoming. Knowing the residues critical to Palivizumab-epitope binding and their spatial orientation should allow one to only select the most important parts of the primary sequence, or potentially add in discontinuous residues with an inert linker. As was indicated previously, the desired

orientations and lengths of the two alpha helical sections known to be important to the binding interaction should be evaluated in the ELISA assay. The specific effects of adding, removing, or replacing single amino acids would allow for the selection of the smallest, most efficient peptides to be used in nanoparticle studies as supposed to the 24 amino acid sequence (not including any added linker residues) found most successful in the current study. This might also add additional insight into the binding of the native proteins, further corroborating the previously mentioned crystal structure data.

While the current research discussed the importance of peptide structural modifications beyond primary sequence variation such N and C terminal modification and linker chemical structure and length with regards to optimizing peptide efficacy in biomimetic design, the data collected was not systematic. This was largely due to the desire to obtain a working mimic as a starting point. Having found this starting point, a systematic variation of peptide structure is now appropriate. The following systematic variations are prescribed: effect of C-terminal amination and N-terminal acetylation individually or in tandem versus unmodified termini for like primary sequences, directly comparing PEG spacers to inert amino acid spacers, and comparing chemically similar spaces of different lengths.

Once ideal peptides have been designed, a number of structural changes can be investigated with regards to the final nanomaterial. Nanoparticle core size, especially in the case of dual cysteine functionalized peptides, should have a significant effect. In the case of a single cysteine containing peptide, the core size could affect the secondary structure of the peptide by modifying the interactions between neighboring ligands. In

the case of a dual cysteine containing peptide, the core size is expected to have an effect on how far apart the cysteine residues space themselves (due to spacings between active sites and surface curvature versus the strain imparted to the peptide upon anchoring the cysteine thiol groups on the gold core), and, therefore, on the conformation of the formed peptide loop.¹¹⁰ Options for controlling the nanoparticle size are via synthetic conditions (for instance, ligand to metal ratio)⁶³ or by post-synthetic size separation.^{55, 183}

Another exciting possibility, especially for this specific case, is the concept of functionalizing a nanoparticle with two (or more) peptides to represent a discontinuous epitope, suggested by Rutledge and coworkers.⁹² In the Palivizumab epitope, one should recall that the interacting residues are located on two alpha helices separated by an amorphous loop region, and a further residue on an entirely different region of the peptide. If both helices are separately synthesized, and potentially a third peptide is synthesized with the other interacting residue, and they are subsequently place exchanged onto an appropriate sized nanoparticle, then the interacting residues could be placed at the appropriate spatial coordinates without the need for non-interacting amino acids.

Finally, it would be prudent to evaluate this system with different methodologies. In the context of the QCM, different antibody immobilization strategies should be evaluated, as spacing of antibodies in an immunoassay is critical in optimizing sensitivity.¹²⁸ Also, QCM with dissipation measurement should provide additional information as to whether the binding is rigid, as would be expected for an antigen-antibody interaction.¹⁸⁴ An instrument suited to this task is available from Q-Sense which also is equipped with an autosampler. As manual QCM experiments are time intensive (typically 2 hours) and

subject to errors during sample change which lead to useless data sets, such as the introduction of air bubbles or pressure changes across the crystal face, a higher data yield might be attained with such an instrument. Another consideration should be the validation of the QCM results with an additional analytical method such as ELISA or SPR.

Wired Nanoparticles

Currently, Dave Crisostomo is continuing with the research in wired nanoparticles. As with the biomimetic nanoparticle project, a great deal of systematic changes should lead to important insights on structure-function relationship. Currently, the research is focused on observing whether or not electron transfer kinetics of nanoparticles protected by alkanethiolate ligands of different lengths (for instance, hexanethiol versus octanethiol) are similarly affected by the introduction of a molecular wire ligand. Another interesting question is how the nanoparticle core size might affect electron transfer or the ability of the molecular wire ligands to modulate the electron transfer. It is possible that a change in surface curvature could have a significant effect on the ability of the core itself to come in close proximity of an electrode surface. It might also effect the chemical environment of the molecular wire ligand itself.

Upon successful completion of these fundamental studies, integration of the “wired” nanomaterials into functional nanomolecular electronic devices is of great interest. An idea proposed by David Cliffel is to integrate wired particles with Photosystem I (PSI).

In this context, the nanoparticles could store charge from photocurrent generated by covalently attached PSI which could later be discharged to a quantum dot to produce light. The whole device is comparable to a nanoscale, battery-powered flashlight with wired nanoparticle capacitors.

Nanoparticle Precursor Formation

While the determined rate law for gold(III) chloride reduction by tiopronin in methanol accurately fit the data over a sufficient concentration range (much greater than typical synthetic conditions)¹²², collection of more data points to verify the saturation kinetics data is crucial. Simply put, more data points are needed to prove the non-linear relationship at higher tiopronin concentrations. Verification of this rate law is crucial to suggesting a mechanism for tiopronin gold nanoparticle precursor formation. In order to measure the initial pre-reduction ligand exchange process, a spectrophotometer with a stop-flow system is required. Such an experimental set-up would also allow us to interrogate the initial rates of reduction in the bromide system.

APPENDIX A

THERMAL GRAVIMETRY-MASS SPECTROMETRY AND ELEMENTAL
ANALYSIS OF TIOPRONIN PROTECTED GOLD NANOPARTICLES

This research was conducted at the Center for Nanophase Materials Sciences, which is sponsored at Oak Ridge National Laboratory by the Division of Scientific User Facilities, U.S. Department of Energy. This research was authorized upon successful submission and review of a rapid access proposal, ID CNMS2007-R19. The experiments were held at the Macromolecular Complex Systems Group under the supervision of Dr. Joseph Pickel.

Introduction

Thermal gravimetric analysis is the easiest route to determining the percent organic composition of gold nanoparticles. There has been debate about the identity of the burnoff material, and often times the average approximate molecular formulas determined for certain preparations are not reasonable with the current picture of how a nanoparticle should look. Therefore, it was endeavored to characterize the thermal gravimetric plot with mass spectrometry. The technique is occasionally referred to as temperature programmed desorption mass spectrometry (TPD-MS).

Methods

Synthesis of Au₂₁₆Tiopronin₁₂₉

Tiopronin MPCs were synthesized as previously described.¹²² 5.25 g (15.4 mmol) HAuCl₄ · 3H₂O was dissolved in 500 mL 6:1 methanol:acetic acid and chilled in an ice bath for 30 minutes, giving a yellow solution. 7.56 g (46.2 mmol) tiopronin was then added to the solution, forming a ruby red intermediate. Upon dissolution of the tiopronin, 5.84 g (154 mmol) sodium borohydride in approximately 10 mL water was immediately and rapidly added to the mixture. A violent, exothermic reaction results, leaving a black solution. The solution is stirred overnight, yielding polydisperse nanometer sized clusters. The resulting solution is rotary evaporated *in vacuo* to remove the methanol. The resulting precipitate/viscous acetic acid solution is redissolved in water, pH adjusted to 1 with concentrated hydrochloric acid and placed in dialysis tubing (cellulose ester, MWCO = 10 kDa). The dialysis proceeds for 2 weeks changing the water at least twice daily until the water does visually turn a color. ¹H NMR: 4.00 ppm broad singlet (tiopronin methylene on cluster), 3.76 ppm broad singlet (tiopronin CH on cluster), 1.66 ppm very broad singlet (tiopronin methyl on cluster). TEM: average particle diameter of 2.2 nm ± 0.6 nm. UV/Visible spectroscopy: no surface plasmon resonance band observable. TGA: 33.134 weight percent organic (tiopronin). Average formula: Au_{216±7}Tiopronin_{129±4}.

Synthesis of Hexanethiol Monolayer Protected Clusters

1.5 g of tetraoctylammonium bromide (a phase transfer agent) was dissolved in 80 mL of toluene. 0.31 g of HAuCl_4 was dissolved in 25 mL of water. To the vigorously stirring tetraoctylammonium bromide solution, the gold solution was added slowly. The resulting orange gold-containing organic phase was isolated and chilled in an ice bath for 30 minutes and stirred vigorously. 0.38 g of NaBH_4 was dissolved in 25 mL of water. To the stirring organic solution, 260 μL of 1-hexanethiol was added. Immediately, the NaBH_4 solution was added over a period of 10 seconds. The resulting black solution was stirred for 30 minutes on ice, and then additionally overnight at room temperature. The organic phase was isolated and rotary evaporated to yield a black solid. The solid was dissolved in a minimum of toluene and precipitated in 400 mL of ethanol at $-20\text{ }^\circ\text{C}$ overnight. The precipitate was collected on a fine glass frit and washed with ethanol and acetone. Additional purification was accomplished by sonicating in acetonitrile for 15 minutes, and again collecting on a glass frit and washing with ethanol and acetone. ^1H NMR: 2.17 ppm, 1.45 ppm, 0.98 ppm broad peaks. TEM: $2.8\text{ nm} \pm 0.9\text{ nm}$ diameter. UV/Vis: slight surface plasmon band observed at 520 nm. TGA: 20.367 weight percent organic. Average molecular formula: $\text{Au}_{448}\text{Hexanethiol}_{192}$.

Thermal Gravimetric-Mass Spectrometric Analysis

TGA with mass spectrometric analysis of the evolved gases was accomplished using a TA Instruments 2950TGA equipped with Pfeiffer ThermoStar Mass spectrometer. Both ion selective trend scans and scanning bar graph scans were completed. The purge gas was argon, and the temperature was ramped from room temperature up to 1000 °C.

Elemental Analysis

Samples were sent to Columbia Analytical Services for analysis of carbon, hydrogen, nitrogen, sulfur, oxygen, gold, and sodium. Carbon, hydrogen, and nitrogen were analyzed by combustion with a WO₃ catalyst, and detection by TC and IR. Sulfur was analyzed by combustion with IR detection. Oxygen was analyzed by pyrolysis with IR detection. Sodium and gold were measured either by ICP-OES, ICP-MS, or AAS.

Results and Discussion

Thermogravimetric Analysis

Thermogravimetric analysis for AuTiopronin and AuHexanethiol were compared qualitatively, as in Figure 53.

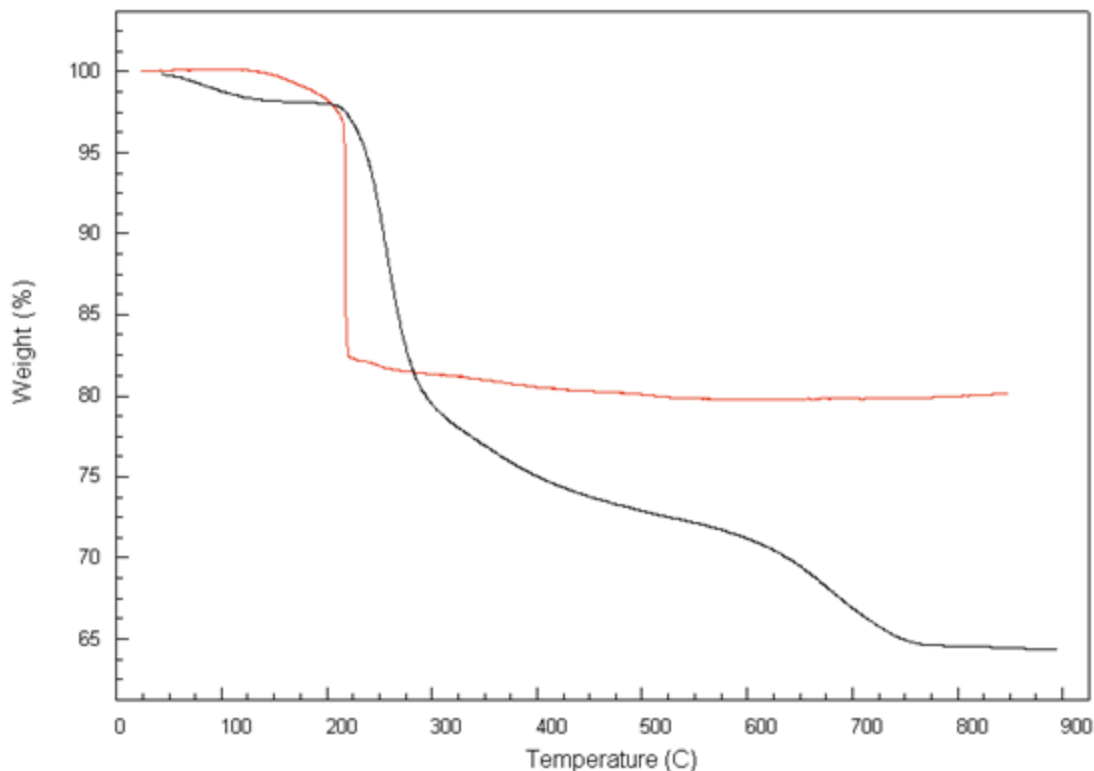


Figure 53: Thermogravimetric profiles of gold hexanethiol cluster (red) and gold tiopronin cluster (black). Differences in the total magnitude of percent weight loss may be due to size dependent properties, but the step-wise nature of the tiopronin cluster weight loss is characteristic of polar MPCs

Whereas alkanethiol nanoparticles have a single mass loss step when heated under nitrogen, tiopronin nanoparticles exhibit two. The shape of the curve is identical for thermal analysis of tiopronin ligand, although the temperature of each step is shifted slightly to lower temperature. The assumption had always been that any thermal loss should be attributed strictly to loss of organic material, which made theoretical sense with what was understood about thiolate gold nanoparticles if composition calculations used burn off data up to 550 °C. Once spectrum were run up to 800 °C, however, composition

calculations yielded thiols in excess of hypothesized surface gold atoms, which was inconsistent with expected compositions.

Elemental Analysis

The results of elemental analysis in terms of calculated molecular composition compared to results obtained with a combination of TGA and TEM by two different calculations are compared in Table 13.

Table 13: Elemental analysis-calculation compared to two different TGA-TEM calculations of molecular formula. Found represents the found percentages from elemental analysis. Expected are the percentages anticipated from the TGA-TEM calculations. Errors are given for each individual element and for the totals percentages expected for tiopronin and inorganic material (sodium was factored in to investigate whether the final solids are heavily sodiated at the carboxylate groups despite the acidification pre-dialysis).

<i>calculated formula</i>	$\text{Au}_{216}(\text{C}_5\text{H}_9\text{NO}_3\text{S})_{146}$	$\text{Au}_{216}(\text{C}_5\text{H}_9\text{NO}_3\text{S})_{129}$			$\text{Au}_{216}(\text{C}_5\text{H}_9\text{NO}_3\text{S})_{68}$		
%	<i>found</i>	<i>expected</i>	<i>error</i>	<i>error_{net}</i>	<i>expected</i>	<i>error</i>	<i>error_{net}</i>
C	13.5	12.2	-10.7%	-8.12%	7.61	-77.4%	-73.1%
H	1.65	1.84	10.3%		1.15	-43.5%	
N	3.04	2.84	-7.04%		1.78	-70.8%	
S	6.82	6.50	-4.92%		4.07	-67.6%	
O	10.8	9.74	-10.9%		6.08	-77.6%	
Na	0.25	0.00	-	1.72%	0.00	-	17.1%
Au	65.5	66.9	2.09%		79.3	17.4%	
<i>total %</i>	102	100	-1.54%	-6.40%	100	-1.57%	-56.0%

The formula $\text{Au}_{216}(\text{C}_5\text{H}_9\text{NO}_3\text{S})_{146}$ was obtained from direct calculation of elemental analysis results and TEM core size calculations. $\text{Au}_{216}(\text{C}_5\text{H}_9\text{NO}_3\text{S})_{129}$ was obtained from a combination of TGA and TEM assuming that all loss was attributed to tiopronin, and

$\text{Au}_{216}(\text{C}_5\text{H}_9\text{NO}_3\text{S})_{68}$ was calculated in the same way, except that it was assumed that the loss was due to a loss of AuTiopronin_2 staple complexes from the surface. If it is assumed that the elemental analysis gives a true total tiopronin loss, then the conclusion is that the all tiopronin calculation from TGA underestimates the tiopronin thiolate content by 8.12% while the staple calculation underestimates the content by 73.1%. Therefore, given the assumption, the all tiopronin loss method is more accurate than the staple calculation. Consequently, it is not expected that Au atoms are lost from the sample during thermal analysis. The underestimation could originate from ashing of the ligand on the pan, resulting in residual elemental carbon that was not factored into the total organic mass. Ashing was expected from visual inspection of burned material. When the TGA was only run up to 550 °C, the residual material in the pan was black. Running the TGA up to 800 °C or higher resulted in what appeared to be purely solid gold flakes, consistent with a complete loss of organic matter. In order to confirm the identity of the burn off during this final step, TPD-MS was used.

TPD-MS of Tiopronin Gold Nanoparticles

Therefore, TPD-MS was used to study the identity of the burn off material. A TGA from the TPD-MS instrument is provided for comparison in Figure 54.

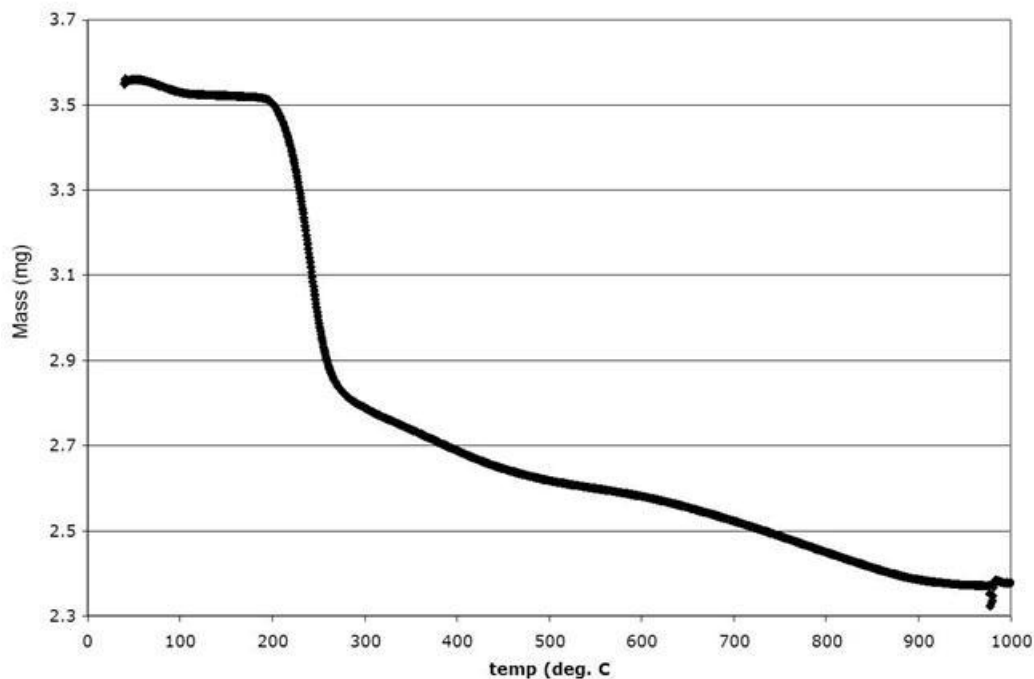


Figure 54: Thermal gravimetric spectrum generated on the TG-MS instrument at Oakridge, under Argon purge.

The magnitude of each loss is identical between the two analyses, but the shape of the final loss is different. The difference in thermal gravimetric plot shape was likely due to an argon purge in the Oak Ridge instrument as supposed to a nitrogen purge with the VINSE instrument. M/z of the burn off compound tracked with temperature is displayed in Figure 57, preceded by burn off for AuHexanethiol in Figure 55 and 56 for comparison.

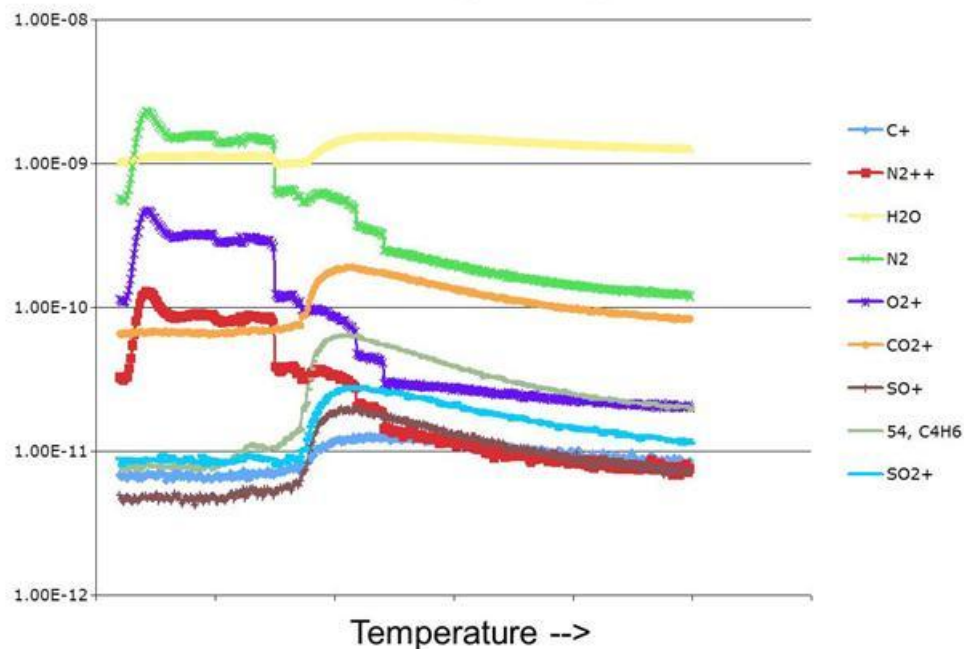


Figure 55: Selective ion scan of elemental and small molecule fragments thermally lost from AuHexanethiol nanoparticles. The y-axis is total ion current at the selected m/z.

Small room-temperature gas molecules are the easiest to observe in this technique.

Notice how molecules or atoms associated with carbon and sulfur from hexanethiol spike at the beginning of the mass loss (Figure 53) and slowly taper off. Total quantitative measurements of these ions are hampered by their natural presence in the chamber due to < 100% purging efficiency.

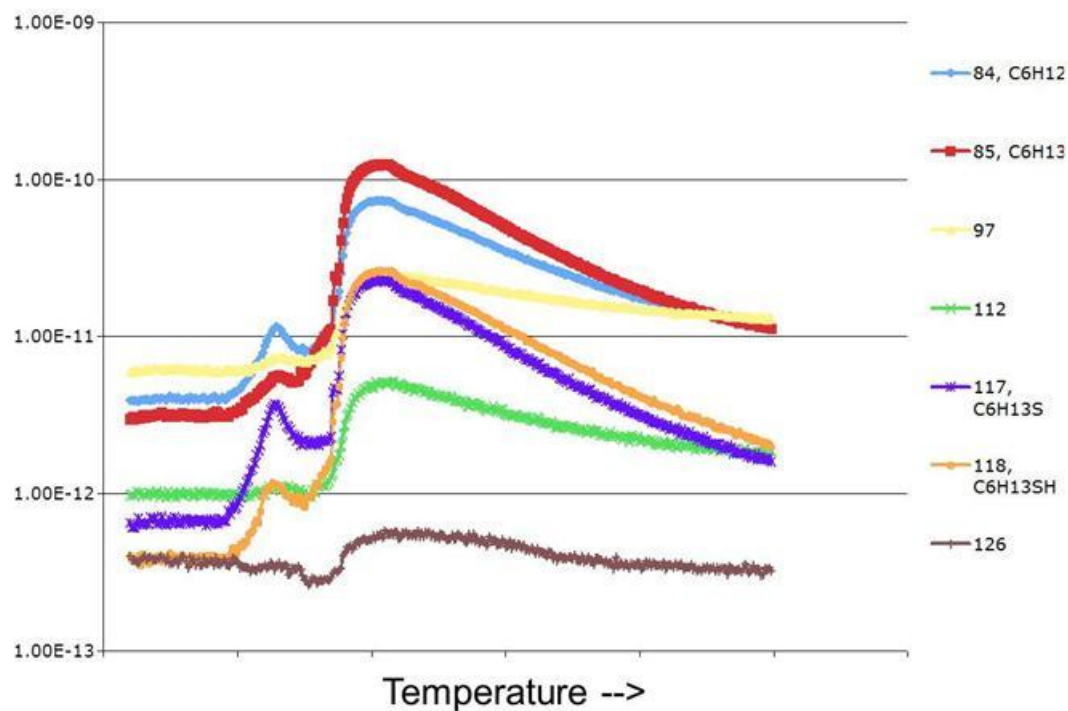


Figure 56: Larger mass peaks thermally lost from AuHexanethiol nanoparticles. The y-axis is total ion current at the selected m/z , listed at right, in Da, with some m/z identified.

Larger mass fragments were identifiable for this sample, including the intact ligand and some fragments thereof, noted in the key (charges on the ions not shown). Some larger mass fragments could be identified for the AuTiopronin sample, but identification of the ions was not consistent with expectations (see Figure 55). Therefore, only the small mass ions under oxidative (air) conditions are presented.

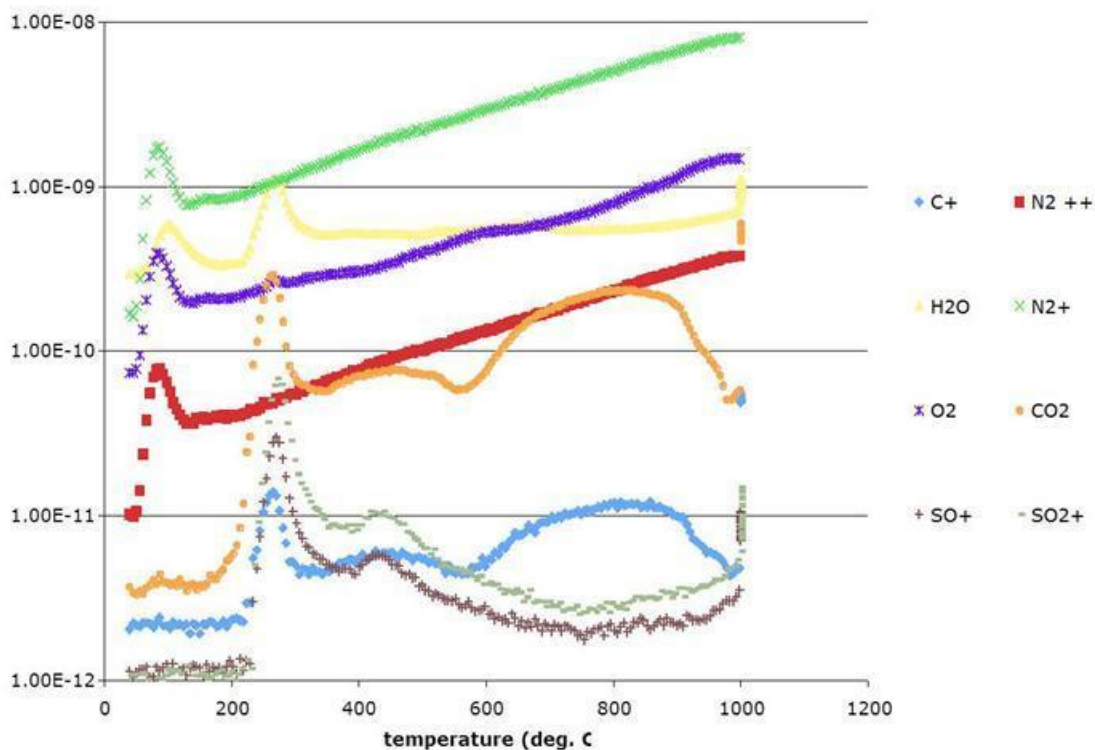


Figure 57: Small mass fragments thermally lost from AuTiopronin nanoparticles. The y-axis is total ion current at the selected m/z. This particular experiment was run in air instead of argon.

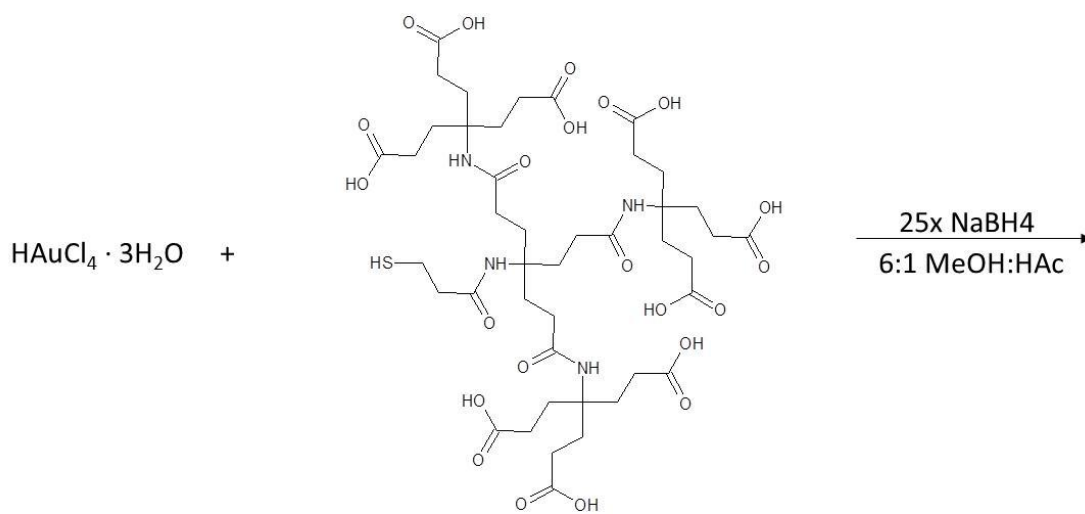
For tiopronin, only small molecule masses were identifiable. The loss that spans 600 to 1000 °C tracks directly with carbon, supporting the idea that tiopronin ashes during the burning process. This attributed to the carboxylate group, as molecules with carboxylate groups tend to have additional high temperature losses (as was observed with tiopronin and glutathione ligands without gold). The hypothesized chemistry of this process, consistent with the observations, might be $\text{RCOOH} \rightarrow \text{RH} + \text{CO}_2$, $\text{CO}_2 \rightarrow \text{O}_2 + \text{C}_{(s)}$, $\text{C}_{(s)} + \text{O}_2$.

APPENDIX B

SYNTHESIS AND CHARACTERIZATION OF WATER SOLUBLE DENDRIMER PROTECTED GOLD NANOPARTICLES

Introduction

The aim was to prove that carboxylate terminated G1 dendrimers could be used to synthesize gold nanoparticle cored dendrimers (NCDs) by Brust-like methodology. Here, to the best of our knowledge at the time of the study, the first example of a water soluble NCD is presented. The following reaction was studied, in Scheme B-1.



Scheme B-1: Synthesis of gold nanoparticle cored dendrimers (AuNCD)

Methods

Synthesis of (Au_x(G1S)_y)

Au_xG1SH_y was synthesized using a modified Brust reaction.¹ A solution of HAuCl₄ · 3H₂O in 5 mL of 6:1 methanol:acetic acid was cooled to -70° C in a dry ice/acetone bath. To this cold solution was added 60 mg of AuG1SH in 3.5 mL 6:1 methanol:acetic acid. Upon allowing the solution to slowly warm to -30° C, the solution turned from yellow to a light brown-orange, indicating the formation of a Au(III)-G1SH complex. To this solution was rapidly added a 25x molar excess (50 mg) of NaBH₄ in 1 mL of deionized water. CAUTION! A violent exothermic reaction results from the reduction of Au(III) to Au⁰. Upon reduction a black precipitate formed and was allowed to stir for 15 hrs. The solvent was removed by rotary evaporation, and the resulting black solid was resuspended in 0.5M NaOH. Purification was accomplished by dialysis in 10,000 MWCO tubing with MeOH:0.5M NaOH/H₂O. Dialysis proceeded for 5 days, with changes 4x daily. NMR: Consistent with the ligand, desensitization of protons that would be closest to the gold core, consistent with other ligands on gold (Figure 58). UV/Vis: No resulting SPR band. TEM: average diameter 1.3 ± 0.6 nm (Figure 59). TGA analysis was obscured by the presence of salt, but was measured as 60.2% organic. Average formula Au₁₈₆G1S₅₀.

Place Exchange

G1SH was stirred with AuTiopronin nanoparticles in 50:50 MeOH:H₂O (20 mg nanoparticle in 4 mL solvent, 30:1 G1SH:tiopronin feed ratio). ¹H NMR is displayed in Figure 60. Quantification was not possible due to solvent peaks.

Results

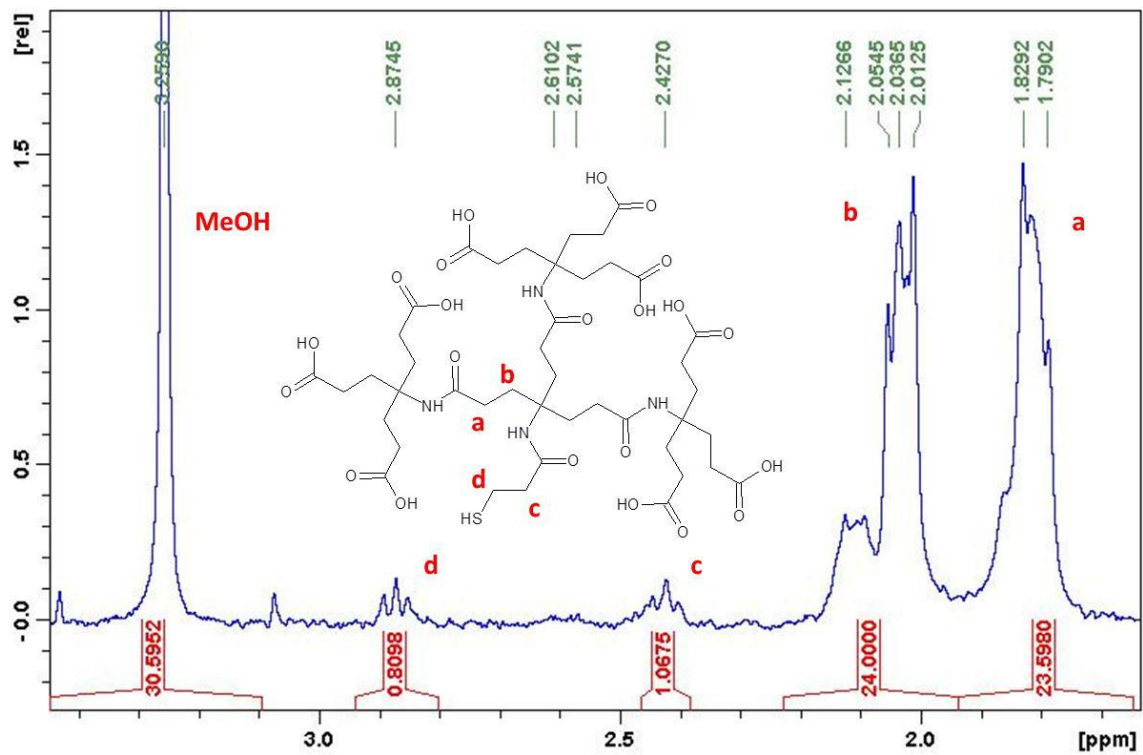


Figure 58: ^1H NMR of G1 dendrimer protecting a gold nanoparticle

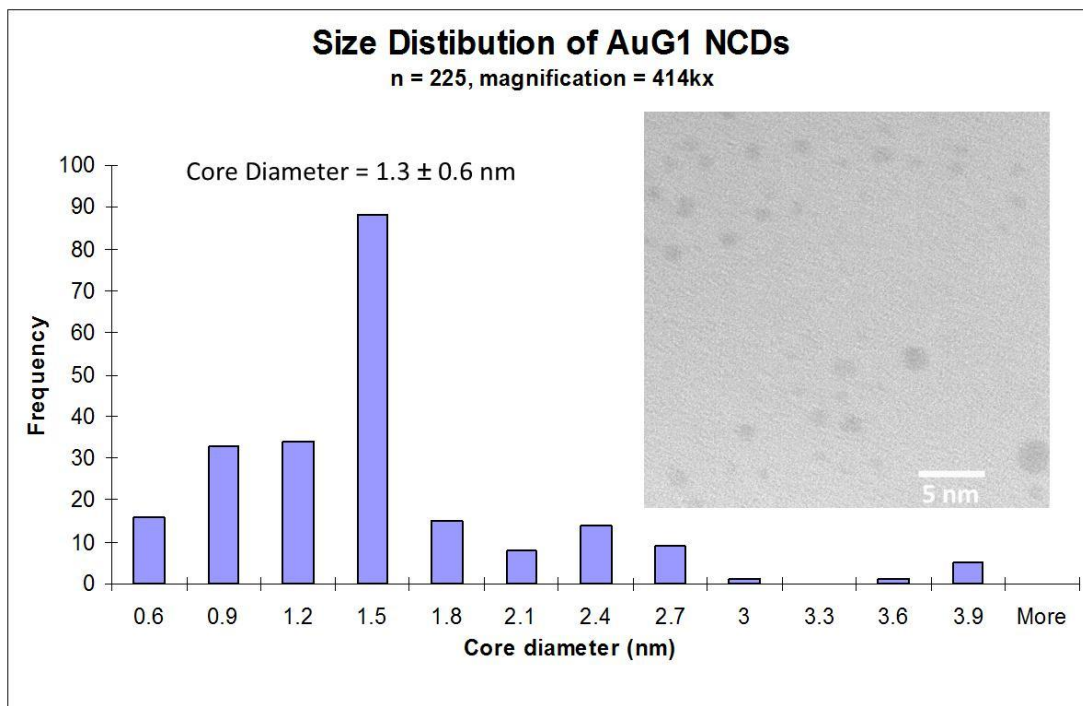


Figure 59: TEM micrograph and size distribution of AuG1S NCDs.

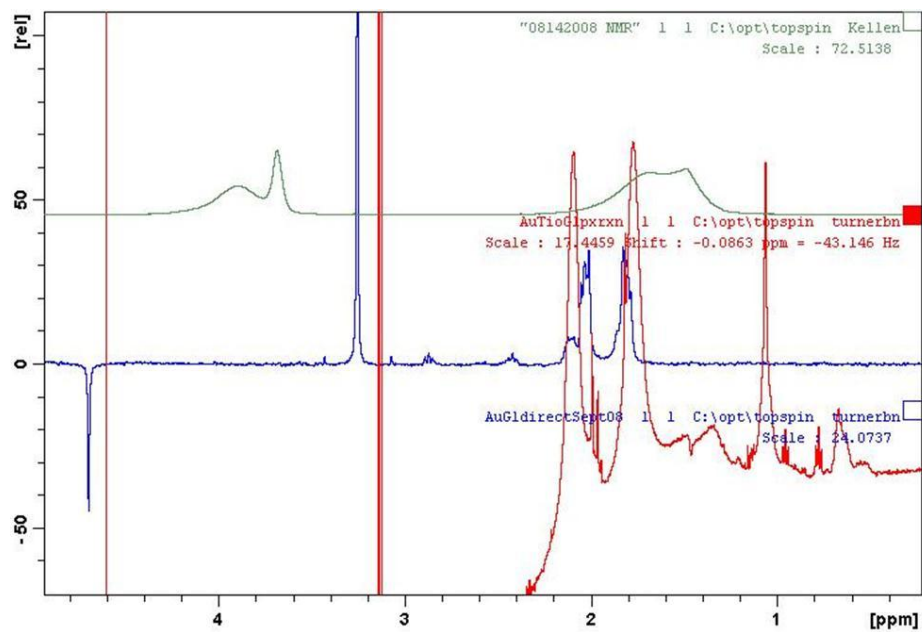


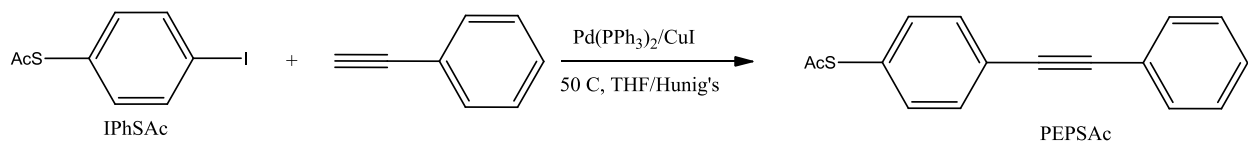
Figure 60: ^1H NMR data G1 place exchanged onto AuTiopronin. Green spectrum (top) is gold tiopronin nanoparticles, blue spectrum (middle) is G1SH, and red spectrum (bottom) is the place exchanged product.

APPENDIX C

SYNTHETIC ROUTES TO P-MERCAPTOPHENYLETHYNYLBENZENE

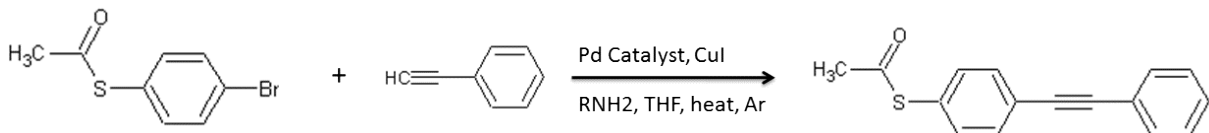
Methods

Standard Route to p-thioacetylphenylethynylbenzene (PEPSAc)¹⁵⁷



This route was not practical in the current research, as the starting material (4-iodophenylthioacetate) was not commercially available. Therefore, the following syntheses were pursued before turning to the commercially available PEPEPSAc.

Other routes to PEPSAc



*Synthesis of PEPSAc Through a Solvent Free, Copper Free Sonogashira Coupling*¹⁸⁵

0.5g BrPhSAc (2.16 mmol), 0.045g PdCl₂(PPh₃)₂ (3 mol %), and 2.05 g TBAF (6.5 mmol) were weighed into a 3 neck flask and purged with Ar. 290 μL of phenylacetylene (2.6 mmol) was added via syringe. The reaction mixture was heated to 80 °C in an oil bath and moderately stirred for 18 hours. The product was extracted in ether, washed 3x with water, dried over MgSO₄, filtered, and evaporated. The product was further purified on a silica gel column with DCM/hexanes. The reaction yielded 0.49 g of a yellowish solid. ¹H NMR: Product appeared to be deprotected disulfide, but coupled to phenylacetylene. The next reaction was chosen in order to work at a lower temperature so that disulfide formation might be avoided.

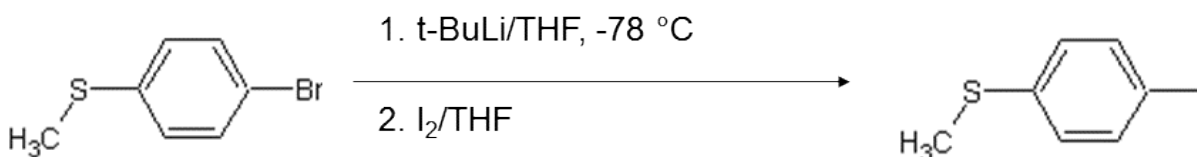
*Synthesis of PEPSAc Through a Copper Free, Amine Free Sonogashira Coupling*¹⁸⁶

0.5g BrPhSAc (2.16 mmol), 0.045g Pd₂(dba)₃ (0.5 mol %), and 0.82 g TBAF (2.6 mmol), and 11.3 g of PPh₃ (2 mol%) were weighed into a 3 neck flask and purged with Ar. 6 mL of anhydrous THF was added via syringe. 290 μL of phenylacetylene (2.6 mmol) was added via syringe. The reaction mixture was moderately stirred for 24 hours at room temperature. The product was extracted in ether, washed 3x with water, dried over MgSO₄, filtered, and evaporated. The product was further purified on a silica gel column with DCM/hexanes. The reaction yielded 0.54 g of a yellow oil. The correct product did not seem to be formed. The next reaction was chosen to work at an intermediate temperature, and to follow more closely the original Sonogashira reaction.

*Synthesis of PEPSAc Through a Standard Sonogashira Coupling*¹⁸⁷

0.5g BrPhSAc (2.16 mmol), 0.027g PdCl₂(PPh₃)₂ (0.039 mmol), and 0.023 g CuI (0.119 mmol) were weighed into a 3 neck flask and purged with Ar. 3 mL of anhydrous THF and 3 mL of anhydrous Hunig's base was added via syringe. 290 μ L of phenylacetylene (2.6 mmol) was added via syringe. The reaction mixture was heated to 50 °C in an oil bath and moderately stirred for 24 hours. The product was extracted in ether, washed 3x with water, dried over MgSO₄, filtered, and evaporated. The product was further purified on a silica gel column with DCM/hexanes. An orange solid was obtained. ¹H NMR: 7.55ppm, 7.36ppm, and 7.29 ppm, m, 9H (aromatic); 2.42 ppm, s, 3H (thioacetate methyl group). Yield: 42%, questionable purity.

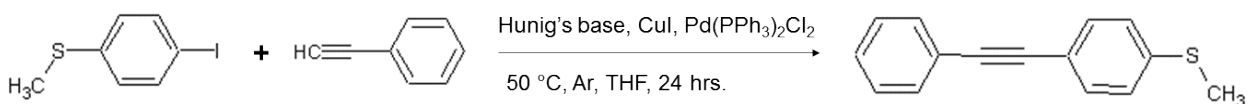
*Iodine Exchange with p-bromothioanisole (BrPhSCH₃)*¹⁸⁸



An amount of 1.0g of BrPhSCH₃ (4.92 mmol) was weighed into a 3 neck flask and purged with Ar. The solid was dissolved in 30 mL anhydrous THF, added via syringe. This solution was cooled in a dry ice/acetone bath. 5.8 mL of 1.7 M *tert*-butyllithium in

heptanes was added. CAUTION: *tert*-butyllithium should be handled with extreme caution as it readily acts with air and water in an extremely exothermic reaction capable of producing large flames. This solution was stirred for 5 minutes. 1.37 g iodine (5.42 mmol) was dissolved in 15 mL anhydrous THF. The iodine solution was added to the organolithium reagent via cannula. The reaction was brought to room temperature and stirred for about 30 minutes. The reaction was quenched with 20 mL of 1M HCl, and 2 moderate scoops of sodium sulfite. The solution was evaporated, and 20 mL of water was added. The organic product was extracted into ether and washed 3x with water. Recrystallization from hot iso-octane/toluene yielded a blue-green crystalline product. ¹H NMR matches literature values.

Synthesis of p-thiomethylphenylethylnylbenzene (PEPSCH₃) via Songoashira Coupling of IPhSCH₃¹⁵⁷



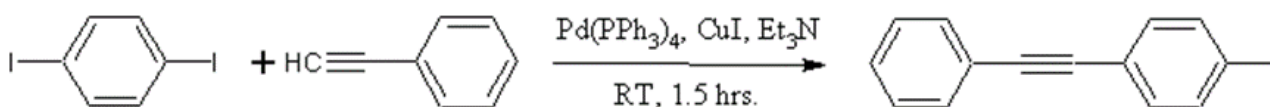
0.3 g of IPhSCH₃ from the previous reaction (1.27 mmol) and 0.010 g CuI (1.8 mol%) were weighed into a 3 neck flask and purged with Ar. 5.5 mL THF, 5.5 mL Hunig's base, and 522 μL of phenylacetylene were added via syringe. Then, 48.6 mg (0.6 mol %) PdCl₂(PPh₃)₂ was quickly added, and the solution purged. The solution was heated to 50 °C in an oil bath and stirred overnight. The product was extracted in ether, washed 3x with water, dried over MgSO₄, filtered, and evaporated. Recrystallization from hot

hexanes yielded an orange solid. ¹H NMR: 7.5 ppm, m, 2H; 7.42 ppm, d, 2H, J = 8.52 Hz; 7.32 ppm, m, 3H; 7.19 ppm, d, J = 8.52 Hz (aromatic); 2.48 ppm, s, 3H (thiomethyl). GC/MS M⁺ = 224.3 Da observed, pure product. Deprotection of this product proved impractical by the methods of Young, Gauthier, and Coombs, and also by NaH reaction.

Route from p-iodophenylethynylbenzene (PEPI) to

p-triisopropylsilylphenylethynylbenzene (PEPSSiTIP)

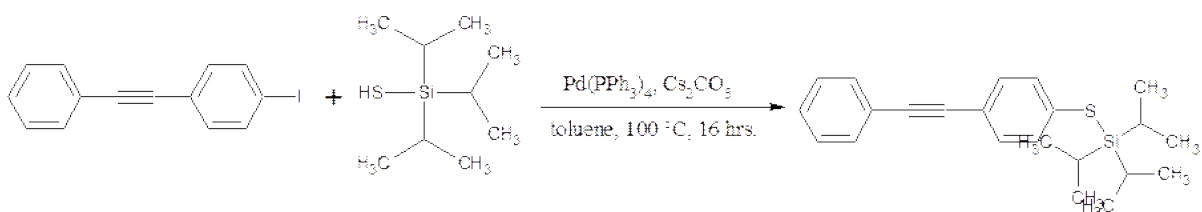
Synthesis of PEPI via Sonogashira Coupling of Diiodobenzene¹⁸⁹



Triethylamine was distilled over CaH₂ under Ar. 1 g diiodobenzene (3.0 mmol), 28.3 mg PPh₃ (0.1 mmol), and 8 mg CuI (10 mol%) were added to 180 mL of freshly distilled triethylamine. Then, 12.4 mg Pd₂dba₃ (5 mol%) was quickly added. 100 μL of phenylacetylene was added (1.0 mmol). The solution was stirred under Ar for 1.5 hours, the filtered, and evaporated. The yellowish solid was the dissolved in dichloromethane and poured over an excess of silica gel. The dichloromethane was then removed *in vacuo*, and the dry silica gel with the product absorbed onto it is loaded on top of a silica gel column. Chromatography yields high purity crystals of diiodobenzene in hexanes, and high purity PEPI. Yield 78% white flaky solid. ¹H NMR: 7.69 ppm, d, 2H, J = 8.52

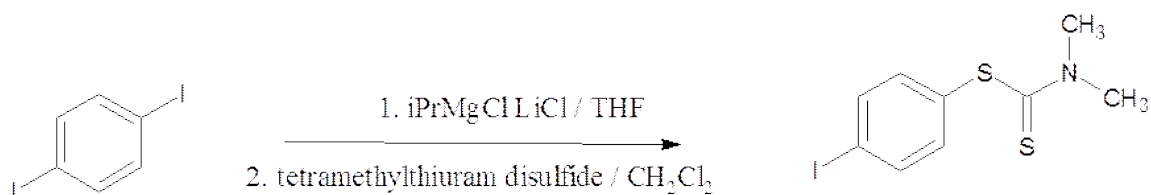
Hz; 7.53 ppm, 2H, m; 7.36 ppm, m, 3H; 7.26 ppm, d, 2H, J = 8.52 Hz, values match literature value.

Synthesis of PEPSSi TIP from PEPI¹⁹⁰



0.9 g of PEPI from the previous reaction (2.96 mmol), 200 mg $\text{Pd}(\text{PPh}_3)_4$ (5.8 mol %), 212 mg CsCO_3 (3.69 mmol) were dissolved in 30 mL of toluene, previously dried over molecular sieves, and purged with Ar. 850 μL of TIPSiSH (3.83 mmol) was added via syringe. The mixture was brought to $100\text{ }^\circ\text{C}$ in an oil bath and stirred for 18 hours. Afterwards, 30 mL saturated NH_4Cl was added, and the aqueous solution was extracted twice with diethyl ether. The organic fractions were washed 3 times with water, and evaporated to yield a red oil with red/orange precipitate. Residual solvent was removed with heating *in vacuo*. The product was extracted into hexanes. ^1H NMR: 7.54 ppm, m and 7.50 ppm, d, total 4H; 7.40 ppm, d, and 7.35 ppm, m, total 5H (aromatic); 1.12 ppm, m, 21H (triisopropyl silane protons). Crude product could not be further purified on a column as the product decomposed. Recrystallization strategies were not very successful.

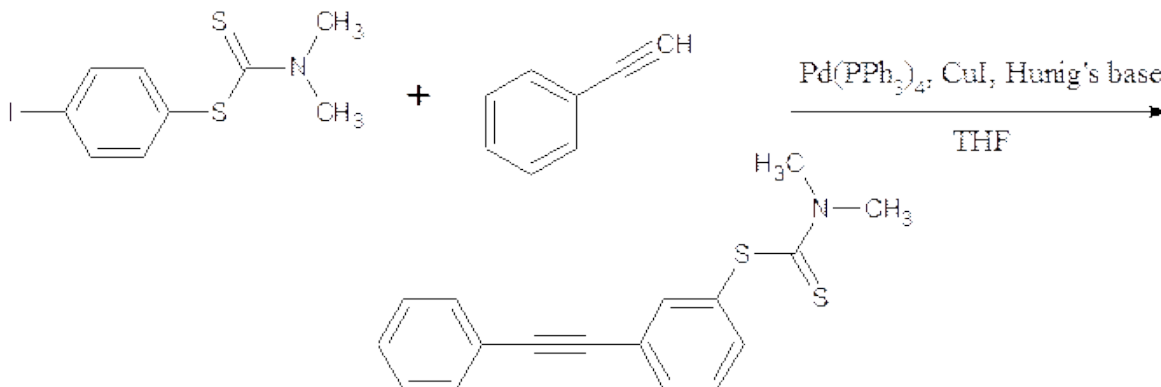
*Synthesis of p-iodotetramethylthiurylbenzene (IPhSTMT)*¹⁹¹



An amount of 1.0 g diiodobenzene (3.0 mmol) was weighed into a 3 neck flask and purged with Ar. 6 mL of freshly distilled THF was added. The solution was chilled in an ice bath. 3.54 mL of 0.9M (as determined by iodine titration) $i\text{PrMgCl-LiCl}$ solution was added. CAUTION: The Grignard reagent will react exothermically with air and water. The solution was allowed to warm to RT. 0.80 g of tetramethylthiuram disulfide was dissolved in 10 mL of freshly distilled dichloromethane and purged with Ar. The Grignard solution was, again, cooled in an ice bath, and the thiuram solution was added cautiously. The solution was filtered, evaporated, and eluted on a silica gel column with DCM/hexanes. $^1\text{H NMR}$ 7.78 ppm, d, 2H, $J = 8.44$ Hz (aromatic close to iodine); 7.19 ppm, d, 2H, $J = 8.44$ Hz (aromatic close to thiuram); 3.57 ppm, s, 3H, thiuram methyl a); 3.50 ppm, s, 3H, (thiuram methyl b).

Synthesis of p-tetramethylthiurylphenylethynylbenzene (PEPSTMT) via Sonogashira

Cross-Coupling of IPhSTMT



0.47 g IPhSTMT from the previous synthesis (1.55 mmol), 121 mg Pd(PPh₃)₄ (10 mol%), and 29 mg CuI (10 mol %) were dissolved in freshly distilled Hunig's base (9mL) and THF (4mL), and purged with argon. 186 μ L of phenylacetylene was syringed in, and the reaction was stirred for 24 hours at 100 °C. The product was extracted in ether, washed 3x with water, dried over MgSO₄, filtered, and evaporated. The product was further purified on a silica gel column with DCM/hexanes. ¹H NMR: 7.73 ppm, m, 4H; 7.49 ppm, m, 5H (aromatic); 3.56 ppm, s, 3H (first thiuram methyl); 3.35 ppm, s, 3H (second thiuram methyl). Reaction worked extremely well, but was irreproducible in later trials. This was attributed this to humidity, as every repeat was performed in the summer, and a Schlenk line was not utilized (only argon balloons).

Deprotection of PEPSTMT to p-mercaptophenylethynylbenzene (PEPSH)

The product above was deprotected by NaOH (24 mg), Zn (3 mg), H₂O 1.8 mL, THF (3 mL) and stirring for 3 hours, followed by quenching and acidifying with HCl. A greenish, semi-crystallin solid was obtained and recrystallized once from iso-octane. ¹H NMR 7.71 ppm, m, 2H; 7.59 ppm, m, 2H; 7.51 ppm, m, 3H; 7.07 ppm, m, 2H (aromatic); 2.34 ppm, bs, 1H (thiol). Thiuram-like byproduct present, 3.62 ppm, bs, 6H (in thiuram it is at 3.60 ppm).

Acknowledgements

I would like to thank Bryan Ringstrand for his constant and willing help in various aspects of the organic syntheses: devising reaction pathways, preparing solvents, using catalysts, purification, and setting up reactions under inert atmosphere. I would also like to thank Dr. Piotr Kaszynski for recommending the triisopropylsilanethiol as a protected thiolating reagent. I would also like to acknowledge some assistance from Joe Keene during his rotation in the lab.

APPENDIX D

PURIFICATION AND CHARACTERIZATION DATA FOR SYNTHETIC PEPTIDES USED IN THIS STUDY OR OTHERWISE DESIGNED AND PURIFIED

Table 14: Characterization data for peptides synthesized by this author. The sequences are labeled as the single letter amino acid abbreviations, the identity of the termini (unlabeled termini indicates that both termini were left as the free amine or carboxylic acid, CONH₂ is an amidated C terminus, and Ac is an acetylated N terminus), and (PEG)₆ indicates a hexaethyleneglycol spacer. Retention times are from reverse phase, preparatory scale HPLC and represent the time (rounded to the nearest minute) at which collection of the highest absorbing fraction was began. Calculated m/z values represent the value calculated for the most abundant isotope for reflectron mode, or the average mass for linear mode. The most prevalent ions in the MALDI spectrum of the highest absorbing fraction were recorded. [M + H] and [M + Na] were assumed to be indicative of a successful synthesis, while [M + O] is indicative of an oxidized methionine residue (not generally considered to effect peptide-antibody binding). Mode indicates reflectron (R) or linear (L) time of flight for the MALDI characterization.

Sequence	retention time (min)	ion	calculated m/z	observed m/z	error (ppm)	mode	yield (mg)
H ₂ N-C(PEG) ₆ NSELLSLINDMPITNDQKKLMSNN(PEG) ₆ C-CONH ₂	39	[M + H] ⁺	3609.7872	3609.8594	20.001179	R	5.6
		[M + Na] ⁺	3631.7691	3631.592	-48.764113		
		[M + H ₂ O] ⁺	3627.79777	3627.8363	10.622147		
	37	[M + H] ⁺	3609.7872	3609.8196	8.9755983	R	6.9
		[M + Na] ⁺	3631.7691	3631.8269	15.915109		
H ₂ N-C(PEG) ₆ NSELLSLINDMPITNDQKKLMSNN-CONH ₂	38	[M + H] ⁺	3171.5676	3171.55733	-3.238146	R	6.3
		[M + Na] ⁺	3193.5495	3193.6757	39.517158		
	39	[M + H] ⁺	3171.5676	3171.6936	39.727988	R	2.9
CKYNDKLPYISNPC	25	[M + H] ⁺	1769.8713	1769.4893	-215.834903	R	11.1
		[M + Na] ⁺	1791.8532	1791.3846	-261.516959		
	26	[M + H] ⁺	1769.8713	1769.6119	-146.564329	R	14.2
		[M + Na] ⁺	1791.8532	1791.3874	-259.954331		
C(PEG) ₆ KYNDKLPYISNP(PEG) ₆ C	30	[M + Na] ⁺	2463.48454	2463.4374	-19.137120	R	12.3
	30	[M + Na] ⁺	2463.48454	2463.7249	97.567489	R	11.2
Ac-NSELLSLINDGSGSC-CONH ₂	24	[M + Na] ⁺	1571.69874	1571.2008	-316.818984	R	*
Ac-SELLSLINDMGSFGSC-CONH ₂	27	[M + Na] ⁺	1588.69634	1588.2592	-275.158939	R	*
Ac-ELLSLINDMPGSGSC-CONH ₂	26	[M + Na] ⁺	1598.71654	1598.7421	15.985323	R	*
Ac-LLSLINDMPIGSGS-CONH ₂	27	[M + Na] ⁺	1582.75854	1582.4455	-197.783800	R	*
Ac-LSLINDMPITGSGSC-CONH ₂	24	[M + Na] ⁺	1570.72214	1570.852	82.672801	R	*
Ac-SLINDMPITNGSGSC-CONH ₂	23	[M + Na] ⁺	1571.68104	1571.4155	-168.955400	R	*
Ac-LINDMPITNDGSGSC-CONH ₂	23	[M + Na] ⁺	1599.67594	1599.4242	-157.371873	R	*
Ac-CSGSGNSELLSLINDMPITNDQKKLMSNN-CONH ₂	25	[M + Na] ⁺	3186.48454	3186.0723	-129.372666	R	*
Ac-NSELLSLINDMPITNDQKKLMSNNGSGSC-CONH ₂	26	[M + Na] ⁺	3186.48454	3186.0175	-146.570301	R	*
Ac-CSGSGNSELLSLINDMPITNDQKKLMSNNGSGSC-CONH ₂	26	[M + Na] ⁺	3579.97004	3574.18	-1617.344260	L	*
CSGSGNSELLSLIND	31	[M + Na] ⁺	1530.67224	1530.2344	-286.046867	R	13.9
CSGSGSELLSLINDM	37	[M + Na] ⁺	1547.66974	1547.1988	-304.292309	R	13.3
CSGSGELSLINDMP	35	[M + Na] ⁺	1557.69054	1557.0032	-441.258376	R	13.4
CSGSGLSLINDMPI	38	[M + Na] ⁺	1541.73194	1541.5425	-122.877392	R	18.2
CSGSGLSLINDMPIT	30	[M + Na] ⁺	1528.68774	1528.663	-16.186432	R	17.4
CSGSGLSLINDMPITN	26	[M + Na] ⁺	1530.65444	1530.7704	75.755831	R	11.5
CSGSGLINDMPITND	5	[M + Na] ⁺	1558.64934	1558.6397	-6.187408	R	10.7
CSGSGINDMPITNDQ	5	[M + Na] ⁺	1573.62384	1573.4026	-140.595226	R	27.1
CSGSGNDMPITNDQK	5	[M + H] ⁺	1566.6529	1566.8284	112.022261	R	13
CSGSGMPITNDQK	5	[M + H] ⁺	1580.7049	1581.0735	233.187105	R	22.2
CSGSGMPITNDQKLL	5	[M + H] ⁺	1578.762	1578.3384	-268.311500	R	19.6
CSGSGPITNDQKLLM	5	[M + O] ⁺	1593.749	1594.3453	374.149254	R	23.6
		[M + H] ⁺	1578.762	1578.3568	-256.656798	R	
CSGSGITNDQKLLMS	5	[M + Na] ⁺	1590.72324	1591.1441	264.568964	R	32.1
		[M + H] ⁺	1568.7413	1569.0895	221.961390	R	
CSGSGTNDQKLLMSN	5	[M + Na] ⁺	1591.68204	1591.0812	-377.489966	R	25.9
		[M + H] ⁺	1569.7001	1570.0826	243.677120	R	
		[M + O] ⁺	1584.6871	1585.0651	238.532894	R	
CSGSGNDQKLLMSNN	5	[M + Na] ⁺	1582.6954	1582.5573	-87.256209	R	24.2

APPENDIX E

ADDENDUM TO “COLOR MY NANOWORLD” EXERCISE USED AT THE VANDERBILT SUMMER ACADEMY

The Vanderbilt Summer Academy is a collaborative effort within Vanderbilt that invites gifted high school underclassmen to campus in order to learn about nanoscale science and engineering. Every year, the research group of David Cliffler participates and teaches kids about gold nanoparticles through a brief lecture followed by a hands-on experience. For that section, an article from J.Chem. Ed from Mirkin and coworkers, entitled “Color my Nanoworld” is used, in which the students make citrate stabilized gold nanoparticles and study their properties colorimetrically. In order to enhance this experience, I designed an addendum to the experience where the students study hexanethiol protected gold nanoparticles from a Brust synthesis. The addendum is as follows:

Brian Turner

6-23-10

Monolayer Protected Cluster

Supplement for “Color my Nanoworld”

Vanderbilt Summer Academy

Chemicals required

1. Hexanethiol (C₆SH)
2. Tetraoctylammonium bromide (TOABr)
3. Tetrachloroauric acid (HAuCl₄)
4. Sodium borohydride (NaBH₄)
5. Toluene
6. Water

Materials Required:

1. Small glass vials.
2. Gloves.
3. Safety goggles.
4. Tongs.
5. Heat plates.
6. Plastic droppers.
7. Large tagged container for waste.
8. Secondary waste container.

Preparation of solutions:

1. C6SH: Use as is. Will be delivered by micropipette.
2. TOABr: For a 2 mM solution in toluene, add _____g of TOABr to _____ mL of toluene. Can be prepared ahead of time.
3. HAuCl4: Use the same 1 mM solution of HAuCl4 from “Color my Nanoworld.” Again, this should be prepared immediately before the lab, or stored cold.
4. NaBH4: For a 30 mM solution, dissolve _____g of NaBH4 in _____mL of water. This solution should be prepared immediately before use. It is possible that this solution loses its potency, and requires a new preparation part way through the lab.

Procedure for the Preparation of 3nm Gold Hexanethiol Monolayer Protected Clusters (MPCs)

1. In a small vial, add 1 dropper full of TOABr solution. To this, add the aqueous HAuCl4 solution.
2. Option A: Cap and shake the vial vigorously to temporarily mix the layers together. Option B: Use a dropper to mix the layers over and over. Either method should be done until you have 1 red layer and 1 colorless layer (not faintly yellow).
3. Use a pipet to remove the clear aqueous layer (which should be dilute hydrobromic acid). The remaining layer should be toluene with 1mM tris(tetraoctylammonium) gold(III).
4. To the red organic layer, add _____ μL of C6SH (3:1 molar excess). Subsequent reduction of gold(III) to gold(I) may be observed by a color change from red to colorless.
5. Immediately upon fading of the red color, CAUTIOUSLY add 1 dropper full of NaBH4 solution (in the hood). Continuously mix with the dropper. Capping and shaking is an option, but should be done carefully while holding the

lid on very tightly, and easing the lid off after reduction. This should render a black solution.

Concepts:

1. It should be noted that these particles are more stable than the citrate particles because they are protected by covalently bonded layer of hexanethiolate molecules.
2. Throughout the course of all of the experiments, the children have observed a variety of colors.
 - a. RED from large particles scattering multiple wavelengths of light unequally and absorbing a specific wavelength of light.
 - b. BLUE from larger particles aggregating and scattering and absorbing light differently.
 - c. YELLOW from small gold complexes absorbing light by transferring charge between the metal and ligand.
 - d. RED from small gold complexes absorbing light by transferring charge between the metal and a *different* ligand.
 - e. BLACK or BROWN from differently sized smaller particles scattering light and absorbing a small portion of light.
3. This is a good time to tell the kids about how scientists can use light to gain details about molecules and particles such as their size.

The numbers are left blank so that the teaching assistants customize to suit the class.

REFERENCES

1. Clifffel, D. E., Turner, B. N. and Huffman, B. J. (2009) Nanoparticle-based biologic mimetics. *Wiley Interdisciplinary Reviews-Nanomedicine and Nanobiotechnology*, **1**, 47-59.
2. Faraday, M. (1857) The Bakerian Lecture: Experimental Relations of Gold (and Other Metals) to Light. *Philos Trans R Soc London*, **147**, 145.
3. Turkevich, J., Stevenson, P. C. and Hillier, J. (1951) A Study of the Nucleation and Growth Processes in the Synthesis of Colloidal Gold. *Discuss Faraday Soc*, **11**, 55-75.
4. Brust, M., Walker, M., Bethell, D., Schiffrin, D. J. and Whyman, R. (1994) Synthesis of thiol-derivatized gold nanoparticles in a two-phase liquid-liquid system. *Chem Commun*, **7**, 801-902.
5. Templeton, A. C., Wuelfing, W. P. and Murray, R. W. (2000) Monolayer-Protected Cluster Molecules. *Acc Chem Res* **33**, 27-36.
6. Niemeyer, C. M. (2001) Nanoparticles, Proteins, and Nucleic Acids: Biotechnology Meets Materials Science. *Angew Chem Int Ed*, **40**.
7. Rowe, R. P., Plass, K. E., Kim, K., Kurdak, C., Zellers, E. T. and Matzger, A. J. (2004) Single-Phase Synthesis of Functionalized Gold Nanoparticles. *Chem Mater*, **16**, 3513-3517.
8. Templeton, A. C., Chen, S., Gross, S. M. and Murray, R. W. (1999) Water-Soluble, Isolable Gold Clusters Protected by Tiopronin and Coenzyme A Monolayers. *Langmuir*, **15**, 66-76.
9. Templeton, A. C., Clifffel, D. E. and Murray, R. W. (1999) Redox and Fluorophore Functionalization of Water-Soluble, Tiopronin-Protected Gold Clusters. *J Am Chem Soc*, **121**, 7081-7089.
10. Yee, C., Scotti, M., Ulman, A., White, H., Rafailovich, M. and Sokolov, J. (1999) One-Phase Synthesis of Thiol-Functionalized Platinum Nanoparticles. *Langmuir*, **15**, 4314-4316.
11. Yee, C. K., Jordan, R., Ulman, A., White, H., King, A., Rafailovich, M. and Sokolov, J. (1999) Novel One-Phase Synthesis of Thiol-Functionalized Gold Palladium and Iridium Nanoparticles Using Superhydride. *Langmuir*, **15**, 3486-3491.

12. Croce, T. A., Hamilton, S. K., Chen, M. L., Muchalski, H. and Harth, E. (2007) Alternative *o*-Chinodimethane Crosslinking Precursors for Intramolecular Chain Collapse Nanoparticles. *Macromolecules*, **40**, 6028-6031.
13. Ahmed, F., Photos, P. J. and Discher, D. E. (2006) Polymersomes as Viral Capsid Mimics. *Drug Dev Res*, **67**, 4-14.
14. Joralemon, M. J., Smith, N. L., Holowka, D., Baird, B. and Wooley, K. L. (2005) Antigen-Decorated Shell Cross-Linked Nanoparticles: Synthesis, Characterization, and Antibody Interactions. *Bioconjugate Chem*, **16**, 1246-1256.
15. Taubert, A., Napoli, A. and Meier, W. (2004) Self-assembly of reactive amphiphilic block copolymers as mimetics for biological membranes. *Curr Opin Chem Bio*, **8**, 598-603.
16. Bosio, C. M., Moore, B. D., Warfield, K. L., Ruthel, G., Mohamadzadeh, M., Aman, M. J. and Bavari, S. (2004) Ebola and Marburg virus-like particles activate human myeloid dendritic cells. *Virology*, **326**, 280-287.
17. Noad, R. and Roy, P. (2003) Virus-like particles as immunogens. *Trends Microbiol*, **11**, 438-444.
18. Ogasawara, Y., Amexis, G., Yamaguchi, H., Kajigaya, S., Leppla, S. H. and Young, N. S. (2006) Recombinant Viral-like Particles of Parvovirus B19 as Antigen Carriers of Anthrax Protective Antigen. *in vivo*, **20**.
19. Raja, K. S., Wang, Q. and Finn, M. G. (2003) Icosahedral Virus Particles as Polyvalent Carbohydrates Display Platforms. *ChemBioChem*, **4**, 1348-1351.
20. Szécsi, J., Boson, B., Johnsson, P., Dupeyrot-Lacs, P., Matrosovich, M., Klenk, H.-D., Klatzmann, D., Volchkov, V. and Cosset, F.-L. (2006) Induction of Neutralising antibodies by virus-like particles harbouring surface proteins from highly pathogenic H5N1 and H7N1 influenza viruses. *Virol J*, **3**.
21. Wang, Q., Lin, T., Tang, L., Johnson, J. E. and Finn, M. G. (2002) Icosahedral Virus Particles as Addressable Nanoscale Building Blocks. *Angew Chem Int Ed* **41**, 459-462.
22. Jahanshahi, M., Williams, S., Lyddiatt, A. and Shojaosadati, S. A. (2004) Preparation and purification of synthetic protein nanoparticles. *IEE Proc-Nanobiotechnol*, **151**, 176-182.
23. Gole, A., Vyas, S., Phadtare, S., Lachke, A. and Sastry, M. (2002) Studies on the formation of bioconjugates of *Endoglucanase* with colloidal gold. *Colloids Surf, B*, **25**, 129-138.

24. Lyon, L. A., Peña, D. J. and Natan, M. J. (1999) Surface Plasmon Resonance of Au Colloid-Modified Au Films: Particle Size Dependence. *J Phys Chem B*, **103**, 5826-5831.
25. Matsuya, T., Tashiro, S., Hoshino, N., Shibata, N., Nagasaki, Y. and Kataoka, K. (2003) A Core-Shell Type Fluorescent Nanosphere Possessing Reactive Poly(ethylene glycol) Tethered Chains on the Surface of Zeptomole Detection of Protein in Time-Resolved Fluorometric Immunoassay. *Anal Chem*, **75**.
26. Whetten, R. L., Shafigullin, M. N., Khoury, J. T., Schaaff, T. G., Vezmar, I., Alvarez, M. M. and Wilkinson, A. (1999) Crystal Structures of Molecular Gold Nanocrystal Arrays. *Acc Chem Res*, **32**, 397-406.
27. Gies, A. P., Hercules, D. M., Gerdon, A. E. and Cliffler, D. E. (2007) Electrospray mass spectrometry study of tiopronin monolayer-protected gold nanoclusters. *J Am Chem Soc*, **129**, 1095-1104.
28. Schaaff, T. G., Knight, G., Shafigullin, M. N., Borkman, R. F. and Whetten, R. L. (1998) Isolation and selected properties of a 10.4 kDa Gold : Glutathione cluster compound. *J Phys Chem B*, **102**, 10643-10646.
29. Johnson, S. R., Evans, S. D. and Brydson, R. (1998) Influence of a terminal functionality on the physical properties of surfactant-stabilized gold nanoparticles. *Langmuir*, **14**, 6639-6647.
30. Ackerson, C. J., Jadzinsky, P. D. and Kornberg, R. D. (2005) Thiolate ligands for synthesis of water-soluble gold clusters. *J Am Chem Soc*, **127**, 6550-6551.
31. Cliffler, D. E., Zamborini, F. P., Gross, S. M. and Murray, R. W. (2000) Mercaptoammonium-monolayer-protected, water-soluble gold, silver, and palladium clusters. *Langmuir*, **16**, 9699-9702.
32. Hostetler, M. J., Green, S. J., Stokes, J. J. and Murray, R. W. (1996) Monolayers in three dimensions: Synthesis and electrochemistry of omega-functionalized alkanethiolate-stabilized gold cluster compounds. *J Am Chem Soc*, **118**, 4212-4213.
33. Hostetler, M. J., Templeton, A. C. and Murray, R. W. (1999) Dynamics of Place-Exchange Reactions on Monolayer-Protected Gold Cluster Molecules. *Langmuir*, **15**, 3782-3789.
34. Kassam, A., Bremner, G., Clark, B., Ulibarri, G. and Lennox, R. B. (2006) Place exchange reactions of alkyl thiols on gold nanoparticles. *J Am Chem Soc*, **128**, 3476-3477.

35. Montalti, M., Prodi, L., Zaccheroni, N., Baxter, R., Teobaldi, G. and Zerbetto, F. (2003) Kinetics of place-exchange reactions of thiols on gold nanoparticles. *Langmuir*, **19**, 5172-5174.
36. Hong, R., Fernandez, J. M., Nakade, H., Arvizo, R., Emrick, T. and Rotello, V. M. (2006) In situ observation of place exchange reactions of gold nanoparticles. Correlation of monolayer structure and stability. *Chem Commun*, 2347-2349.
37. Häkkinen, H., Barnett, R. N. and Landman, U. (1999) Electronic structure of passivated Au-38(SCH₃)₂₄ nanocrystal. *Phys Rev Lett*, **82**, 3264-3267.
38. Donkers, R. L., Song, Y. and Murray, R. W. (2004) Substituent effects on the exchange dynamics of ligands on 1.6 nm diameter gold nanoparticles. *Langmuir*, **20**, 4703-4707.
39. Song, Y. and Murray, R. W. (2002) Dynamics and extent of ligand exchange depend on electronic charge of metal nanoparticles. *J Am Chem Soc*, **124**, 7096-7102.
40. Myung, N., Bae, Y. and Bard, A. J. (2003) Effect of surface passivation on the electrogenerated chemiluminescence of CdSe/ZnSe nanocrystals. *Nano Lett*, **3**, 1053-1055.
41. Chechik, V. (2004) Reduced reactivity of aged Au nanoparticles in ligand exchange reactions. *J Am Chem Soc*, **126**, 7780-7781.
42. Häkkinen, H., Walter, M. and Grönbeck, H. (2006) Divide and Protect: Capping Gold Nanoclusters with Molecular Gold-Thiolate Rings. *J Phys Chem B*, **110**, 9927-9931.
43. Kornberg, R. D., Jadzinsky, P. D., Calero, G., Ackerson, C. J. and Bushnell, D. A. (2007) Structure of a thiol monolayer-protected gold nanoparticle at 1.1 angstrom resolution. *Science*, **318**, 430-433.
44. Heaven, M. W., Dass, A., White, P. S., Holt, K. M. and Murray, R. W. (2008) Crystal structure of the gold nanoparticle [N(C₈H₁₇)₄][Au-25(SCH₂CH₂Ph)₁₈]. *J Am Chem Soc*, **130**, 3754-+.
45. Whetten, R. L. and Price, R. C. (2007) Nano-golden order. *Science*, **318**, 407-408.
46. Harkness, K. M. Dissertation, Vanderbilt University, Nashville, TN, 2011.

47. Worden, J. G., Shaffer, A. W. and Huo, Q. (2004) Controlled functionalization of gold nanoparticles through a solid phase synthesis approach. *Chem Commun*, 518-519.
48. Shaffer, A. W., Worden, J. G. and Huo, Q. (2004) Comparison study of the solution phase versus solid phase place exchange reactions in the controlled functionalization of gold nanoparticles. *Langmuir*, **20**, 8343-8351.
49. Liu, X., Worden, J. G., Dai, Q., Zou, J. H., Wang, J. H. and Huo, Q. (2006) Monofunctional gold nanoparticles prepared via a noncovalent-interaction-based solid-phase modification approach. *Small*, **2**, 1126-1129.
50. Bardea, A., Dagan, A., Ben-Dov, I., Amit, B. and Willner, I. (1998) Amplified microgravimetric quartz-crystal-microbalance analyses of oligonucleotide complexes: a route to a Tay-Sachs biosensor device. *Chem Commun*, 839-840.
51. Ghosh, S. S., Kao, P. M., McCue, A. W. and Chappelle, H. L. (1990) Use of Maleimide-Thiol Coupling Chemistry for Efficient Syntheses of Oligonucleotide-Enzyme Conjugate Hybridization Probes. *Bioconjugate Chem*, **1**, 71-76.
52. Iyer, R. P., Egan, W., Regan, J. B. and Beaucage, S. L. (1990) 3H-1,2-Benzodithiole-3-one 1,1-Dioxide as an Improved Sulfurizing Reagent in the Solid-Phase Synthesis of Oligodeoxyribonucleoside Phosphorothioates. *J Am Chem Soc*, **112**, 1253-1254.
53. Connolly, S. and Fitzmaurice, D. (1999) Programmed assembly of gold nanocrystals in aqueous solution. *Adv Mater*, **11**, 1202-1205.
54. Huffman, B. J. Dissertation, Vanderbilt University, Nashville, 2009.
55. Sweeney, S. F., Woehrle, G. H. and Hutchison, J. E. (2006) Rapid purification and size separation of gold nanoparticles via diafiltration. *J Am Chem Soc*, **128**, 3190-3197.
56. Fleming, D. A., Thode, C. J. and Williams, M. E. (2006) Triazole cycloaddition as a general route for functionalization of Au nanoparticles. *Chem Mater*, **18**, 2327-2334.
57. Tan, H., Zhan, T. and Fan, W. Y. (2006) Direct functionalization of the hydroxyl group of the 6-mercapto-1-hexanol (MCH) ligand attached to gold nanoclusters. *J Phys Chem B*, **110**, 21690-21693.
58. Templeton, A. C., Hostetler, M. J., Warmoth, E. K., Chen, S., Hartshorn, C. M., Krishnamurthy, V. M., Forbes, M. D. E. and Murray, R. W. (1998) Gateway

Reactions to Diverse, Polyfunctional Monolayer-Protected Gold Clusters. *J Am Chem Soc*, **120**, 4845-4849.

59. Tai, Y., Murakami, J., Saito, K., Ikeyama, M., Tajiri, K., Watanabe, M., Tanemura, S. and Mizota, T. (2003) Plasma desorption mass spectroscopy of thiol-passivated gold nanoparticles. *Eur Phys J D*, **24**, 261-263.
60. Whetten, R. L., Khoury, J. T., Alvarez, M. M., Murthy, S., Vezmar, I., Wang, Z. L., Stephens, P. W., Cleveland, C. L., Luedtke, W. D. and Landman, U. (1996) Nanocrystal gold molecules. *Adv Mater*, **8**, 428-&.
61. Terrill, R. H., Postlethwaite, T. A., Chen, C. H., Poon, C. D., Terzis, A., Chen, A. D., Hutchison, J. E., Clark, M. R., Wignall, G., Londono, J. D., Superfine, R., Falvo, M., Johnson, C. S., Samulski, E. T. and Murray, R. W. (1995) Monolayers in three dimensions: NMR, SAXS, thermal, and electron hopping studies of alkanethiol stabilized gold clusters. *J Am Chem Soc*, **117**, 12537-12548.
62. Badia, A., Cuccia, L., Demers, L., Morin, F. and Lennox, R. B. (1997) Structure and dynamics in alkanethiolate monolayers self-assembled on gold nanoparticles: A DSC, FT-IR, and deuterium NMR study. *J Am Chem Soc*, **119**, 2682-2692.
63. Hostetler, M. J., Wingate, J. E., Zhong, C. J., Harris, J. E., Vachet, R. W., Clark, M. R., Londono, J. D., Green, S. J., Stokes, J. J., Wignall, G. D., Glish, G. L., Porter, M. D., Evans, N. D. and Murray, R. W. (1998) Alkanethiolate gold cluster molecules with core diameters from 1.5 to 5.2 nm: Core and monolayer properties as a function of core size. *Langmuir*, **14**, 17-30.
64. Templeton, A. C., Hostetler, M. J., Kraft, C. T. and Murray, R. W. (1998) Reactivity of Monolayer-Protected Gold Cluster Molecules: Steric Effects. *J Am Chem Soc*, **120**, 1906-1911.
65. Harkness, K. M., Hixson, B. C., Fenn, L. S., Turner, B. N., Rape, A. C., Simpson, C. A., Huffman, B. J., Okoli, T. C., Cliffel, D. E. and McLean, J. A. (2010) A Structural Mass Spectrometry Strategy for the Relative Quantitation of Ligands on Mixed Monolayer-Protected Gold Nanoparticles. *Analytical Chemistry*, **82**, 9268-9274.
66. Bower, P. V., Louie, E. A., Long, J. R., Stayton, P. S. and Drobny, G. P. (2005) Solid-state NMR structural studies of peptides immobilized on gold nanoparticles. *Langmuir*, **21**, 3002-3007.
67. Mandal, H. S. and Kraatz, H.-B. (2007) Effect of the Surface Curvature on the Secondary Structure of Peptides Adsorbed on Nanoparticles. *J Am Chem Soc*, **129**, 6356-6357.

68. Slocik, J. M. and Naik, R. R. (2010) Probing peptide-nanomaterial interactions. *Chem Soc Rev*, **39**, 3454-3463.
69. Collins, P., Chanock, R. M. and Murphy, B. R. Respiratory Syncytial Virus In *Fields Virology*, 4th ed.; Knipe, D. M., Howley, P. M., Eds.; Lippincott, Williams, and Wilkins: Philadelphia, PA, 2001; Vol. 1, pp 1443-1485.
70. Holberg, C. J., Wright, A. L., Martinez, F. D., Ray, C. G., Taussig, L. M. and Lebowitz, M. D. (1991) Risk Factors for Respiratory Syncytial Virus-associated Lower Respiratory Illnesses in the First Year of Life. *Am J Epidemiol*, **133**, 1135-1151.
71. Maes, P.; RSV-1.img, Ed.; Katholieke Universiteit Leuven, 2011.
72. Connors, M., Collins, P. L., Firestone, C.-Y. and Murphy, B. R. (1991) Respiratory Syncytial Virus (RSV) F, G, M2 (22K), and N Proteins each induce resistance to RSV challenge, but resistance induced by M2 and N proteins is relatively short-lived. *J Virol*, **65**, 1634-1637.
73. Bukreyev, A., Whitehead, S. S., Murphy, B. R. and Collins, P. L. (1997) Recombinant respiratory syncytial virus from which the entire SH gene has been deleted grows efficiently in cell culture and exhibits site-specific attenuation in the respiratory tract of the mouse. *J Virol*, **71**, 8973-8982.
74. Karron, R. A., Wright, P. F., Belshe, R. B., Thumar, B., Casey, R. and Newman, F. (2005) Identification of a recombinant live attenuated respiratory syncytial virus vaccine candidate that is highly attenuated in infants. *J Infect Dis*, **22**, 394-405.
75. Arbiza, J., Taylor, G., Lopez, J. A., Furze, J., Wyld, S., Whyte, P., Stott, E. J., Wertz, G., Sullender, W., Trudel, M. and Melero, J. A. (1992) Characterization of 2 Antigenic Sites Recognized by Neutralizing Monoclonal-Antibodies Directed against the Fusion Glycoprotein of Human Respiratory Syncytial Virus. *J Gen Virol*, **73**, 2225-2234.
76. Morton, C. J., Cameron, R., Lawrence, L. J., Lin, B., Lowe, M., Luttick, A., Mason, A., McKimm-Breschkin, J., Parker, M. W., Ryan, J., Smout, M., Sullivan, J., Tucker, S. P. and Young, P. R. (2003) Structural characterization of respiratory syncytial virus fusion inhibitor escape mutants: homology model of the F protein and a syncytium formation assay. *Virology*, **311**, 275-288.
77. Smith, B. J., Lawrence, M. C. and Colman, P. M. (2002) Modelling the structure of the fusion protein from human respiratory syncytial virus. *Prot Eng*, **15**, 365-371.

78. Beeler, J. A. and van Wyke Coelingh, K. (1989) Neutralization Epitopes of the F Glycoprotein of Respiratory Syncytial Virus: Effect of Mutation upon Fusion Function. *J Virol*, **63**, 2941-2950.
79. Tous, G., Schenerman, M., Casas-Finet, J., Wei, Z. and Pfarr, D. S. In *PCT Int Appl*, 2006.
80. Zhao, X. D., Chen, F. P., Megaw, A. G. and Sullender, W. M. (2004) Variable resistance to palivizumab in cotton rats by respiratory syncytial virus mutants. *J Infect Dis*, **190**, 1941-1946.
81. Zhao, X. D., Chen, F. P. and Sullender, W. M. (2004) Respiratory syncytial virus escape mutant derived in vitro resists palivizumab prophylaxis in cotton rats. *Virology*, **318**, 608-612.
82. Zhao, X. D., Liu, E. M., Chen, F. P. and Sullender, W. M. (2006) Vitro and in vivo fitness of respiratory syncytial virus monoclonal antibody escape mutants. *J Virol*, **80**, 11651-11657.
83. Zhao, X. D. and Sullender, W. M. (2005) In vivo selection of respiratory syncytial viruses resistant to palivizumab. *J Virol*, **79**, 3962-3968.
84. Suzich, J. A., Zhu, Q., McAuliffe, J. M., Patel, N. K., Palmer-Hill, F. J., Yang, C. F., Liang, B., Su, L., Zhu, W., Wachter, L., Wilson, S., MacGill, R. S., Krishnan, S., McCarthy, M. P. and Losonsky, G. A. (2011) Analysis of Respiratory Syncytial Virus Preclinical and Clinical Variants Resistant to Neutralization by Monoclonal Antibodies Palivizumab and/or Motavizumab. *J Infect Dis*, **203**, 674-682.
85. Crowe, J. E., Jr., Firestone, C.-Y., Crim, R., Beeler, J. A., Coelingh, K. L., Barbas, C. F., III, Burton, D. R., Chanock, R. M. and Murphy, B. R. (1998) Monoclonal Antibody Resistant Mutants Selected with a Respiratory Syncytial Virus-Neutralizing Human Antibody Fab Fragment (Fab 19) Define a Unique Epitope on the Fusion (F) Glycoprotein. *Virology*, **252**, 373-375.
86. Johnson, S., Oliver, C., Prince, G. A., Hemming, V. G., Pfarr, D. S., Wang, S.-C., Dormitzer, M., O'Grady, J., Koenig, S., Tamura, J. K., Woods, R., Bansal, G., Couchenour, D., Tsao, E., Hall, W. C. and Young, J. F. (1997) Development of a Humanized Monoclonal Antibody (MEDI-493) with Potent In Vitro and In Vivo Activity against Respiratory Syncytial Virus. *J Infect Dis*, **176**, 1215-1224.
87. Padlan, E., Davies, D., Pecht, I., Givol, D. and Wright, C. 1977; 627-637.
88. McLellan, J. S., Chen, M., Chang, J.-S., Yang, Y., Kim, A., Graham, B. S. and Kwong, P. D. (2010) Structure of a Major Antigenic Site on the Respiratory

Syncytial Virus Fusion Glycoprotein in Complex with Neutralizing Antibody 101F. *Journal of Virology*, **84**, 12236-12244.

89. McLellan, J. S., Yang, Y., Graham, B. S. and Kwong, P. D. (2011) Structure of Respiratory Syncytial Virus Fusion Glycoprotein in the Postfusion Conformation Reveals Preservation of Neutralizing Epitopes. *J Virol*, **85**, 7788-7796.
90. McLellan, J. S., Chen, M., Kim, A., Yang, Y., Graham, B. S. and Kwong, P. D. (2010) Structural basis of respiratory syncytial virus neutralization by motavizumab. *Nature Structural & Molecular Biology*, **17**, 248-250.
91. Magro, M., Andreu, D., Gomez-Puertas, P., Melero, J. A. and Palomo, C. (2010) Neutralization of Human Respiratory Syncytial Virus Infectivity by Antibodies and Low-Molecular-Weight Compounds Targeted against the Fusion Glycoprotein. *Journal of Virology*, **84**, 7970-7982.
92. Rutledge, R. D., Huffman, B. J., Cliffler, D. E. and Wright, D. W. (2008) Design and synthesis of an antigenic mimic of the Ebola glycoprotein. *J Mat Res*, **23**, 3161-3168.
93. Sauerbrey, G. (1959) Verwendung von Schwingquarzen zur Wägung dünner Schichten und Microwägung. *Z Physik*, **155**, 206.
94. Janshoff, A., Galla, H.-J. and Steinem, C. (2000) Piezoelectric Mass-Sensing Devices as Biosensors- An Alternative to Optical Biosensors? *Angew Chem Int Ed*, **39**, 4004-4032.
95. Nomura, T. and Okuhara, M. (1982) Frequency Shifts of Piezoelectric Quartz Crystals Immersed in Organic Liquids. *Anal Chim Acta*, **142**, 281-284.
96. Jones, T. A., Kleitz, M., Lundström, I. and Göpel, W. *Micro- and Nano-sensor Technology/Trends in Sensor Markets*, VCH: New York, 1995.
97. Maxtek *Operation and Service Manual/Research Quartz Crystal Microbalance*, Second, Maxtek Inc.: Santa Fe Springs, CA, 2003.
98. Hillier, A. C. and Ward, M. D. (1992) Scanning Electrochemical Mass Sensitivity Mapping of the Quartz Crystal Microbalance in Liquid Media. *Anal Chem*, **64**, 2539-2554.
99. Josse, F., Lee, Y., Martin, S. J. and Cernosek, R. W. (1998) Analysis of the Radial Dependence of Mass Sensitivity for Modified-Electrode Quartz Crystal Resonators. *Anal Chem*, **70**, 237-247.

100. Kanazawa, K. K. and Gordon, J. G. (1985) Frequency of a Quartz Microbalance in Contact with Liquid. *Anal Chem*, **57**, 1770-1771.
101. Bandey, H. L., Martin, S. J., Cernosek, R. W. and Hillman, A. R. (1999) Modeling the responses of thickness-shear mode resonators under various loading conditions. *Anal Chem*, **71**, 2205-2214.
102. Gerdon, A. E., Wright, D. W. and Cliffler, D. E. Quartz Crystal Microbalance Characterization of Nanostructure Assemblies in the Life Sciences In *Nanosystem Characterization Tools in the Life Sciences*; Kumar, C., Ed.; Wiley VCH: Weinheim, 2006; Vol. 3.
103. Koesslinger, C., Uttenhaler, E., Drost, S., Aberl, F., Wolf, H., Brink, G., Stanglmaier, A. and Sackmann, E. (1995) *Sens Actuators, B*, **24**, 107-112.
104. Spangler, B. D., Wilkinson, E. A., Murphy, J. T. and Tyler, B. J. (2001) Comparison of the Spreeta^(R) surface plasmon resonance sensor and a quartz crystal microbalance for detection of Escherichia coli heat-labile enterotoxin *Anal Chim Acta*, **444**, 149-161.
105. Gerdon, A. E., Wright, D. W. and Cliffler, D. E. (2005) Quartz Crystal Microbalance Detection of Glutathione-Protected Nanoclusters Using Antibody Recognition. *Anal Chem*, **77**, 304-310.
106. Rickert, J., Brecht, A. and Goepel, W. (1997) *Anal Chem*, **69**, 1441-1448.
107. Wijekoon, W. M. K. P., Asgharian, B., Casstevens, M., Samoc, M., Talapatra, G., Prasad, P., Geisler, T. and Rosenkilde, S. (1992) Electrooptic Effect in Langmuir-Blodgett Films of 2-(Docosylamino) -5-nitropyridine Probed by Surface Plasmon Waves. *Langmuir*, **8**, 135-139.
108. Keefer, C., 2006.
109. Batlas, S., Talley, E., Tran, M., Lichensein, R. and King, K. 1995.
110. Gerdon, A. E., Wright, D. W. and Cliffler, D. E. (2006) Epitope Mapping of the Protective Antigen of *B. Anthracis* by Using Nanoclusters Presenting Conformational Peptide Epitopes. *Angew Chem Int Ed*, **45**, 594-598.
111. Slocik, J. M., Moore, J. T. and Wright, D. W. (2002) Monoclonal Antibody Recognition of Histidine-Rich Peptide Encapsulated Nanoclusters. *Nano Lett*, **2**, 169-173.

112. Gerdon, A. E., Wright, D. W. and Cliffel, D. E. (2005) Hemagglutinin Linear Epitope Presentation on Monolayer-Protected Clusters Elicits Strong Antibody Binding. *Biomacromolecules*, **6**, 3419-3424.
113. Ingram, R. S., Hostetler, M. J. and Murray, R. W. (1997) Poly-hetero- ω -functionalized Alkanethiolate-Stabilized Gold Cluster Compounds. *J Am Chem Soc*, **119**, 9175-9178.
114. Slocik, J. M., Stone, M. O. and Naik, R. R. (2005) Synthesis of gold nanoparticles using multifunctional peptides. *Small*, **1**, 1048-1052.
115. Miller, S. A., Keil, R. G., Hiatt, L. A., Cliffel, D. E. and Wright, D. W. (2011) Nanoparticle Simulant for Influenza Virus. *Anal Bioanal Chem*, **399**, 1021-1029.
116. Mancin, F., Rio-Echevarria, I. M., Tavano, R., Causin, V., Papini, E. and Moretto, A. (2011) Water-Soluble Peptide-Coated Nanoparticles: Control of the Helix Structure and Enhanced Differential Binding to Immune Cells. *J Am Chem Soc*, **133**, 8-11.
117. Simpson, C. A., Huffman, B. J., Gerdon, A. E. and Cliffel, D. E. (2010) Unexpected Toxicity of Mono layer Protected Gold Clusters Eliminated by PEG-Thiol Place Exchange Reactions. *Chem Res Tox*, **23**, 1608-1616.
118. Yu, J. S., Liao, H. X., Gerdon, A. E., Huffman, B., Scarce, R. M., McAdams, M., Alam, S. M., Popernack, P. M., Sullivan, N. J., Wright, D., Cliffel, D. E., Nabel, G. J. and Haynes, B. F. (2006) Detection of Ebola virus envelope using monoclonal and polyclonal antibodies in ELISA, surface plasmon resonance and a quartz crystal microbalance immunosensor. *J Virol Meth*, **137**, 219-228.
119. Zhang, Y. and Cliffel, D. E. (2011) Quartz Crystal Microbalance Detector for Avian Influenza Virus. *In Preparation*.
120. Hiatt, L. A. and Cliffel, D. E. (2011) Detection of Mycobacterium Tuberculosis and Lipoarabinomannan with a Quartz Crystal Microbalance Immunosensor. *In Preparation*.
121. Brauer, G. *Handbook of preparative inorganic chemistry*, 2d, Academic Press: New York,, 1963.
122. Templeton, A. C., Chen, S. W., Gross, S. M. and Murray, R. W. (1999) Water-soluble, isolable gold clusters protected by tiopronin and coenzyme A monolayers. *Langmuir*, **15**, 66-76.
123. Zhang, Y., Turner, B. N., Krim, M., Swartz, J., Wright, D. W., Crowe, J. E., Jr and Cliffel, D. E. (2011) Untitled work in preparation.

124. Zuo, B., Li, S., Guo, Z., Zhang, J. and Chen, C. (2004) Piezoelectric Immunosensor for SARS-Associated Coronavirus in Sputum. *Anal Chem*, **76**, 3536-3540.
125. McLellan, J. S., Correia, B. E., Chen, M., Yang, Y. P., Graham, B. S., Schief, W. R. and Kwong, P. D. (2011) Design and Characterization of Epitope-Scaffold Immunogens That Present the Motavizumab Epitope from Respiratory Syncytial Virus. *J Mol Bio*, **409**, 853-866.
126. Ebara, Y., Itakura, K. and Okahata, Y. (1996) Kinetic studies of molecular recognition based on hydrogen bonding at the air-water interface by using a highly sensitive quartz-crystal microbalance. *Langmuir*, **12**, 5165-5170.
127. Ebato, H., Gentry, C. A., Herron, J. N., Muller, W., Okahata, Y., Ringsdorf, H. and Suci, P. A. (1994) Investigation of Specific Binding of Antifluorescyl Antibody and Fab to Fluorescein Lipids in Langmuir-Blodgett Deposited Films Using Quartz-Crystal Microbalance Methodology. *Anal Chem*, **66**, 1683-1689.
128. Rodbard, D., Feldman, Y., Jaffe, M. L. and Miles, L. E. M. (1978) Kinetics of 2-Site Immunoradiometric (Sandwich) Assays .2. Studies on Nature of High-Dose Hook Effect. *Immunochem*, **15**, 77-82.
129. Ryall, R. G., Story, C. J. and Turner, D. R. (1982) Reappraisal of the Causes of the Hook Effect in 2-Site Immunoradiometric Assays. *Anal Biochem*, **127**, 308-315.
130. Atkins, P. and de Paula, J. *Physical Chemistry*, 7th, W. H. Freeman: New York, 2002.
131. Kankare, J. and Vinokurov, I. A. (2002) Kinetics of multilayer Langmuirian adsorption. *Langmuir*, **18**, 6789-6795.
132. Balinski, A., Vanderbilt University, Nashville, TN, 2011.
133. Bruckenstein, S. and Shay, M. (1985) Experimental Aspects of Use of the Quartz Crystal Microbalance in Solution. *Electrochimica Acta*, **30**, 1295-1300.
134. Feldheim, D. (2000) Nanotechnology - Flipping a molecular switch. *Nature*, **408**, 45-46.
135. Nichols, R. J., Gittins, D. I., Bethell, D. and Schiffrin, D. J. (2000) A nanometre-scale electronic switch consisting of a metal cluster and redox-addressable groups. *Nature*, **408**, 67-69.

136. Blum, A. S., Soto, C. M., Sapsford, K. E., Wilson, C. D., Moore, M. H. and Ratna, B. R. (2011) Molecular electronics based nanosensors on a viral scaffold. *Biosens Bioelectron*, **26**, 2852-2857.
137. Hicks, J. F., Miles, D. T. and Murray, R. W. (2002) Quantized double-layer charging of highly monodisperse metal nanoparticles. *J Am Chem Soc*, **124**, 13322-13328.
138. Peterson, R. R. and Cliffel, D. E. (2006) Scanning electrochemical microscopy determination of organic soluble MPC electron-transfer rates. *Langmuir*, **22**, 10307-10314.
139. Hicks, J. F., Zamborini, F. P., Osisek, A. and Murray, R. W. (2001) The dynamics of electron self-exchange between nanoparticles. *J Am Chem Soc*, **123**, 7048-7053.
140. Wuelfing, W. P. and Murray, R. W. (2002) Electron hopping through films of arenethiolate monolayer-protected gold clusters. *J Phys Chem B*, **106**, 3139-3145.
141. Caban, K., Offenhausser, A. and Mayer, D. (2009) Electrochemical characterization of the effect of gold nanoparticles on the electron transfer of cytochrome c. *Phys Stat Sol A*, **206**, 489-500.
142. Vijayamohanan, K., Chaki, N. K., Aslam, M., Gopakumar, T. G., Sharma, J., Pasricha, R. and Mulla, I. S. (2003) Effect of chain length and the nature of the monolayer on the electrical behavior of hydrophobically organized gold clusters. *J Phys Chem B*, **107**, 13567-13574.
143. Leopold, M. C., Sheibley, D., Tognarelli, D. J. and Szymanik, R. (2005) Ultra-fast formation and characterization of stable nanoparticle film assemblies. *J Mat Chem*, **15**, 491-498.
144. Ozoemena, K. I., Pillay, J., Tshikhudo, R. T. and Moutloali, R. M. (2010) Monolayer-Protected Clusters of Gold Nanoparticles: Impacts of Stabilizing Ligands on the Heterogeneous Electron Transfer Dynamics and Voltammetric Detection. *Langmuir*, **26**, 9061-9068.
145. Nitzan, A. and Ratner, M. A. (2003) Electron transport in molecular wire junctions. *Science*, **300**, 1384-1389.
146. Berlin, Y. A., Hutchison, G. R., Rempala, P., Michl, J. and Ratner, M. A. (2003) Charge hopping in molecular wires as a sequence of electron-transfer reactions. *J Phys Chem A*, **107**, 3970-3980.

147. Kushmerick, J. G., Pollack, S. K., Yang, J. C., Naciri, J., Holt, D. B., Ratner, M. A. and Shashidhar, R. (2003) Understanding charge transport in molecular electronics. *Molecular Electronics III*, **1006**, 277-290.
148. Tour, J. M., Rawlett, A. M., Kozaki, M., Yao, Y. X., Jagessar, R. C., Dirk, S. M., Price, D. W., Reed, M. A., Zhou, C. W., Chen, J., Wang, W. Y. and Campbell, I. (2001) Synthesis and preliminary testing of molecular wires and devices. *Chem Eur J*, **7**, 5118-5134.
149. Bard, A. J., Fan, F. R. F., Kwak, J. and Lev, O. (1989) Scanning Electrochemical Microscopy - Introduction and Principles. *Anal Chem*, **61**, 132-138.
150. Bard, A. J., Mauzeroll, J., Owhadian, O. and Monks, T. J. (2004) Menadione metabolism to thiodione in hepatoblastoma by scanning electrochemical microscopy. *Proc Nat Acad Sci*, **101**, 17582-17587.
151. Wilburn, J. P., Wright, D. W. and Cliffel, D. E. (2006) Imaging of voltage-gated alamethicin pores in a reconstituted bilayer lipid membrane via scanning electrochemical microscopy. *Analyst*, **131**, 311-316.
152. Black, M., Cooper, J. and McGinn, P. (2005) Scanning electrochemical microscope characterization of thin film combinatorial libraries for fuel cell electrode applications. *Meas Sci Tech*, **16**, 174-182.
153. Georganopoulou, D. G., Mirkin, M. V. and Murray, R. W. (2004) SECM measurement of the fast electron transfer dynamics between Au-38(1+) nanoparticles and aqueous redox species at a liquid/liquid interface. *Nano Lett*, **4**, 1763-1767.
154. Bard, A. J. and Faulkner, L. R. *Electrochemical methods : fundamentals and applications*, 2nd, Wiley: New York, 2001.
155. Schiffrin, D. J., Waters, C. A., Mills, A. J. and Johnson, K. A. (2003) Purification of dodecanethiol derivatised gold nanoparticles. *Chem Commun*, 540-541.
156. Wuelfing, W. P., Templeton, A. C., Hicks, J. F. and Murray, R. W. (1999) Taylor dispersion measurements of monolayer protected clusters: A physicochemical determination of nanoparticle size. *Anal Chem*, **71**, 4069-4074.
157. Hsung, R. P., Babcock, J. R., Chidsey, C. E. D. and Sita, L. R. (1995) Thiophenol Protecting Groups for the Palladium-Catalyzed Heck Reaction - Efficient Syntheses of Conjugated Arylthiols. *Tet Lett*, **36**, 4525-4528.

158. Braun, P. V., Shimmin, R. G. and Schoch, A. B. (2004) Polymer size and concentration effects on the size of gold nanoparticles capped by polymeric thiols. *Langmuir*, **20**, 5613-5620.
159. Liu, S. P., He, Y. Q., Kong, L. and Liu, Z. F. (2005) A study on the sizes and concentrations of gold nanoparticles by spectra of absorption, resonance Rayleigh scattering and resonance non-linear scattering. *Spectrochim Act A*, **61**, 2861-2866.
160. Wai, C. M., Smetana, A. B., Wang, J. S., Boeckl, J. and Brown, G. J. (2007) Fine-tuning size of gold nanoparticles by cooling during reverse micelle synthesis. *Langmuir*, **23**, 10429-10432.
161. Yang, Y., Yan, Y., Wang, W. and Li, J. R. (2008) Precise size control of hydrophobic gold nanoparticles using cooperative effect of refluxing ripening and seeding growth. *Nanotechnology*, **19**.
162. Hutchison, J. E., Lohse, S. E. and Dahl, J. A. (2010) Direct Synthesis of Large Water-Soluble Functionalized Gold Nanoparticles Using Bunte Salts as Ligand Precursors. *Langmuir*, **26**, 7504-7511.
163. Jin, R. C., Qian, H. F., Wu, Z. K., Zhu, Y., Zhu, M. Z., Mohanty, A. and Garg, N. (2010) Size Focusing: A Methodology for Synthesizing Atomically Precise Gold Nanoclusters. *J Phys Chem Lett*, **1**, 2903-2910.
164. Girigoswami, A., Ghosh, D., Sarkar, D. and Chattopadhyay, N. (2011) A Fully Standardized Method of Synthesis of Gold Nanoparticles of Desired Dimension in the Range 15 nm-60 nm. *J Nanosci Nanotech*, **11**, 1141-1146.
165. Li, D. X., Li, C. F., Wan, G. Q., Xu, J. and Hou, W. G. (2011) Facile synthesis of concentrated gold nanoparticles with low size-distribution in water: temperature and pH controls. *Nano Res Lett*, **6**.
166. Simpson, C. A., Farrow, C. L., Tian, P., Billinge, S. J. L., Huffman, B. J., Harkness, K. M. and Cliffl, D. E. (2010) Tiopronin Gold Nanoparticle Precursor Forms Auophilic Ring Tetramer. *Inorg Chem*, **49**, 10858-10866.
167. Hakkinen, H., Walter, M., Akola, J., Lopez-Acevedo, O., Jadzinsky, P. D., Calero, G., Ackerson, C. J., Whetten, R. L. and Gronbeck, H. (2008) A unified view of ligand-protected gold clusters as superatom complexes. *Proc Nat Acad Sci*, **105**, 9157-9162.
168. Harkness, K. M., Fenn, L. S., McLean, J. A. and Cliffl, D. E. (2010) Surface Fragmentation of Complexes from Thiolate Protected Gold Nanoparticles by Ion Mobility-Mass Spectrometry. *Anal Chem*, **82**, 3061-3066.

169. Elmroth, S., Skibsted, L. H. and Elding, L. I. (1989) Kinetics and Mechanism for Reaction between Ammine-(III) and Haloamminegold(III) Complexes and Thiocyanate - Competitive Electron-Transfer and Substitution. *Inorg Chem*, **28**, 2703-2710.
170. Ericson, A., Elding, L. I. and Elmroth, S. K. C. (1997) Kinetics and mechanism of reduction of gold(III) complexes by dimethyl sulfide. *Journal of the Chemical Society-Dalton Transactions*, 1159-1164.
171. Ericson, A., Arthur, C., Coleman, R. S., Elding, L. I. and Elmroth, S. K. C. (1998) Kinetics of interaction of the thione unit in 4-thio-2'-deoxyuridine and 4-thiouridine 5'-monophosphate with rapidly reacting gold(III) complexes. *Journal of the Chemical Society-Dalton Transactions*, 1687-1692.
172. Elding, L. I. and Olsson, L. F. (1982) Kinetics and Mechanism for Reduction of Tetrachloro-Aurate(III) and Tetrabromoaurate(III) by Iodide. *Inorganic Chemistry*, **21**, 779-784.
173. Annibale, G., Canovese, L., Cattalini, L. and Natile, G. (1980) Reduction of Gold(III) to Gold(I) by Dialkyl Sulfides - Evidence for an Atom-Transfer Redox Process. *Journal of the Chemical Society-Dalton Transactions*, 1017-1021.
174. Bachman, R. E., Bodolosky-Bettis, S. A., Pyle, C. J. and Gray, M. A. (2008) Reversible Oxidative Addition and Reductive Elimination of Fluorinated Disulfides at Gold(I) Thiolate Complexes: A New Ligand Exchange Mechanism. *Journal of the American Chemical Society*, **130**, 14303-14310.
175. Wilkins, R. G. *Kinetics and Mechanisms of Reactions of Transition Metal Complexes*, 2nd, thoroughly revised, von der Saal, K., VCH Publishers: New York, NY, 1991.
176. Hainfeld, J. F., Brinas, R. P., Hu, M. H., Qian, L. P. and Lyman, E. S. (2008) Gold nanoparticle size controlled by polymeric Au(I) thiolate precursor size. *J Am Chem Soc*, **130**, 975-982.
177. Gammons, C. H., Yu, Y. M. and Williams-Jones, A. E. (1997) The disproportionation of gold(I) chloride complexes at 25 to 200 degrees C. *Geochimica Et Cosmochimica Acta*, **61**, 1971-1983.
178. Skibsted, L. H. Ligand Substitution and Redox Reactions of Gold(III) Complexes In *Advances in Inorganic and Bioinorganic Mechanisms*; Sykes, A. G., Ed.; Harcourt Brace Jovanovich: London, 1986; Vol. 4, pp 137-184.
179. Fry, F. H., Hamilton, G. A. and Turkevich, J. (1966) Kinetics and Mechanism of Hydrolysis of Tetrachloroaurate(III). *Inorganic Chemistry*, **5**, 1943-&.

180. Wilkins, R. G. *Kinetics and mechanisms of reactions of transition metal complexes*, 2nd thoroughly rev., VCH Publishers: Weinheim New York, 1991.
181. Hendra, P. J. (1967) Raman Spectra of Complex Anions of Formula $Mx4n-$ Where M Is Au_3 Pt_2 or Pd_2 and X Is a Halogen Atom. *J Chem Soc A*, 1298-&.
182. Bekker, P. V. Z. and Robb, W. (1972) Kinetics of Hydrolysis of Tetrachloroaurate(III) Anion in Aqueous Perchloric-Acid. *Inorg Nuc Chem Lett*, **8**, 849-&.
183. Peterson, R. R. and Cliffel, D. E. (2005) Continuous free-flow electrophoresis of water-soluble monolayer-protected clusters. *Analytical Chemistry*, **77**, 4348-4353.
184. Rodahl, M., Hook, F., Fredriksson, C., Keller, C. A., Krozer, A., Brzezinski, P., Voinova, M. and Kasemo, B. (1997) Simultaneous frequency and dissipation factor QCM measurements of biomolecular adsorption and cell adhesion. *Faraday Discussions*, **107**, 229-246.
185. Li, J. H., Liang, Y. and Xie, Y. X. (2006) Modified palladium-catalyzed sonogashira cross-coupling reactions under copper-, amine-, and solvent-free conditions. *J Org Chem*, **71**, 379-381.
186. Urgaonkar, S. and Verkade, J. G. (2004) Ligand-, copper-, and amine-free Sonogashira reaction of aryl iodides and bromides with terminal alkynes. *J Org Chem*, **69**, 5752-5755.
187. Krause, N. and Thorand, S. (1998) Improved procedures for the palladium-catalyzed coupling of terminal Alkynes with aryl bromides (Sonogashira coupling). *J Org Chem*, **63**, 8551-8553.
188. Bailey, W. F. and Wachter-Jurcsak, N. In *Encyclopedia of Reactions for Organic Synthesis*.
189. Martensson, J., Kajanus, J., van Berlekom, S. B. and Albinsson, B. (1999) Synthesis of bis(phenylethynyl)arylene-linked diporphyrins designed for studies of intramolecular energy transfer. *Synth-Stuttgart*, 1155-1162.
190. Brase, S. and Kreis, M. (2005) A general and efficient method for the synthesis of silyl-protected arenethiols from aryl halides or triflates. *Adv Synth Catal*, **347**, 313-319.
191. Takagi, K. (1986) A Facile Synthesis of Sulfides Using S-Aryl-Isothiuronium Intermediates. *Chem Lett*, 1379-1380.

Brian N. Turner
Curriculum Vitae

Vanderbilt University
Department of Chemistry
7330 Stevenson Center
VU Station B 351822
Nashville, TN 37235

Phone: (615) 483-3278
E-mail: turnerbn@gmail.com
Birthdate: September 1, 1982
Place of Birth: Cleveland, OH
Citizenship: US

Education

Post-Doctoral Training, Chemical and Materials Engineering, University of Dayton,
November 2011 – Present
Advisor: Dr. Scott A. Gold
Research: Application of Nanomaterials to 3-Dimensional Materials Printing

PhD, Chemistry, Vanderbilt University, December 2011
Advisor: Dr. David E. Cliffel
Dissertation: *Kinetic Investigations of Thiolate Protected Gold Nanoparticles: Protein Interaction, Electron Transfer, and Precursor Formation*

BS, Chemistry (*cum laude*), University of Dayton, May 2005
Advisor: Dr. Shawn M. Swavey
Thesis: *Synthesis and characterization of a tridentate ligand with pyridyl, thioether, and phenolate donors and its copper(II) complexes*

Honors Diploma (*cum laude*), North Royalton High School, June 2001

Publications

Harkness, K.M.; Hixson, B.C.; Fenn, L.S.; **Turner, B.N.**; Rape, A.C.; Simpson, C.A.; Huffman, B.J.; McLean, J.A.; Cliffel, D.E. A Structural Mass Spectrometry Strategy for the Relative Quantitation of Ligands on Mixed Monolayer-Protected Gold Nanoparticles. *Anal. Chem.*, **2010**, 49,10858-10866

Huffman, B.J.; **Turner, B. N.**; Cliffel, D.E. Nanoparticle-based biologic mimetics. In *Nanomedicine*; Baker, J.R. and Ahmad, A., Eds.; Wiley Interdisciplinary Reviews; John Wiley and Sons: Hoboken, NJ, **2008**; 1(Jan./Feb. 2009), 47-59.

Turner, B. and Swavey, S. Synthesis and characterization of a mononuclear copper (II) complex with pyridyl, thioether, and phenolate donors. *Inorg. Chem. Comm.* **2007**, 10(2), 209-211.

Manuscripts in Preparation

Zhang, Y.; **Turner, B.N.**; Krim, M.; Swartz, J.D.; Wright, D.W.; Crowe, J.E., Jr.; Cliffel, D.E. A Quartz Crystal Microbalance Immunosensor for Human Respiratory Syncytial Virus and Nanoparticle Biomimics. **2012.**

Turner, B.N.; Harkness, K.M.; Balinski, A.; Cliffel, D.E. Kinetic study of formation of gold-tiopronin precursor complexes in the synthesis of water soluble gold nanoparticles. **2012.**

Agrawal, A.C; **Turner, B.N.**; Cliffel, D.E. Untitled work on peptide presenting gold nanoparticles *in vivo*. **2012.**

Crisostomo, D.A.; **Turner, B.N.**; Hijazi, F.M.; Chen, G.P.; Cliffel, D.E. Wired Gold Nanoparticles. **2012.**

Conference Presentations

Turner, B.N.; Chen, G.; Hijazi, F.M.; Cliffel, D.E. Wired Gold Nanoparticles. Oral presentation at *The 62nd Annual Pittsburgh Conference on Analytical Chemistry and Applied Spectroscopy*, Atlanta, GA, March 2011.

Turner, B.N.; Cliffel, D.E.; Wiring Gold Monolayer Protected Clusters. Poster presented at *The 240th National Meeting of the American Chemical Society*, Boston, MA, August 2010.

Turner, B.N.; Rutledge, R.D.; Zhang, Y.; Crowe, J.E., Jr.; Wright, D.W.; Cliffel, D.E. Biomimetic Monolayer Protected Clusters for Immunosensor Calibration. Oral presentation given at *The 60th Southeastern Regional Meeting of the American Chemical Society*, Nashville, TN, November 2008.

Turner, B.N.; Zhang, Y.; Rutledge, R.D.; Crowe, J.E., Jr.; Wright, D.W.; Peptide presenting gold monolayer protected clusters as human respiratory syncytial virus fusion protein mimics; Poster presented at *The 59th Southeastern Regional Meeting of the American Chemical Society*, Greenville, SC, October 2007.

Turner, B.N.; Zhang, Y.; Broncel, M.; Crowe, J.E., Jr.; Wright, D.W.; Cliffel, D.E.; A Quartz Crystal Microbalance Immunosensor for Human Respiratory Syncytial Virus and Gold Nanoparticle Mimics for Calibration; Poster presented at *The 58th Annual Pittsburgh Conference on Analytical Chemistry and Applied Spectroscopy*, Chicago, IL, February 2007.

Teaching Experience

Undergraduate Instructor
University of Dayton (Fall 2004 –Spring 2005)
Courses: General Chemistry Lab I

Graduate Instructor
Vanderbilt University (2005-2007)
Courses: General Chemistry Lab I Organic Chemistry Lab II Instrumental Analysis Lab

Private Tutor
Nashville, TN (2006-2010)
Courses: General Chemistry, Organic Chemistry, High School Chemistry and Algebra

Research Interests

Gold nanoparticle synthesis and characterization.
Applications of gold nanoparticles to life science, materials science, and catalysis.
Sensor and assay development.
Chemical kinetics

Skills

Synthesis: Organic compounds, Inorganic complexes, Gold nanoparticles, Peptides

Instrumental Techniques: ¹H NMR, Mass Spectrometry, Transmission Electron Microscopy, Electrochemistry, Spectroelectrochemistry, Scanning Electrochemical Microscopy, UV-Vis Spectroscopy, FT-IR Spectroscopy, Quartz Crystal Microbalance, Semi-prep HPLC

Other Techniques: ELISA, Chromatography

Languages: Novice level German

Computer Skills: Microsoft Office, ChemOffice, Image J, instrument specific software such as Bruker TopSpin.

Honors, Awards, and Affiliations

Dawson Fellowship (Vanderbilt, outstanding entering chemistry graduate)

Graduate Teaching Assistantship (Vanderbilt)

Graduate Research Assistantship (Vanderbilt)

Bernard J. Katchmann Scholarship (U. Dayton, outstanding entering chemistry major)

Carl I. Michaelis Scholarship (U. Dayton, outstanding chemistry major upperclassman)

University of Dayton President's Scholarship (U. Dayton, high GPA and ACT score)

President, Student Affiliates of the ACS, 2004-2005

-Founder, Science Day with the Dakota Center, in collaboration with other UD science clubs, for inner-city children (2005)

Secretary, Student Affiliates of the ACS, 2003-2004

Amnesty International (UD Chapter)

American Chemical Society (member since 2006)